

# **Cation ordering and ferroelectric properties of epitaxial Pb(Sc,Ta)O<sub>3</sub> thin films grown by pulsed laser deposition**

## **Dissertation**

zur Erlangung des akademischen Grades  
doktor rerum naturalium (Dr. rer. nat.)

vorgelegt der  
Naturwissenschaftlichen Fakultät II  
der Martin-Luther-Universität Halle-Wittenberg

von

**Anuj Chopra**

geb. am 8. März 1981 in Hamirpur, Indien

angefertigt am Max-Planck-Institut  
für Mikrostrukturphysik in Halle an der Saale



Gutachter:

1. Prof. D. Hesse
2. Prof. H. Beige
3. Prof. K. Doerr

Halle (Saale) 04.07.2011

## In Sanskrit

यदा किञ्चिज्ज्ञोऽहं द्विप इव मदान्धः समभवम्

तदा सर्वज्ञोऽस्मीत्यभवदवलिसं मम मनः।

यदा किञ्चित्किञ्चिद्बुधजनसकाशादवगतं

तदा मूर्खोऽस्मीति ज्वर इव मदो मे व्यपगतः ॥

## English translation

*With limited knowledge,*

*I had become blind by pride like a wild elephant.*

*However, in the association of wise men*

*slowly my pride waned like a fever,*

*with the realization of my ignorance*

*and the undying pursuit of knowledge.*

*Dedicated to my lovely parents and girlfriend*

## Contents

1.	Introduction and background work	3
2.	Basics and fundamentals of relaxor ferroelectrics and thin films	6
	2.1 Ferroelectric and relaxor materials	6
	2.1.1 Evolution of ferroelectric technology	6
	2.1.2 Definition and structural aspects of ferroelectric materials	8
	2.2 Thin films	17
3.	Experimental techniques and details	21
	3.1 Deposition techniques	21
	3.1.1 Pulsed laser deposition	21
	3.1.2 Radio frequency sputtering	27
	3.2 Structural characterization	28
	3.2.1 X-ray diffraction (XRD)	28
	3.2.2 Atomic force microscopy	32
	3.2.3 Transmission electron microscopy	34
	3.3 Electrical measurements	38
4.1	Results and discussions	40
	4.1.1 PST target	40
	4.1.2 PST thin film deposition	42
	4.1.3 Microstructure of PST films	44
	4.1.4 TEM investigations	47
	4.1.5 Electrical characterization of PST films	50
	4.1.6. Growth and microstructure of PST (111) thin films	54
	4.1.7. Electrical characterization of PST (111) thin films	57
	4.1.8. Summary	59
4.2	Impact of strain on PST films	60
	4.2.1. Deposition of PST on LSMO-electroded STO substrates	60
	4.2.2. Structural investigations	61
	4.2.3 TEM investigations	64
	4.2.4 Electrical characterization of PST films	67
	4.2.5 Non-linear dielectric and piezoelectric behaviour of PST films	70
	4.2.6 Summary	75
4.3	Integration with Si	77
	4.3.1. Deposition of PST films on buffered Si substrates	78
	4.3.2. Structural investigations	78
	4.3.3 TEM investigations	83
	4.3.4. Electrical measurements	85
	4.3.5. Non-linear dielectric and piezoelectric behaviour of PST films	89
	4.3.6 Summary	94
5.	Conclusions and future prospects	95
	References	99



## **Chapter 1. Introduction and background**

In 2005, nature news published an article professing “Relaxors go critical” [1.1]. In the article it is stated that relaxor ferroelectrics are fascinating and useful materials, but they seem to be very heterogeneous. Observing their reaction under electric fields reveals critical behaviour that helps to understand their properties. That article shows how important relaxors are for the development of new devices that work under the effect of an external electric field. Further, in 2006, a giant electromechanical response was discovered in relaxor ferroelectrics [1.2]. Thus recent work shows that the relaxor ferroelectrics offer very interesting and unique properties for application, although it is still challenging to understand them completely. Further study is therefore needed to explore the properties of relaxors fully. In recent years there has been considerable interest in the development of materials to be used in pyroelectric infrared (IR) detection and thermal imaging for both military and commercial applications ranging from night vision, surveillance, driving aids, fire-fighting to security systems [1.3-1.5]. Commercially available high resolution systems utilize photoconductive or photovoltaic p-n junction detectors, which are based on cadmium mercury telluride (CMT), or Si-PtSi Schottky barriers [1.6-1.7]. However, these materials are difficult to grow and require cooling, usually to 77 K for maximum ideal performance and therefore applications are limited to high value high power systems. On the other hand, thermal detectors do not require cooling, although their performance is lower. But still thermal detectors require a comparatively cheap technology and are thus able to provide low power compact IR cameras. The most successful uncooled arrays to date use a hybrid solder-bumped technology and are based on ferroelectrics as the detector material, operating as pyroelectrics or (in a related mode) as dielectric bolometers [1.8-1.10]. Further improvement has continued with the development of phase transition materials such as lead scandium tantalate oxide (PST) [1.4, 1.11]. The competition between detectors has become keener as the designs move towards integrated technologies involving direct deposition of the detector as a thin film onto the integrated circuit. This potentially would yield higher performance with reduced costs. Thus PST is a very promising material for use in uncooled infrared (IR) radiation sensors for a wide

range of applications. Recent effort has been focused on the growth of PST as thin films directly onto different substrates and silicon wafers in order to lower cost and improve device performance. Epitaxial growth of PST thin films on existing silicon circuitry could thus pave the way for fabricating even thinner, more efficient devices, because of their minimal leakage, optical scattering and other improved properties compared to polycrystalline films [1.12].

A number of techniques have been used for the deposition of PST thin films. In the past, PST thin films have been prepared by reactive sputtering [1.13-1.17], by sol-gel [1.18, 1.20], metal-organic chemical-vapor deposition [1.21] and pulsed-laser deposition [1.22, 1.23]. Most of the reports showed a poor microstructure and a specific amount of pyrochlore phase which further degrade the properties of the PST films. Sol-gel and metal-organic chemical-vapor deposition techniques are two-step processes, where first PST is deposited into a non-perovskite form, usually amorphous, followed by a post-deposition annealing step to achieve the perovskite phase. Generally, the annealing temperature is quite high which can further create another problem like intermixing of other electrode material, cracking and lead deficiency etc. PST has a cubic perovskite structure, where Scandium and Tantalum cations occupy the octahedral interstitials. PST is called cation ordered if these cations are ordered in a particular fashion along (111) planes, hence doubling the perovskite lattice parameter. Such ordered structure has better ferroelectric and other properties when compared to the disordered relaxor phase. In case of thin films deposited by Pulsed Laser deposition (PLD), there is no report on the degree of cation-ordering, and the films are polycrystalline. Hence, a motivation is given to explore the epitaxial growth by PLD and the characteristic properties of the films. In the present work we have focused on cation-ordered PST thin films and the influence of cation-ordering on the properties of these thin films. Further we have shown the effect of stress on cation-ordering. In this work **Chapter 2** describes the fundamentals required for the understanding of this topic. In this chapter a brief history of ferroelectrics, definitions, structural aspects and characteristic properties of ferroelectric materials is addressed. A brief introduction into relaxors, cation-ordering and applications of relaxors is included in the chapter. Further, the chapter consists of basics of thin film growth with various growth mechanisms, and a short introduction into the materials with their structure is given.

**Chapter 3** addresses the various techniques used to characterize the PST thin films. All the techniques used are briefly explained with their basic principles. Fabrication methods and influence of deposition conditions are explained. In this chapter, various techniques used for structural studies like X-ray diffraction, atomic force microscopy, piezoforce microscopy and transmission electron microscopy are explained. Further techniques used for the electrical investigations are described in the same chapter.

**Chapter 4.1** consists of results and discussions. First refinement results regarding the PST target are explained. The cation ordered ferroelectric thin films were fabricated on SrTiO<sub>3</sub> (STO) substrates using SrRuO<sub>3</sub> (SRO) as electrode. Various structural and electrical results obtained for the PST thin films fabricated on SRO/STO are explained. This chapter also addresses the influence of growth on ferroelectric and structural properties. Since PST is rhombohedral in structure, its polarization is along the [111] direction. In order to exploit more ferroelectric properties, (111)-oriented PST films were prepared. The microstructure and ferroelectric properties of these PST (111) films are included in the same chapter. In order to find the effect of stress on microstructure and electrical properties of PST, a thin layer of PST was fabricated on La<sub>0.7</sub>Sr<sub>0.3</sub>MnO<sub>3</sub> (LSMO)/STO. The effect of strain on microstructure and electrical properties of thin PST films is explained in **Chapter 4.2**. Since oxide single crystals are not suitable as substrates in silicon-based microelectronics, epitaxial ferroelectric thin films should be grown on silicon substrates. Thus PST was deposited on buffered Si substrates. Structural and electrical properties of PST thin films on buffered Si substrates are explained in **Chapter 4.3**. Finally, in the **Chapter 5**, a summary is given and future work is considered.

## **Chapter 2. Basics and fundamentals of relaxor ferroelectrics and thin films**

### **2.1 Ferroelectric and relaxor materials**

#### **2.1.1 Evolution of ferroelectric technology**

The spontaneous possession of a temperature dependent electric dipole moment is known as pyroelectricity. This phenomenon has been known since ancient times because of the ability of such materials to attract objects when heated. It is generally believed that the piezoelectric effect was first suggested by Charles Coulomb circa in 1785 [2.1] but this phenomenon was not actually confirmed until about 1880. In an attempt to characterize this property in a quantitative manner, Gauguin in 1856 carried out several experiments which eventually led to the discovery of piezoelectricity. The Curie brothers, Jacques Curie and Pierre Curie, in 1880 described the production of electrical polarity on application of mechanical/thermal stress [2.2]. They found that when external stresses were applied by placing small weights on the surfaces of crystals such as quartz and Rochelle salt, electric charges developed on the surfaces proportional to the weights. The phenomenon was later named “piezoelectricity” where “piezo” is a Greek derivative meaning “to press” [2.1, 2.2]. In 1920, Valasek discovered that the polarization of sodium potassium tartrate tetrahydrate ( $\text{KNaC}_4\text{H}_4\text{O}_6 \cdot 4\text{H}_2\text{O}$ ), commonly known as Rochelle salt, could be reversed by application of an external electric field. Since the dielectric properties of this crystal were analogous to the ferromagnetic properties of iron such as the presence of a hysteresis effect in the field polarization curve, a Curie temperature (or two in the case of Rochelle salt) and a large dielectric and piezoelectric response close to the ferroelectric region, the phenomenon was termed “ferroelectricity”. The



large dielectric phenomenon associated with this compound was called “Seignette-electricity” and the point of polar ordering in Rochelle salt was called Curie point [2.3]. Until 1935, Rochelle salt was the only compound with this property when potassium dihydrogen phosphate ( $\text{KH}_2\text{PO}_4$ ) was discovered. Soon, this compound was exploited for its simple structure and feasibility to theoretical understanding. Using this compound, Slater (1941) presented the first basic microscopic model of a ferroelectric, which in its essentials has withstood the test of time [2.4]. There was a growing conviction that the existence of a hydrogen bond was necessary if not sufficient to create polar instability and hence there was little motivation to look for ferroelectric properties in oxides. During World War II, barium titanate, the prototype ferroelectric oxide, was discovered in a search for dielectrics to replace mica. Shortly after the understanding that this material had a dielectric constant of 1000 to 3000 at room temperature and even higher in higher temperatures, Wul and Goldman reported the presence of ferroelectricity in this material [2.5]. From being the first ferroelectric without hydrogen bonds, Barium titanate rapidly became the most extensively investigated ferroelectric material known to date, owing to structural simplicity, ferroelectricity at room temperature, chemical and mechanical stability and ease of preparation. Soon, an array of perovskite materials were reported to have ferroelectricity such as  $\text{KNbO}_3$ ,  $\text{KTaO}_3$ ,  $\text{LiNbO}_3$ ,  $\text{LiTaO}_3$ , and  $\text{PbTiO}_3$  [2.6-2.9]. The simplicity of the perovskite structure gave rise to microscopic theoretical studies. Mason and Matthias proposed a simple model in which the off-center  $\text{Ti}^{4+}$  ion surrounded by 6 oxygen ions gave rise to a unit dipole which is capable of undergoing the order-disorder changes in the presence of thermal or electrical field [2.10]. This model was used by some of the earliest statistical models. Independent pioneering work from Slater in 1950 suggested that the ferroelectric behavior of  $\text{BaTiO}_3$  was caused by long-range dipolar forces which tend to destabilize the high-symmetry configuration favored by the local forces. This model described phase transitions in displacive-type ferroelectrics [2.11]. In 1960, the microscopic theory was written in terms of crystal lattice dynamics and for the first time the existence of “soft modes” was proposed that were later confirmed by scattering experiments [2.12, 2.13]. This theory suggested the involvement of ionic motions of all the constituent atoms as the basic variable to describe displacive lattice instability. Mueller (1945) [2.14], Ginsburg (1945-1949) and Devonshire (1949-1954) [2.15, 2.16] described the macroscopic thermodynamic basis of ferroelectricity. Devonshire's paradigm theory described the phase transitions from cubic to tetragonal, tetragonal to orthorhombic, orthorhombic to rhombohedral and it is a theory that has stayed on for decades. Data from reports earlier than 1940s were re-analyzed and ferroelectricity was discovered in compounds such as ammonium sulfate and the list of known ferroelectrics quickly ran into hundreds [2.17].

## 2.1.2 Definition and structural aspects of ferroelectric materials

All crystalline materials belong to seven basic crystal systems. In the order of ascending symmetry, these seven basic crystal systems are triclinic, monoclinic, orthorhombic, tetragonal, trigonal (rhombohedral), hexagonal, and cubic [2.18]. Based on symmetry, these can be sub-divided into 32 crystallographic classes or point groups. Symmetry considerations can be used to find whether a property or effect is permitted for that crystal. The absence of center of symmetry is a prerequisite for the piezoelectric effect to be allowed. 21 of the 32 crystallographic classes lack such a center of symmetry. One of these classes, the cubic class, has other symmetry considerations that exclude the piezoelectric effect, leaving 20 piezoelectric classes. If the crystal has a single polar axis, the material is pyroelectric, i.e. the polarization shows temperature dependence. This occurs in 10 of the 20 piezoelectric classes. Pyroelectric materials have a spontaneous polarization. This polarization arises from the center of positive charges being not coincident with that of negative charges [2.18]. If the polarization can be switched with an electric field, then a pyroelectric material is also ferroelectric. However, this property of the material cannot be determined from symmetry considerations. Hence on the basis of symmetry considerations all ferroelectrics are a subset of non-centrosymmetric, pyroelectric and piezoelectric materials. It has to be noted that, while symmetry can facilitate prediction of whether a property is allowed, it does not convey any information about the extent of these effects. Experimental limitations like electrical conductivity, temperature, pressure can influence the reversibility of polarization to a great extent. Classification of crystals showing the arrangement of classes with piezoelectric, ferroelectric, pyroelectric properties are shown in the following figure

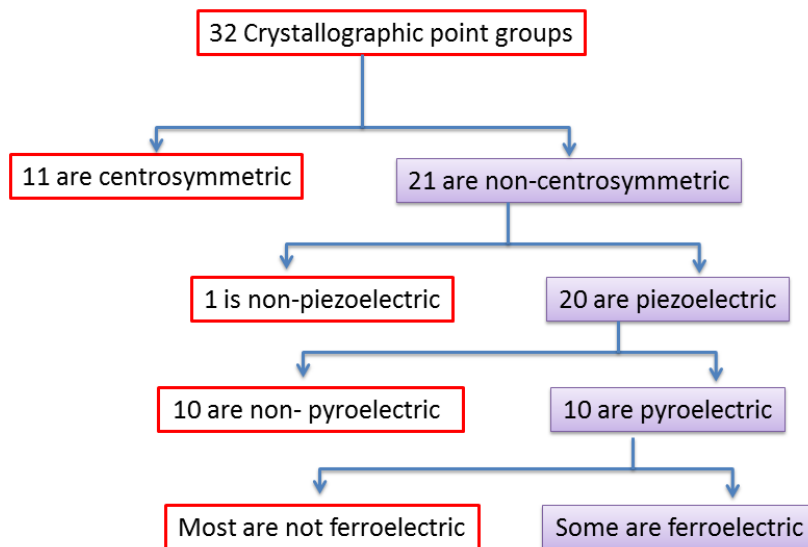


Fig. 2.1. Flow chart describing the relation of ferroelectrics to the 32 crystal classes.

(Fig. 2.1). The materials, which we have studied in this thesis work, are perovskite structure materials. Thus the next section is going to explain briefly about the perovskite structure.

### Perovskite Structure

The presence of a spontaneous polarization is now recognized in a wide group of non-centro-symmetrical lattice materials, predominantly complex metal oxides. The most studied materials belonging to the so-called oxygen-octahedral class of dielectrics are dielectrics having the generalized formula  $ABO_3$ . The representative of that group is  $CaTiO_3$ , a mineral discovered in 1839 in the Urals by Gustav Rose in 1839 [2.19] and named perovskite after Count Lev Alekseevich Perovski, a Russian mineralogist. This common ternary oxide structure, called perovskite structure, (e.g.,  $CaTiO_3$ ,  $BaTiO_3$ ,  $SrRuO_3$  and  $BiFeO_3$ ), is made up of corner-sharing octahedra with the A-cation coordinated by twelve oxygen ions and the B-cation by six. Typically the ionic radius of the A-cation is somewhat larger than the B-cation (Fig. 2a). The structure can easily accommodate a wide range of valence states on both the A and B-sites (i.e.,  $A^{+1}B^{+5}O_3$ ,  $A^{+2}B^{+4}O_3$  and  $A^{+3}B^{+3}O_3$ ) and possesses complex defect chemistry that maintains charge balance in the structure [2.20]. The oxygen ions are situated at the face centre usually. A is a divalent and B a tetravalent metal with

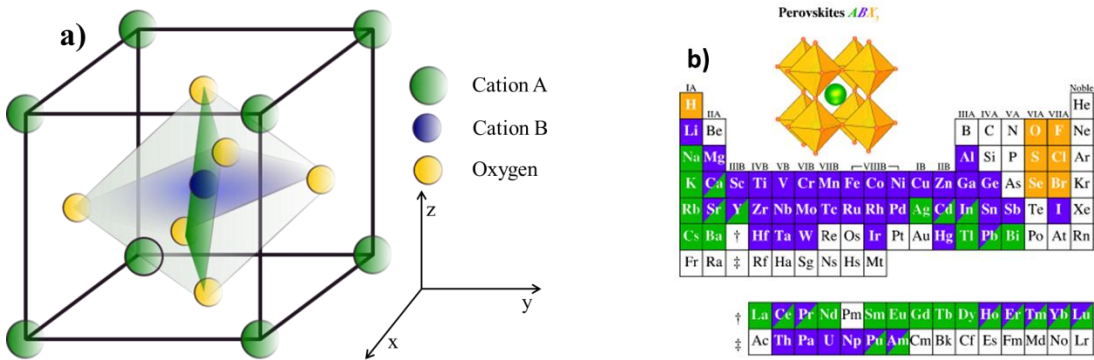


Fig. 2.2. (a) Unit cell of the perovskite structure showing positions of A and B site cations. (b) A periodic table showing the elements that can occupy the three sites (A, B, and X) of the perovskite crystal structure with 100% occupancy. Periodic table is adapted from Ref. [2.20]

potential candidate elements for A and B shown in Fig. 2.2 (b). Similarly, the perovskite structure acts as the parent phase for a wide range of structures including the Ruddlesden–Popper series [2.21] and the high temperature superconductor  $YBa_2Cu_3O_7$ .

### Ferroelectric domains, polarization and hysteresis loop

The minimum region of a crystal where a uniform alignment of dielectric dipoles occurs is called ferroelectric domain, and the interface between two domains is called domain wall. The size and structure of domains depends on the structure of the crystal. A newly formed ferroelectric crystal usually has a polydomain structure. This structure can be transformed into a single-domain structure by applying an external electric field of high strength, a process called poling. A very important characteristic of ferroelectrics is ferroelectric switching. During switching under applied external field of triangular waveform a hysteresis loop develops as depicted in Fig. 2.3. The response of the polarization to an external applied field is initially (*i.e.* at low fields), linear, as given by the equation for linear dielectric as

$$P_i = \chi_{ij}E_j$$

where  $P$  is the polarization vector,  $E$  is the electric field and  $\chi_{ij}$  is second-rank tensor known as the dielectric susceptibility of the material. This region is shown in Fig. 2.3 by segment 1 to 2. With increasing field, the domains with polarization direction opposite to that of the field, start switching in to the direction of the field and, as a result, the measured charge density increases non-linearly (region 2 to 3). When all the domains have polarization aligned to the applied field, a state denominated as saturation, the response of the polarization  $P$  becomes again linear if after stage 3 a higher field is applied (not shown in Fig. 2.3). By decreasing the field strength,  $P$  tends to decrease linearly using the same relationship as given in the equation (point 4) and at zero field it still maintains a positive value (which is called remanent polarization  $P_r$ ).

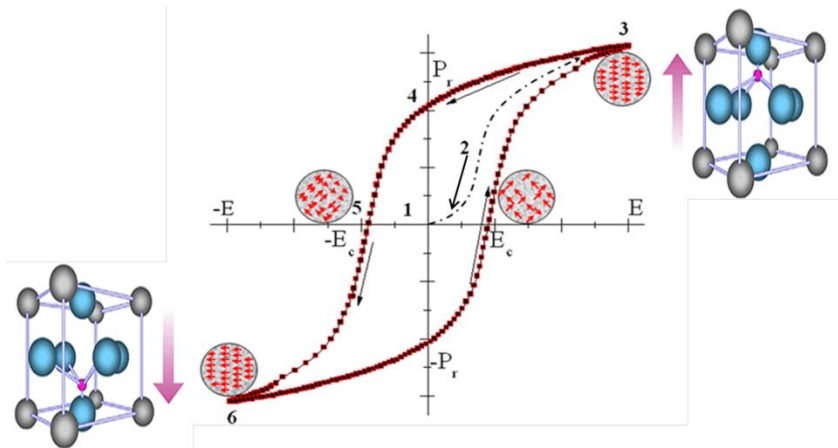


Fig. 2.3. A characteristic polarization vs electric field hysteresis loop of ferroelectric materials.

When a negative electric field of sufficient strength is reached, (point 5) called as coercive field ( $E_c$ ), the nucleation of reversed polarization domains starts. The

polarization  $P$  then decreases non-linearly until saturation is reached for a negative field (point 6). Thereafter an increasing electric field again increases the polarization value linearly. At zero field, the value of polarization is negative. When a positive coercive field value is reached, a steep increase occurs after which again  $P$  increases linearly completing the loop structure.

### **Ferroelectric Curie point and phase transition**

The perovskite structure in the non-polar (or paraelectric) phase is cubic and it has the A cations at the edges, the B cations in the body-center positions, and the oxygen anions in the face-centered positions, forming an octahedron. At a certain temperature designated as the Curie temperature  $T_c$ , the crystal experiences a phase transition from cubic to non-cubic phase. During the transition to the polar (or ferroelectric) phase, the crystal structure changes from cubic to non-cubic (distorted) structure, hence resulting in the formation of a dipole moment and in the presence of a spontaneous polarization. Understanding the structural phase transitions through a thermodynamical approach was first given by Landau [2.22] in 1937 and later adapted by Devonshire for  $\text{BaTiO}_3$  [2.23]. Landau theory serves as the foundation for using symmetry based arguments for macroscopic entities till today. The order parameter polarization, decreases as the temperature increases and attains zero steeply or gradually at  $T_c$ , depending on whether the phase transition is classified as second or first order, respectively. Near the Curie temperature, the dielectric, elastic, optical, and thermal constants of the material show an altered behavior due to distortions appearing in the crystal as the phase changes. According to Landau theory, close to the phase transition, the free energy can be written as an expansion into powers of the order parameter. In case of ferroelectrics, the order parameter is the polarization ( $P$ ). All the odd powers of  $P$  do not occur because of symmetry reason (the parent phase is considered as centrosymmetric). Thus the free energy can be written as:

$$F(P, T) = \frac{1}{2}g_2P^2 + \frac{1}{4}g_4P^4 + \frac{1}{6}g_6P^6 \quad 2.1$$

where  $P$  and  $T$  are polarization and temperature.  $g_2$ ,  $g_4$ ,  $g_6$  are the phenomenological Landau expansion coefficients. The highest phenomenological Landau expansion coefficients (here  $g_6$ ) should be larger than zero, otherwise the free energy will approach minus infinity for large values of  $P$ . The entire coefficients depend on  $T$ , particularly  $g_2$ . Coefficient  $g_2$  in a series of  $T$  around the Curie temperature  $T_\Theta$ , which is equal to or less than the phase transition temperature  $T_c$ , can be written as:

$$g_2 = \frac{1}{C}(T - T_\Theta) \quad 2.2$$

where  $C$  is the Curie constant. The stable state is given by the minima of the free energy with necessary and sufficient conditions:

$$\frac{\partial F}{\partial P} = P(g_2 + g_4P^2 + g_6P^4) = 0 \quad 2.3$$

and

$$\frac{\partial^2 F}{\partial P^2} = \frac{1}{\chi} = g_2 + 3g_4P + 5g_6P^3 > 0 \quad 2.4$$

Now, there are two cases:

- 1) If  $g_4 > 0 \Rightarrow g_6 \approx 0$ , corresponds to a second-order phase transition.
- 2) If  $g_4 < 0 \Rightarrow g_6 > 0$ , corresponds to first-order phase transition.

In the above two cases a trivial solution is  $P = 0$ , which corresponds to a paraelectric state. Further comparing equations 2.2 and 2.4 shows that  $g_2$  can be expressed as susceptibility ( $\chi$ ), for which the Curie-Weiss law can be written as:

$$\chi = \varepsilon - \varepsilon_0 = \frac{C}{T - T_\Theta}$$

where  $\varepsilon$  is the permittivity of the material,  $\varepsilon_0$  is the permittivity of vacuum,  $C$  is the Curie constant and  $T_\Theta$  is the Curie temperature. The dielectric constant increases with an increase in temperature reaching a maximum at  $T_c$  and decreases above  $T_c$  following the Curie-Weiss law. A figure showing the behaviour of  $\varepsilon$ ,  $1/\varepsilon$  and  $P$  in the vicinity of a first order and second order phase transition is shown in Fig. 2.4 (a). More details about the phase transition can be found in Refs. 2.24 and 2.25.

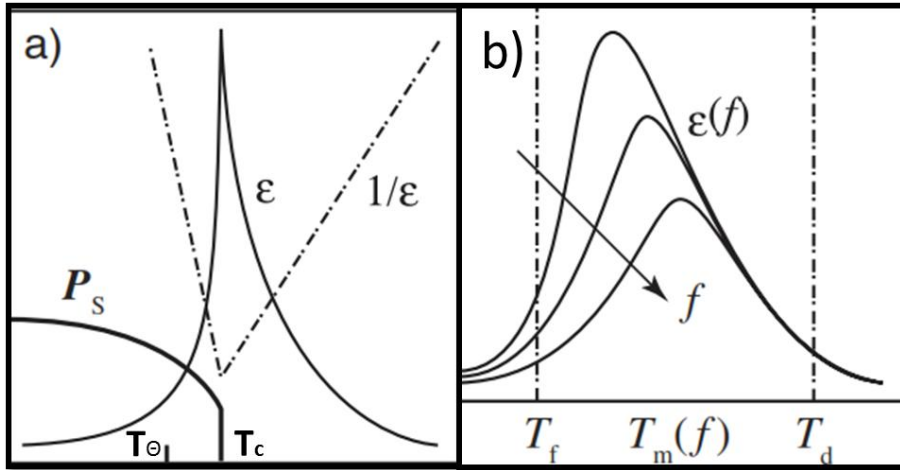


Fig. 2.4. Phase transition diagram for (a) a first order phase transition. If  $T_\Theta = T_c$ , it is a second order phase transition. (b) A relaxor phase transition showing the frequency dependence of the permittivity ( $\varepsilon$ ) [after Ref. 2.25.].

### Normal and relaxor ferroelectrics

Relaxors are a subclass of ferroelectric materials which exhibit a diffuse phase transition with significant frequency dispersion of dielectric permittivity as shown in Fig. 2.4 (b). In order to understand the behaviour of relaxor ferroelectrics, it is essential to contrast their characteristic properties with respect to normal

ferroelectrics [2.26]. A normal ferroelectric generally possesses a square hysteresis loop with large coercive field ( $E_c$ ), spontaneous ( $P_s$ ) and remnant ( $P_r$ ) polarization whereas the relaxors possess a slim loop.  $P_r$  and  $P_s$  vanish at  $T_c$  in normal ferroelectrics but in relaxors, they remain well above the temperature of maximal dielectric constant,  $T_m$ . It is believed that relaxors possess nano-size polar domains in contrast to the macro-size ferroelectric domains in normal ferroelectrics. The presence of nanodomains serves as evidence for the cooperative orientation with the field in the presence of a high electric field. In ferroelectrics, the phase transition can be thermodynamically of first or second order and involves a macroscopic symmetry change at  $T_c$ . On the other hand, relaxor ferroelectrics exhibit a diffuse phase transition with strong dielectric dispersion without undergoing any distinct structural phase transition across  $T_m$ . The peak in the dielectric response is simply a manifestation of the slowing down of the dipolar motion below  $T_m$  [2.27]. Dielectric dispersion generally explains the shifting of  $T_m$  towards higher temperature with increasing frequency. Above  $T_c$ , the dielectric constant obeys the Curie-Weiss law in normal ferroelectrics. For relaxors, the Curie-Weiss law is valid only at very high temperatures, i.e. above a characteristic temperature called the Burns temperature  $T_d$ . Most of relaxor ferroelectrics are lead-based B-site complex perovskite-type materials with a partial or complete chemical disorder on the B-site [2.28], for instance, lead based oxides such as  $\text{PbSc}_{0.5}\text{Ta}_{0.5}\text{O}_3$  (PST),  $\text{PbSc}_{0.5}\text{Nb}_{0.5}\text{O}_3$  (PSN),  $\text{PbMg}_{1/3}\text{Ta}_{2/3}\text{O}_3$  (PMT). There have several models been suggested in order to explain the complex properties of relaxors. Some of them are diffuse phase transition model [2.29, 2.30], superparaelectric model [2.31], dipolar glassy-like model [2.32] and random field-stabilized model [2.33]. In the diffuse phase transition model, it is assumed that the diffuse nature of the phase transition is due to a chemical inhomogeneity of B-site cations. This inhomogeneity leads to various polar microregions with their own local Curie temperature. The superparaelectric model explains the nature of the micropolarization at higher temperatures than  $T_m$ . According to this model, even at higher temperatures the disordered micropolar regions will have a preferential direction, hence they contribute to the polarization. At lower temperature the slowing down of the dynamics of these polar regions gives rise to relaxor-like behaviour. In case of the dipolar glassy-like model, the polar regions are assumed to behave like a spin-glass phase. The size of these polar regions is considered to be increased on cooling, hence the dynamics of polar regions will slow down. This will result in freezing of the dipoles. According to the random-field model, relaxor ferroelectricity is due to a quenched-in random electric field. This random field is arising from the inhomogeneity and charged nano domains. More details about these models can be found in the respective references.

As explained in Chapter 1, PST has the unique property of B-site cation-ordering, which influences its relaxors properties. The next section explains cation-ordering.

### Cation-ordering

Cation-ordering plays an important role in changing the ferroelectric, dielectric, piezoelectric and phase transition properties of many complex oxide perovskites. These complex perovskites have the general formula  $A(B_xB'_{1-x})O_3$ . Depending on the ratio between  $x : (1-x)$ , ordering can be defined as 1:1, 1:2, and 1:3. PST comes in the 1:1 cation order category, with the chemical formula of  $Pb(Sc_{1/2}Ta_{1/2})O_3$ . These 1:1 B-site ordered perovskites are derived from the simple perovskite structure by substituting the octahedral B site by a mixture of two different cations (B and B'). Octahedral B-site cation-ordering occurs, when there is a big difference either in charge or size in the B-site cations [2.34]. Further, the degree of cation order can be enhanced with the preparation conditions and additional heat treatments. Ordering of octahedral B-site cations doubles the unit cell of the simple perovskite which changes the space group from  $Pm\bar{3}m$  to  $Fm\bar{3}m$ . This change in the space group leads to doubling the lattice parameter. The degree of cation-ordering is measured through superstructure reflections in X-ray diffraction (XRD) and transmission electron microscopy (TEM). The X-ray diffraction peaks with even values of Miller indices (hkl) are independent of cation-ordering and known as subcell reflections. Miller indices with odd value are the measure of cation-ordering and known as superstructure reflections. In a cation ordered material, both superstructure and subcell reflections exist. The position and intensity of superstructure reflections are a measure of extent of cation-ordering. In the absence of cation-ordering, only subcell reflections exist but with reduced indices by a factor of two. More details about ordering can be found in Ref. 2.35.

### Materials used in this work

In this thesis, we have used PST as main ferroelectric thin film material. Thin PST films were fabricated on STO substrates using SRO and LSMO as bottom electrode. Further for the technological applications PST films were fabricated on Si substrates using  $CeO_2$  and yttria-stabilized zirconia as buffer layers. For this growth, SRO and  $LaNiO_3$  were used as bottom electrodes. Thus the next section is going to explain some properties of these materials one by one.

**Lead scandium tantalate:** Lead scandium tantalate  $PbSc_{0.5}Ta_{0.5}O_3$  (PST) is a cubic perovskite in bulk at room temperature.  $Pb^{2+}$  cations occupy the corner positions of the cube,  $Sc^{3+}$  and  $Ta^{5+}$  cations occupy the body-centered position, while the oxygen anions occupy the face-centered positions. Alternatively the perovskite structure can be considered as cubic close packed arrangement of  $PbO_3$  planes with the  $Sc^{3+}$  and  $Ta^{5+}$  ions occupying the octahedral interstitials between the planes. PST is ferroelectric when chemically ordered and relaxor ferroelectric when disordered. The Curie temperature of PST has been reported to vary between 0 and 26 °C, depending



on the degree of cation-ordering on the B sites. Below the Curie temperature PST has a rhombohedral structure, whereas above, it has an ideal cubic structure with 0.4074 nm lattice parameter at room temperature [2.36]. The degree of order in B-site cations can be controlled by annealing PST at a temperature lower than the sintering temperature. In a cation ordered PST, space group changes from  $Pm\bar{3}m$  to  $Fm\bar{3}m$  by doubling the unit cell parameter. PST is a wide band gap semiconductor with a band gap of 3.4 eV [2.37].

**Strontium titanate:** Strontium titanate  $SrTiO_3$  (STO) is a cubic perovskite which is paraelectric at RT and frequently used as substrate. For the epitaxial growth of thin films the substrate should be a single crystal. The choice of substrate is limited by various factors, such as crystal symmetry, orientation, minimum lattice parameter mismatch, surface energy consideration, surface termination, chemical nature, thermal expansion coefficient, and most importantly the application for which the film is being deposited. The growth of high-quality epitaxial thin films needs substrates that should have structural and chemical compatibility with the film. Chemical incompatibility between substrates and thin films can lead to inter-diffusion of unwanted elements between each other. Further structural incompatibility and difference in thermal expansion can implant additional defects and cracks inside the films and results in poor electrical and structural properties. STO was used as substrate by alleviating all the negative effects discussed. It is one of the most stable substrates for epitaxial growth of high-temperature superconductors and oxides. STO has a lattice parameter of  $a_{STO} = 0.390$  nm [2.38, 2.39] which is very close to the lattice parameter of PST, thus allowing in principle the epitaxial growth of PST films with a high crystalline quality. Since the lattice parameter of STO is smaller than that of the PST, this will favour a c-axis oriented growth of the PST films.

**Strontium ruthenate:** In general for the electrical measurements of ferroelectric epitaxial thin films,  $SrRuO_3$  is used as a bottom electrode. Strontium ruthenate  $SrRuO_3$  (SRO) is a perovskite which shows a metallic behaviour in the entire temperature range from 4 K to 700 K [2.40]. It has an orthorhombic structure at RT with  $a = 0.553$  nm,  $b = 0.557$  nm and  $c = 0.785$  nm [2.41]. Owing to the only small distortions in the arrangement of the  $RuO_6$  octahedra, it can be regarded as a pseudocubic perovskite with a lattice parameter of  $a_{SRO} = 0.393$  nm. Pseudocubic indexing is used for  $SrRuO_3$  throughout this thesis. Because of small lattice mismatch and good chemical compatibility with STO substrate, SRO grows almost perfectly on it. Further, SRO facilitates a good growth of perovskite layers on it, and is thus suitable as a bottom electrode. Another advantage of using an oxide electrode is its permeability to oxygen vacancies [2.42]. Thus SRO is expected to serve as a good electrode layer in various perovskite oxide based devices.

**Lanthanum nickelate:**  $\text{LaNiO}_3$  is another promising bottom electrode candidate for ferroelectric thin film capacitors. Moreover, it has a perovskite-type structure and lattice constant of 0.384 nm that is close to the lattice constant of most perovskite ferroelectric materials, which makes it possible to use  $\text{LaNiO}_3$  (LNO) as a template layer in promoting the crystal orientation of ferroelectric PST films on buffered Si substrates for the application purpose [2.43].

**Strontium doped lanthanum manganate:** The doped manganates with the perovskite-type crystal structure, such as  $\text{La}_{1-x}\text{Sr}_x\text{MnO}_3$ , have been intensively investigated in recent years because of their outstanding colossal magnetoresistance (CMR) effect [2.44].  $\text{La}_{0.7}\text{Sr}_{0.3}\text{MnO}_3$  (LSMO) is an attractive material for use as a bottom oxide electrode. LSMO bulk is rhombohedral at room temperature with a rhombohedral angle of  $90.26^\circ$  and a pseudocubic lattice parameter  $a$  of 3.873 Å [2.45].

**Buffer layers used to promote the epitaxial growth of PST on the silicon wafers:** The epitaxial growth of oxide thin films on silicon substrates is a challenging process due to oxidation of silicon to amorphous silicon oxide and possible diffusion and/or reaction processes between film and substrate. We achieved this aim by using an epitaxial buffer layer of  $\text{CeO}_2$  and yttria-stabilized (9 mol %) zirconia (YSZ) between the PST film and the silicon substrate. YSZ with (9 mol %) has cubic crystal structure with a lattice parameter of  $a=0.514$  nm. Several studies suggest that a thin  $\text{SiO}_2$  layer on top of the Si surface favors the high-quality epitaxial growth of YSZ. It is assumed that the impinging zirconia atoms reduce the  $\text{SiO}_2$  to Si, which epitaxially crystallizes on the substrate, enabling  $\text{ZrO}_2$  epitaxy. Epitaxial  $\text{SrRuO}_3$  films with (110) orientation have been grown on Si (100) substrates with these (100)-oriented YSZ buffer layers [2.46, 2.47]. Further in order to obtain PST (100) growth, an additional  $\text{CeO}_2$  buffer layer was introduced on the YSZ buffer layer, which promotes the epitaxial growth of  $\text{LaNiO}_3$  (100), hence PST (100) [2.48].  $\text{CeO}_2$  is used in catalytic converters for cars and in fuel cell applications where oxygen vacancies may determine the physical properties. It crystallizes in the fluorite structure (cubic) with lattice parameter 0.541 nm and is an interesting material because it is lattice matched to silicon within 0.35% at room temperature.

## **2.2 Thin films**

A film is a thin layer of material which is deposited on a substrate. A thin film can have a thickness range from a few monolayers to several micrometers. The production of thin films for device purposes has been developed over the past 40 years. Thin films play an important role in science and technology. Thin film technology has also developed for the needs of the integrated circuit industry. Compared to bulk materials, thin film forms of materials are important because of their unique functionalities and applications such as hard coatings, integrated circuits (ICs), filters, reflective, anti-reflective coatings etc. The increasing demand for the development of smaller and smaller devices with higher speed, especially in new generations of integrated circuits, requires advanced materials and new processing techniques suitable for future giga scale integration (GSI) technology. Thus the thin film technology becomes more and more important. In this regard, it is very important to understand nucleation and growth processes of thin films.

### **Epitaxial thin films**

The word epitaxy comes from the Greek prefix epi meaning “upon” or “over” and taxis meaning “arrangement” or “order.” Thus epitaxy refers to the process of atom-by-atom growing of thin films or complex structures onto the surface of a substrate. Epitaxial growth of thin films refers to the formation of a single crystal film on top of a single crystal substrate and the subsequent evolution of a specific crystallographic orientation relationship between the film and the underlying substrate as growth commences. The specific orientation relationship is governed by the crystal systems and lattice parameters of the substrate and thin film. There can be more than one orientation relationship in case of deviation from the single crystalline structure of the film. The specific orientation of the film is significantly influenced by that of the substrate as a result of some degree of matching between the two along the interface. Epitaxy can be classified into two types: homoepitaxy and heteroepitaxy. Homoepitaxy is the simplest form of epitaxy and refers to the case where the film and the substrate are of the same material, for example, epitaxial Si deposited on Si wafers is the most significant example of homoepitaxy. On the other hand, heteroepitaxy refers to the case where films and substrates consist of different materials, for example, Ge deposited on Si. Practically heteroepitaxy is the most important form of epitaxy.

The lattice mismatch between substrate and thin film material plays an important role in epitaxial growth. In case of homoepitaxy, there is no lattice mismatch. In case of heteroepitaxy, there is generally a lattice mismatch between substrate and film material, causing either a strained or relaxed interface depending on the difference in mismatch as shown in Fig. 2.4.

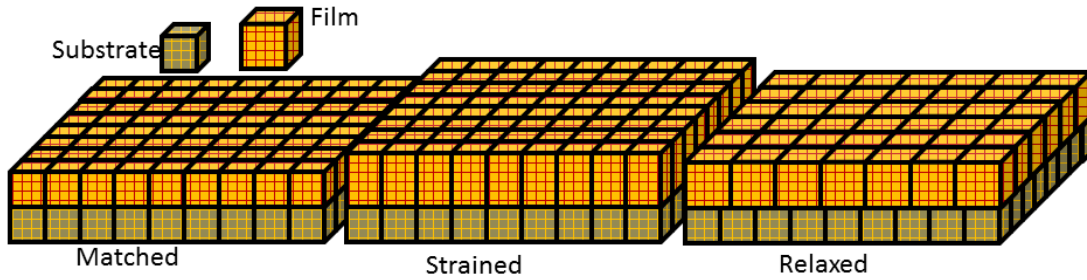


Fig. 2.4. A schematic illustration of matched, strained and relaxed epitaxial growth.

The lattice mismatch between film and substrate can be written as:

$$f = \frac{a_f - a_s}{a_f}$$

where  $a_s$  and  $a_f$  are the lattice parameter of substrate and epitaxial thin film, respectively. For the ideal epitaxial growth, the lattice mismatch should be as low as possible. Heteroepitaxial growth can take place through different ways. One of them is cube-on-cube growth, in case of lattice matching. In the case when the lattice mismatch is too high, the film plane can rotate by  $45^\circ$  in order to reduce the lattice mismatch and hence the interface energy. Fundamentally the minimization of interface energy governs the epitaxial growth of thin films. Further, in heteroepitaxial growth, up to a thickness of a few monolayers,  $a_s = a_f$ , hence this causes strain in the films, which results in stress inside the films. This stress inside the thin films increases the interface free energy, and as the thickness keeps on increasing up to a point (called critical thickness), this interface energy is released in the form of the formation of misfit dislocations [2.48] or crystallographic domains [2.49]. This process is called relaxation process and the film relaxes fully when the lattice parameter of the film becomes equal to its bulk lattice parameter. Positive strain forces the film to a smaller lattice parameter and is called compressive strain. On the other hand negative strain causes tensile strain.

### Growth mechanisms of epitaxial thin films

In a typical thin film growth process, the arriving adatoms (an atom reaching the surface of the substrate from the target) must adsorb on the substrate surface. Some of the adatoms might have high enough energy to re-evaporate, but others participate in a diffusion process along the surface. After the diffusion process, these adatoms form clusters which might become stable once the critical size limit is reached [2.50]. The process of forming stable clusters is called nucleation. Further growing of these stable clusters leads to their coalescing and the formation of a continuous film. The way the particles nucleate may determine the structure or morphology of the growing film. Three typical film growth modes, which take place during growth of epitaxial thin films, are:

**Frank-van der Merwe (FV) growth mode (Layer-by-layer growth)**

During FV or layer-by-layer growth mode a new layer is nucleated only after completion of the layer below. In this growth mode, the adatoms are more strongly bonded to the substrate than to each other therefore facilitating the layer-by-layer 2D-growth. This growth mode is shown schematically in Fig. 2.5 (a).

**Volmer-Weber (VW) growth mode (Island growth)**

In the VW growth mode, growth is in the form of 3D-islands, either by surface diffusion or direct impingement of atoms on active sites like crystal defects, atomic steps or impurities as shown in Fig. 2.5 (b). Thus after initial VW growth, further growth occurs in the columnar mode. A continuous film is formed when the islands are large enough to come into contact with each other and coalesce. One simplistic explanation for this growth behavior is that the atoms or molecules being deposited are more strongly bonded to each other than to the substrate material.

**Stranski-Krastanov (SK) growth mode**

SK mode is a mixture of the FV and VW growth modes. It is caused by a significant lattice misfit between film and substrate. The lattice mismatch between the substrate and the film creates a built-in strain as a consequence of the increasing elastic energy with increasing layer thickness. The first few monolayers are deposited atomically smooth (FV growth mode), as a strained layer up to a critical thickness. When the thickness increases the critical thickness, a transition to island growth rapidly takes place (VW growth mode) in order to release the mismatch strain. This mode is schematically shown in Fig. 2.5 (c).

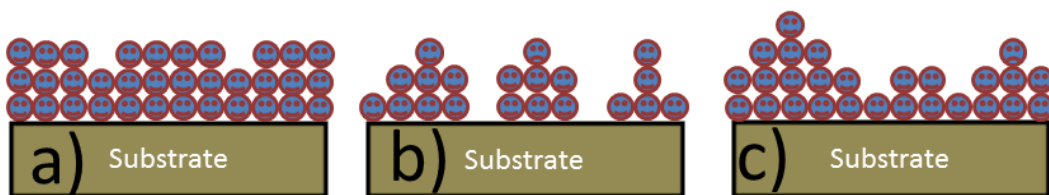


*Fig. 2.5. Different epitaxial growth modes. (a) Frank-van der Merwe growth mode. (b) Volmer-Weber growth and (c) Stranski-Krastanov growth mode*

In addition to the above explained three growth processes, two more growth processes are induced by the substrate surface. Step flow mode is clearly distinct from layer-by layer growth in FV mode. Unidirectional step flow is induced by substrate misorientation (offcut angle). This trick is often used to avoid island formation, their coalescence and following columnar growth in epitaxy from the vapor phase. Step bunching is observed when a high density of steps moves with large step velocities over the growth surface. More details of step flow and step

bunching processes can be found in Refs. [2.51-2.52].

## **Chapter 3. Experimental techniques and details**

### **3.1 Deposition techniques**

Fundamentally, thin films can be grown by two methods known as physical vapor deposition (PVD) and chemical vapor deposition (CVD). Each deposition method has its own benefits and limitations. Pulsed laser deposition (PLD), and radio frequency (RF) sputtering, both belong to PVD, were used for the deposition of various oxide thin films and platinum (Pt) top electrodes. In this section, both techniques will be discussed with their basics and working principle.

#### **3.1.1 Pulsed laser deposition**

PLD is one of the most versatile and efficient techniques used for the deposition of thin films in solid state physics. PLD is a good method to ensure stoichiometric transfer of components from a bulk material to a thin film form and to prepare multilayers [3.1]. In this growth technique, a laser beam with a specific pulse duration and frequency is used to ablate the solid material (known as target) in the form of a luminous plume consisting of ions and atoms. PLD is a highly non-equilibrium deposition technique, in which the focused intense laser beam hits the surface of the target resulting in a sharp and rapid increase in temperature (more than 4500 °C within few nanoseconds, with a heating of  $10^{12}$  K/s) [3.2], hence ensuring an equal and uniform evaporation of all the elements of the targets, irrespective of their partial binding energy. The angular distribution of the ablated plume of material frequently follows the power cosine law [3.3]. Generally the flow of material is directed towards the substrate, where it condenses back to the solid state to form the film. The size of the plume depends on the absorption properties and the band gap of the target material, on laser wavelength, pulse duration and gas pressure inside the deposition chamber. The first time, PLD was used in 1965 by Smith and Turner [3.4], for the preparation of semiconducting, dielectric and organometallic thin films. The first ferroelectric film was deposited in 1968 by Schwarz and Tourtellotte [3.5].

Due to technical difficulties, this technique became more distributed only after 1987, when Dijkkamp and coworkers reported the successful growth of high-temperature superconductor oxide thin films [3.6]. Since that time, PLD became a very popular deposition tool for the growth of oxide thin films. The PLD technique provides a lot of freedom to vary many parameters. Deposition parameters like substrate temperature, target-substrate distances, background gas pressure and many more can be varied. Further in addition, laser parameters like fluence, wavelength, pulse duration and repetition rate can be changed. Nowadays PLD machines are equipped with a multi target holder, which provides the opportunity to grow *in-situ* complex multilayer structures. In case of complex multicomponent oxide materials, by conventional equilibrium technique like evaporation and sputtering, it is very difficult to achieve good stoichiometry and hence a lot of efforts is required to get similar stoichiometry of the films as of the target (from a single target), because of different partial pressure and sputtering yield of each element. Because of the non-equilibrium nature of the process, PLD provides us with the possibility to grow metastable materials which cannot be obtained with conventional techniques [3.7]. PLD is a simple, powerful and cost effective technique and provides fast deposition of thin films. All of these benefits made PLD one of the most popular techniques for thin film growth. The PLD process is mainly divided into three basic stages. These are: laser-target interaction, plume-laser interaction and film growth. All the three processes are discussed shortly below in the next section.

### Laser-target interaction

When a laser beam strikes the surface of a target, the photon energy of the laser

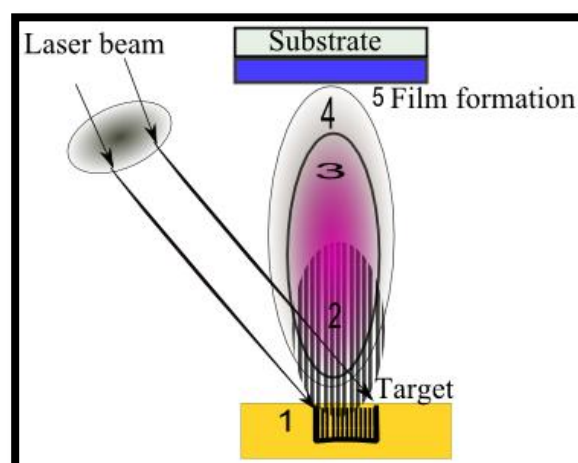


Fig. 3.1. Description of different steps involved in the PLD process. (1) Laser-target interaction. (2) Evaporation and ablation. (3) Formation of a Knudsen layer and absorption by the plasma. (4) Adiabatic expansion of the plasma. (5) Thin film formation.



interacts only with the surface of the target, resulting in a sharp increase in surface temperature of the target, although the bottom remains close to room temperature (RT). The congruent evaporation of all the elements from the target simultaneously is achieved by applying the laser energy to a small volume within a short duration of the order of 20 ns. There is a threshold energy density for the ablation of a certain target material which depends on the target material properties like band gap, reflectivity etc. If we consider that  $h\nu$  is the laser energy of the incident beam, and  $E_g$  is the energy gap of the target material, then if  $h\nu - E_g > 0$ , the excess photon energy is quickly transformed into a phonon and thus results in heating of the target surface [3.8]. It has been found that if the laser energy density is less than the threshold energy density, then the ablated plume follows a simple cosine law and gives a non-stoichiometric deposition, very similar to conventional deposition techniques, but if the energy density is higher than the threshold energy density, the plume follows the power cosine law and gives a highly stoichiometric deposition [3.9]. The impact of the intense laser beam on the target produces melting and re-solidification, and can cause compositional and topographical changes as shown in Fig. 3.1 (1-2). This problem can be solved by continuous rotation of the targets, resulting in a uniform removal of material from the whole target.

Further, the interaction of the directed laser beam with the plume breaks the constituents of the plume up via photo-dissociation and photo-ionization, resulting in the formation of a thin plasma layer. Particles evaporated from the surface of the target are in thermal equilibrium through collisions and form a layer called Knudsen layer. In the Knudsen layer, the emitted particles can have a different velocity distribution than the ones emitted through pure thermal ablation and evaporation [3.10]. This process is schematically shown in Fig. 3.1 (3). Further heating of plasma occurs via an inverse Bremsstrahlung process, which expands the plasma adiabatically in the direction perpendicular to the target surface [3.11]. The adiabatic, collisionless, expanded fluorescent plasma plume is directed towards the substrate surface as shown in Fig. 3.1(4). The microscopic mechanism of the film formation by nucleation and growth during condensation of the vapour phase onto the substrate is explained in Chapter 2.2.

### **Excimer laser**

Most of the materials used for thin film growth exhibit a strong absorption coefficient in the UV region. An excimer laser bombards the target with pulses of light in the ultraviolet (UV) wavelength spectral range. This wavelength facilitates better light absorption and thus the light penetrates only the surface near the region of the targets. It is therefore employed in most PLD chambers for the ablation. The first experimental demonstration of excimer lasers was performed in 1970 [3.12]. The name “excimer” comes from “excited dimer”, where dimer stands for diatomic molecules like  $N_2$ ,  $H_2$ , and  $O_2$ . The excimer lasers are gas lasers. Excimer lasers

operate with a combination of inert gas [argon (Ar), krypton (Kr), or xenon (Xe)] and reactive gas [fluorine (F) or chlorine (Cl)]. Energy is pumped into the gas mixture by electric discharge to produce excited species. As a result, these excited species react chemically in the presence of a buffer gas (He or Ne) and produce the rare gas halogen excimer molecules. The rare gas halogen formation takes place by two major reaction channels: first, by recombination of a positive rare ion and negative halide ion in the presence of the buffer gas and second, by the reaction of the excited rare gas atom with a halogen molecule (called harpooning reaction). These reactions take place in nanoseconds. In case of the KrF laser, the excited KrF is very unstable and it decays to Kr and F<sub>2</sub> with the emission of a photon within some nanoseconds, being then available for another excitation cycle. Because of this unstable ground state, excimer lasers belong to the class of four-level lasers and have inherently a high efficiency [3.13]. Modern lasers can be called exciplexes because they are based on excited complexes of rare gas monohalides rather than on excited dimers. The most important lasing species in an excimer laser are ArF (193 nm), KrF (248 nm), XeCl (308 nm) and XeF (351 nm). Recently, the fluorine laser (F<sub>2</sub>, 157 nm) became distributed, because of its very short wavelength [3.14]. The major mechanism and kinetics involved in a KrF excimer laser operation is shown as a flow chart in Fig.3.2

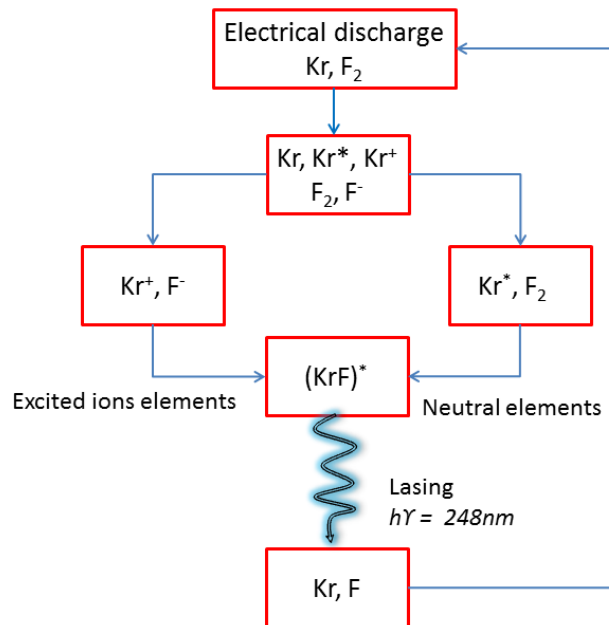


Fig. 3.2. Flow chart describing the kinetics of KrF laser operation.

In order to control the growth quality, it is very important to optimize the laser repetition rate. The laser frequency controls the amount of material to be ablated. The average flux ( $F_{av}$ ) of incident atoms can be given as:  $F_{av} = t_p \times f \times F_i$ , where  $t_p$  and  $f$  are the pulse duration of the incident flux and the laser repetition rate, respectively. In this relationship  $F_i$  is the instantaneous flux. A slower deposition rate

at a fixed pulse intensity means that the adsorbed species will be given more time, and a higher deposition rate will give less time to diffuse on the surface. Thus, the kinetics of growth may be very well controlled by laser frequency and fluence [3.15].

### Experimental set-up used

The deposition chamber set-up used is shown in Fig. 3.3 (b) and in the schematic drawing in Fig. 3.3 (a).

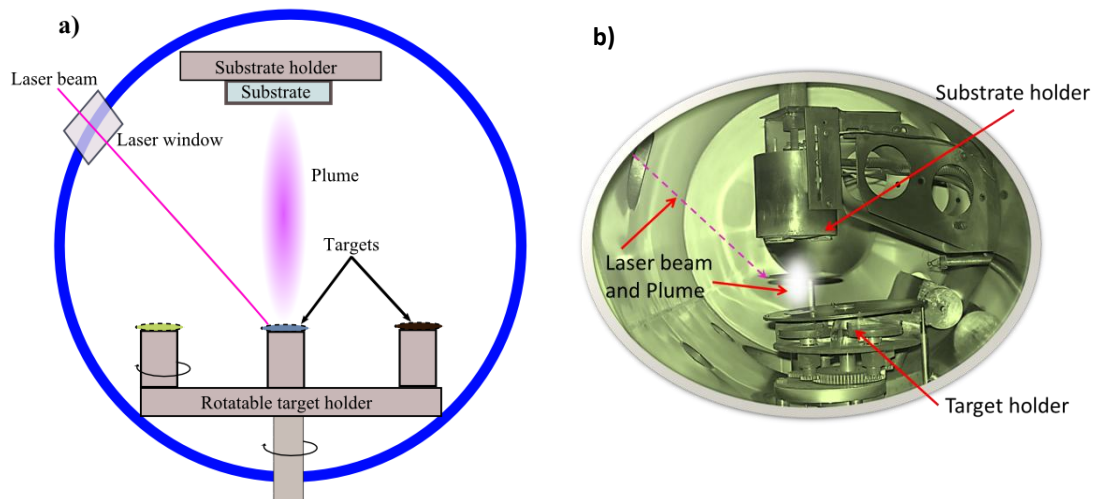


Fig. 3.3. PLD chamber used for the thin film preparation. (a) Schematic of the PLD chamber. (b) experimental set-up of the PLD chamber used.

It consists of a target holder and a substrate holder which are separated typically by a distance of 5.5 to 6 cm. The surface of target and substrate are parallel to each other in our set up. The substrate holder is equipped with a heating element and a thermocouple for the temperature measurement during the whole deposition process. The heater can heat the substrate up to 1000 °C. The chamber can load simultaneously four targets together for the *in-situ* preparation of electrode, films and optionally multilayers. The target positions can be changed from outside according to the specific process. The target holder is attached to a motor which keeps it rotating during the deposition process in order to avoid any chance of compositional change during the whole deposition process. The chamber can be filled with various gases such as oxygen, argon or nitrogen for the different background gas atmospheres through an automatically controlled gas inlet for the different gases. The chamber is equipped with a standard vacuum pump unit, where a turbo pump is backed by a rotary pump. The chamber can be evacuated up to  $1.0 \times 10^{-7}$  mbar. The chamber used is also provided with a RF sputtering unit. The PLD part of the chamber is attached to a high-power excimer KrF laser as an external energy source to vaporise materials

for the growth of thin films. A typical set of optical components (aperture, windows, mirrors, lenses) is placed in between the laser and the vacuum chamber to focus and boost the laser beam over the target. An aperture is used here to cut off the lower energetic edges of the laser beam and obtain a homogeneous energy profile. An excimer laser (LPX300 by Lambda Physics) with KrF as the excimer molecule, and Ne as a buffer gas, was used in our set up. In case of PST, the energy gap is around 3.4 eV and the used excimer laser with a wavelength of 248 nm corresponds to a photon energy of 5 eV, thus providing the facility to ablate the target material at low laser fluence.

### Target preparation

To have good quality growth, it is very important to have dense and homogeneous targets. In order to avoid droplets and particles during the growth, one needs to make sure that the targets have a smooth surface. The PST target used for growth of PST thin films in this thesis work was self-made, having quite a good density (around 80% of the theoretical density). The target was prepared by conventional solid state reaction method [3.16]. For the *PST* target, relevant oxide powders PbO (99.9%, Alfa Aesar), Sc<sub>2</sub>O<sub>3</sub> (99.9%, Alfa Aesar), Ta<sub>2</sub>O<sub>3</sub> (99.85%, Alfa Aesar) were mixed in appropriate ratio by ball milling in ethanol for 10 hours. In order to compensate the Pb losses during sintering and deposition, 10 mol% excess of PbO was added. The ball-milled mixture was dried and then calcined at 1000 °C for 12 hours in air to obtain the intermediate oxide as the precursory material. Then, the precursory material was thoroughly mixed, reground, and pressed into pellets with a size of 35 mm in diameter and finally targets were sintered at 1200 °C for 12 hours in a lead oxide atmosphere. The quality of the target was tested by XRD. All other targets with 99.9% purity used in this work were purchased from PRAXAIR.

In order to avoid any compositional and topographical changes, the targets were re-polished to smooth surfaces after each deposition.

### Background gas used and pressures

Generally, oxygen is used as background gas for the deposition of ferroelectric oxides. It helps first in providing the right oxygen stoichiometry and then in controlling the deposition rate. In the presence of oxygen as background gas, there is significant reduction in the kinetic energy of the vapour flux (reducing the deposition rate) reaching the surface during the deposition process. This high oxygen flux might change the film and substrate surface energies and will increase the oxygen content which is important for the ferroelectric oxide film nucleation process. In the PLD process a large amount of material is deposited in a very short time, separated by periods with no vapor flux [3.15]. Thus, it is necessary to have a high flux of oxygen available to oxidize and thermalize the species arriving at the surface of the

substrate. The presence of oxygen reduces the speed of the highly energetic particles through collisions, thus helping to protect the surface of the substrate. Due to the collisions of the particles with the oxygen atoms, lead oxide (PbO) is formed as a precursor for the formation of the film [3.17]. Further it reduces the vapour pressure of the metals used in the targets, helping to retain the composition of the films.

### 3.1.2 Radio frequency sputtering

As mentioned earlier, the PLD chamber used for the depositions is equipped with a RF sputtering unit. Sputtering is a phenomenon of knocking out the target atoms physically by a bombardment with Ar ions. Generally, the chamber is filled with Ar gas, and it is employed with a high voltage to produce a plasma. For the electrical measurements, Pt was deposited as top electrodes through a metal shadow mask of electrode size of approximately  $60 \times 60 \mu\text{m}^2$  by radio frequency sputtering at room temperature. Before the electrode deposition, the chamber was pumped down to  $5 \times 10^{-6}$  mbar, and then Ar was introduced into the chamber until the sputtering starts. Once the sputtering process starts, the Ar pressure was reduced to  $2.5 \times 10^{-3}$  mbar. A typical deposition rate was 30 nm/min with an input power of 40 W.

#### Parameters used for the depositions

The deposition parameters were optimized for the good growth after several trials. The listed parameters were used for the growth of the different films.

Material	Laser fluence (J/cm <sup>2</sup> )	O <sub>2</sub> -Pressure (mbar)	Frequency (Hz)	Substrate Temperature (°C)
PST	1.5	0.270	2-5	550
SRO	2	0.140	5	650-700
LNO	2.5	0.100	5	650
LSMO	2.8	0.140	5	650
CeO <sub>2</sub>	2.8	$4.5 \times 10^{-3}$	5-10	700
YSZ	2.8	$4.5 \times 10^{-3}$	5-10	700

Table 3.1. List of deposited materials with corresponding target materials and PLD parameters.

## 3.2 Structural characterization

### 3.2.1 X-ray diffraction (XRD)

X-ray diffraction is a non-destructive technique which is used to identify the crystalline phase and analyze the crystallographic structure of a solid material. Further, in thin films, it can be used to characterize the thin film parameters like orientations, epitaxy, and stress. If the wavelength of the X-ray radiation and the angle of diffraction is known, then the distance between the atoms in a crystal can be calculated by using a simple trigonometric calculation derived from Fig. 3.4,

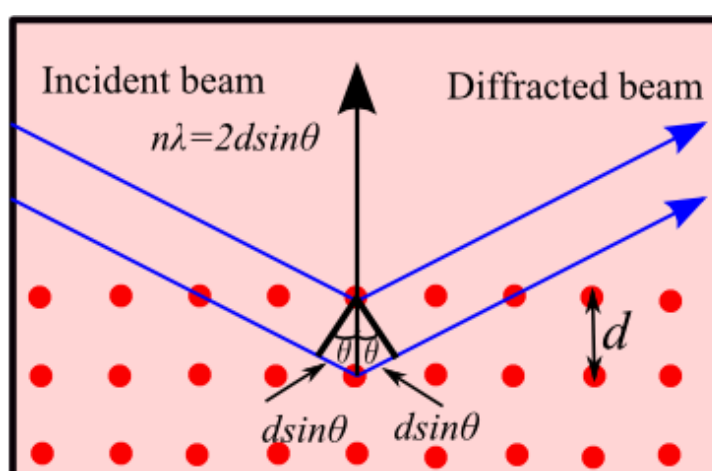


Fig. 3.4. Schematic of lattice planes describing the basics principle used for the X-ray diffraction measurements.

$n\lambda = 2d\sin\theta$ , where  $n$  is an integer (we use 1 for most calculations),  $\lambda$  - the wavelength of the x-ray (1.54 Å if copper is the target),  $d$  - the distance between atoms in angstroms, Å,  $\theta$  - the diffraction angle in degrees. This relationship is known as de-Bragg equation.

By calculating the distance and angles between the atoms of a substance, the structure of the crystal can be determined. X-rays are electromagnetic radiations with a wavelength of 0.01 - 10 nm and photon energies in the range of 100 eV-100 keV. For the diffraction purpose, only short wavelength X-rays in the wavelength range of 0.1 angstrom are used. The wavelength of X-rays is comparable with the interatomic distances in crystals (0.15–0.4 nm). Thus, a phenomenon of constructive and destructive interference is observable when a crystal is exposed to X-rays. The X-rays can penetrate deep into the material and give detailed information about the structure of the material. Each crystalline material has a unique XRD pattern, thus

XRD can be called a finger print for the material's identification and its structural investigation.

A simple X-ray diffractometer consists of an X-ray source, detector and a goniometer. The X-rays are produced by using a tungsten filament and heavy metal as anode. Cu, Mo, Fe and Cr are used as anode. When a sample is loaded inside the diffractometer and exposed to X-rays, the X-rays from the source interact with the sample and the resultant diffracted beam is collected by the detector. Only Bragg-diffracted X-rays form constructive interference patterns, hence resultant patterns. High-intensity characteristic peaks are always superimposed on a low-background continuous radiation. The characteristic radiation (which consists of several wavelengths) along with the continuous spectrum is then filtered by using an absorptive filter, a crystal monochromator, a wavelength-selective detector or a combination of these devices.

### Experimental set up used for XRD

A four-circle Philips X'Pert diffractometer is used for the structural investigation of the targets as well as the PLD prepared films. A typical scheme of a four-circle diffractometer is shown in Fig. 3.5.

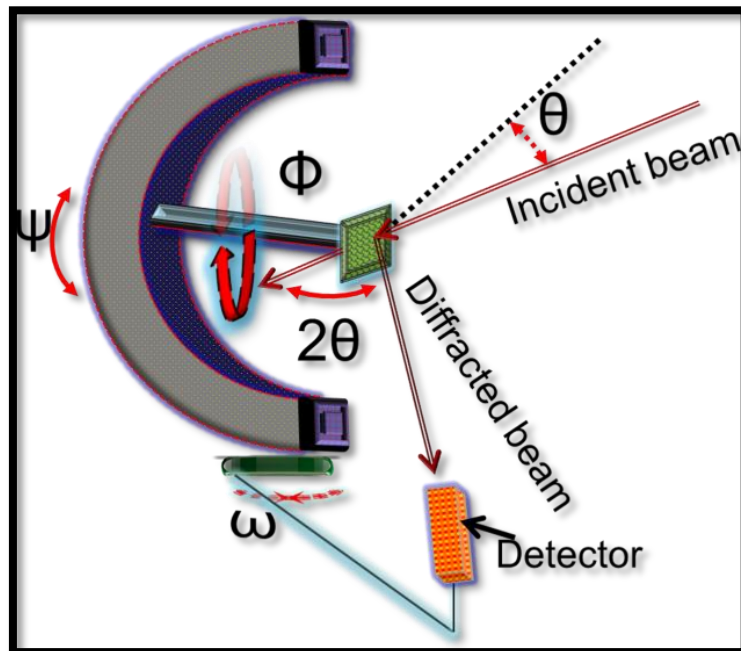


Fig. 3.5. Schematic of a four-circle diffractometer used for the X-ray diffraction measurements.

The X-ray tube is equipped with a monochromator for the Cu  $K\alpha$  radiation ( $\lambda=0.154$  nm). It was operated at a voltage of 50 kV and a current of 30 mA. Three types of X-ray scans were performed using the diffractometer, which are explained below.

### **$\theta$ - $2\theta$ Scans**

In the  $\theta$ - $2\theta$  scan the X-ray tube is stationary, the sample moves by the angle  $\theta$  and the detector simultaneously moves by the angle  $2\theta$ . When the Bragg condition is satisfied, diffraction occurs and provides information about the interatomic spacing of the planes parallel to the surface of the substrate. Before starting each measurement, the angles  $\varphi$  and  $\psi$  are optimized in order to get the maximum possible intensity.  $\psi$  is the angular tilt of the sample with respect to the X-ray beam and  $\varphi$  is the rotation angle of the sample with respect to the incident X-ray beam. The sample can be rotated by  $360^\circ$  and tilted up to  $90^\circ$  in one direction. This kind of measurements (where  $\psi = 0^\circ$ ) is also known as out-of-plane measurement, because it provides the information from only those planes which are parallel to the surface of the substrate. These measurements provide information about the out-of-plane lattice constant, film strain, phase purity, and out-of-plane crystallographic orientation.

### **In-plane Scans**

The  $\theta$ - $2\theta$  scan provides only information about the planes parallel to the sample surface, but it doesn't give any information on the planes that are orientated away from parallel to the surface. Thus, to obtain the full information one needs to perform in-plane measurements which are universally known as phi ( $\varphi$ ) scans. In phi measurements, the sample is moved to the angular position to satisfy the Bragg condition for a specific reflection, and a set of planes not parallel to the surface of the substrate (where  $\psi \neq 0^\circ$ ) is varied through the  $\varphi$  angular space while all other angles are kept fixed. A phi scan provides the information about the in-plane alignment of the films with respect to the substrate. Several  $\theta$ - $2\theta$  scans and  $\varphi$  scans are sufficient to determine and to confirm the film orientation with respect to the substrate orientation. Often it is difficult to determine whether the film has also other minor orientations, which cannot be distinguished in a  $\theta$ - $2\theta$  scan, because of a relatively weak peak intensity or because of an overlap of film peaks with substrate peaks. Thus, performing a pole figure plot of ( $\varphi$  -  $\psi$  scan) the sample will provide all the necessary information about the orientations of the sample. The pole figure plot is equivalent to a stereographic projection, showing the intensity of a known d-spacing in a certain direction. In pole figure measurement,  $\varphi$  scans are performed at all  $\psi$  angles (from  $0^\circ$  to  $90^\circ$ ), resulting in a pole figure for a certain  $2\theta$  angle. In a typical pole figure measurement, the  $\theta$  angle is fixed for a chosen direction of the film, and angles  $\varphi$  and  $\psi$  are varied. In this way, it covers all the possible directions of the chosen direction and gives a global information about the film orientation.



### Reciprocal space maps

Reciprocal space mapping (RSM) is used to study and determine the structural properties such as layer tilt, lattice relaxation and structural quality of epitaxial thin films. The reciprocal space lattice is a set of imaginary points constructed in such a way that the direction of a vector from one point to another coincides with the direction of a normal to the real-space planes, and the separation of those points (absolute value of the vector) is equal to the reciprocal of the real interplanar distance. It is also called Q-space, and the x,y, and z axis in Q space can be defined as  $Q_x$ ,  $Q_y$  and  $Q_z$ . RSM is a measure of the scattering intensity distribution of a reciprocal area in  $Q_x$ , and  $Q_z$ . This can be obtained by joining together successive one-dimensional scans in Q space. Thus RSM is a collection of many consecutive  $\omega$ - $2\theta$  scans or rocking curves with an offset in  $\omega$  value. In a rocking curve, the sample is moved to the angular position to satisfy the Bragg condition ( $n\lambda = 2d\sin\theta$ ) for a specific reflection, and then the sample is swept through the  $\omega$  angular space while the detector ( $2\theta$ ) is kept fixed. When these curves are transformed into reciprocal space, this results in meaningful intensity contours around the specific reciprocal lattice point which represent the actual structural quality of the specific crystal plane in real space. In a reciprocal lattice map,  $\omega$  scan shows the orientation variations of a defined inter-planar spacing, while the  $\omega/2\theta$  coupled scan shows the inter-planar spacing of the same orientation [3.18]. Hence elongations of the intensity contours along both  $\omega$  and the coupled  $\omega/2\theta$  scan directions are very informative. From the  $\omega$  and  $\theta$  angles the reciprocal coordinates  $Q_x$ , and  $Q_y$  can be determined by using the relationships [3.18]:

$$Q_x = \frac{\cos \omega - \cos(2\theta - \omega)}{2} \quad (3.1)$$

and

$$Q_y = \frac{\sin \omega + \sin(2\theta - \omega)}{2} \quad (3.2)$$

The in-plane and out-of-plane lattice parameters are calculated from these reciprocal coordinates using the wavelength  $\lambda = 1.5405 \text{ \AA}$  (for Cu  $K_\alpha$ ) of the X-rays and the miller indices  $h$  and  $l$  of the investigated plane:

$$a = \frac{\lambda h}{2Q_x} \quad (3.3)$$

and

$$c = \frac{\lambda l}{2Q_y} \quad (3.4)$$

### The Rietveld method

The Rietveld method allows to determine the crystal structure from powder diffraction data via a refinement of an initial structure model to the diffraction pattern, using the least-squares algorithm (Rietveld, 1969). This method fits point-to-point the difference between experimental intensities of the whole X-ray pattern and the calculated intensities, based on a certain model of crystalline structure, optical effects of diffraction, instrumental factors and other characteristics of the sample. More details of this technique can be found in Ref. [3.19]. The EXPGUI software is used for the refinement of the PST target. EXPGUI is a graphical interface for the Los Alamos GSAS package [3.20].

### 3.2.2 Atomic force microscopy

Atomic Force Microscopy (AFM) is a powerful version of scanning probe microscopy (SPM) where a small probe is scanned across the sample to obtain information about its topography. The inability of the scanning tunneling microscopy (STM) to measure the surface morphology of non-conducting samples led to the development of the atomic force microscope in 1986 [3.21]. This enabled the detection of atomic scale features on a wide range of insulating surfaces that include ceramic materials, biological samples, and polymers. Besides giving the information about surface topography, it also provides information about the growth process of thin films. Thus, AFM is very useful for the analysis of substrate surfaces for thin film applications, roughness analysis and grain size analysis. An AFM is operated in three modes, namely, contact mode, non-contact mode and tapping mode. The surface of the sample is scanned by a very sharp tip attached to a cantilever. The cantilever position is affected, *i.e.* deflected, by interactions between the tip and the atoms in the sample. A low-power laser beam is focused on the cantilever and the movement of the cantilever is detected by the reflected laser beam which falls on to a quadrant of a photodiode. The cantilever deflection gives the information about the topography of the sample surface. In tapping mode, the cantilever is typically made of Si as is the tip material and oscillates in free air at its resonant frequency. The tapping mode operation has the advantage to investigate the sample surface state without its modification. In contact mode operation, the static tip deflection is used as a feedback signal. However, close to the surface of the sample, attractive forces can be quite strong. Thus static-mode AFM is almost always done in contact where the overall force is repulsive. Consequently, this technique is typically called "contact mode". In contact mode, the force between the tip and the surface is kept constant during scanning by maintaining a constant deflection. In addition, the

contact mode also facilitates the application of an electrical field to the sample during measurement.

There are different kinds of forces coming in to play when a tip approaches the sample surface. The forces include mechanical contact force, capillary force, chemical bonding, electrostatic force, Van-der-Waals force. The force most commonly associated with atomic force microscopy is an interatomic force called the Van-der-Waals force.

In the contact mode, the tip is held less than a few angstroms ( $10^{-10}$  m) away from the sample surface, and the interatomic force between the tip and the sample is repulsive. In the non-contact mode, the tip is held on the order of tens to hundreds of angstroms from the sample surface, and the interatomic force between the tip and sample is attractive.

A Digital Instruments 5000 AFM equipped with a MikroMasch NSC15/AIBS silicon cantilever (with a spring constant of  $40 \text{ Nm}^{-1}$ ) operating in tapping mode was used during this work.

### **Piezoresponse force microscopy**

The motivation for the development of piezoresponse force microscopy (PFM) was the necessity of non-destructive local measurement of the polarization at nanoscale and to image the ferroelectric domains with a resolution beyond the optical resolution. The first PFM measurements were done by Guthner and Dransfeld in 1992 [3.22]. Further with the modification and improvement in microscope techniques it was possible to visualize ferroelectric domains by the converse piezoelectric effect. Thus PFM became an indispensable technique for the study of ferroelectric structures, ferroelectric switching, direction of polarization and the ferroelectric limit [3.23-3.26].

PFM is an extension of the AFM technique, and it is based on the converse piezoelectric effect. A conductive tip is used as top electrode to apply a voltage to the sample. In response to the applied field, the piezoelectric material locally changes its sizes (converse piezoelectric effect) as shown in Fig. 3.6. This response is mechanically transmitted onto the cantilever and can be optically detected by the movement of the reflected laser beam on the four-quadrant photo detector. The piezoelectric response having the same frequency as the excitation frequency can be extracted from the signal of the photo diode by using a lock-in amplifier. The PFM amplitude provides information on the magnitude of the local electromechanical coupling, while the PFM phase image gives the local polarization orientation.

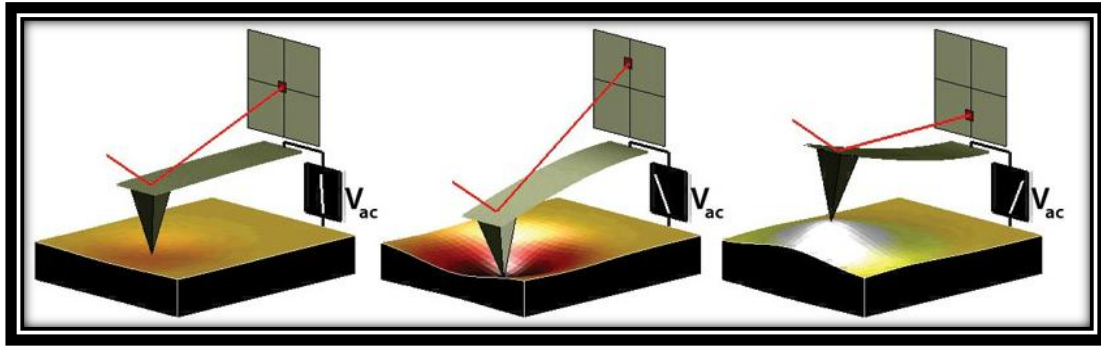


Fig. 3.6. Deformation of a sample in response to an applied AC voltage using an AFM conductive tip. It causes the cantilever to oscillate, which provides the information about the piezoelectric property of the material. Figure adapted from Ref. [3.29].

If the polarization is pointing away from the tip a positive voltage causes for *e.g.* an expansion of the film. The oscillations are in phase with the applied alternating voltage. If the polarisation is pointing towards the tip this causes a phase shift of 180°. More complete and detailed information on PFM can be found in Ref. [3.27-3.29].

In this work PFM was performed using a scanning probe microscope (ThermoMicroscopes) equipped with a PtIr coated tip (ATEC-EFM-20) with an elastic constant of about 2.8 Nm<sup>-1</sup>. Surface mapping and local hysteresis measurements were usually carried out applying an ac probing voltage at 25 kHz.

### 3.2.3 Transmission electron microscopy

Transmission electron microscopy (TEM) is an important technique used to characterize the microstructure of the film. By using TEM, various important information about the orientation of the thin film with respect to the substrate, cation-ordering and microstructure defects, like misfit dislocations at the interface, stacking faults, twins, and antiphase boundaries can be obtained. In 1923, de Broglie showed that all particles have an associated wavelength linked to their momentum. The dual nature of the particles can be explained by the de Broglie relationship given as:

$$\lambda = \frac{h}{mv}$$

where  $m$  and  $v$  are the relativistic mass and velocity, respectively, and  $h$  is Planck's constant. Further in 1927, Hans Busch showed that a magnetic coil can focus an electron beam in the same way that a glass lens is used for light. Five years later, a first image with a TEM was obtained by Ernst Ruska and Max Knoll [3.30]. In the transmission electron microscope, a high energy electron beam is transmitted through

a very thin sample to image and analyze the microstructure of the sample, nowadays with atomic-scale resolution. The electrons are focused with electromagnetic lenses and the image is observed on a fluorescent screen, or recorded on film or digital camera. When electrons are accelerated using a 200 kV acceleration voltage then the wavelength ( $\lambda$ ) of the electrons is 0.0251 Å, which is a very small value compared to the “diameter” of the atoms. However, the resolution of a TEM is not directly related to the wavelength, because it is limited by aberrations of the electro-magnetic lenses used in the microscopes. A reduction in the spherical aberration of the objective lens is a first step to increase the resolution limits in high-resolution microscopy. There are essentially three types of lenses used to form the final image in the TEM. These are the condenser, objective, and projector lenses. The condenser lens is used to concentrate and focus the beam of electrons coming off of the filament onto the sample to give a uniformly illuminated sample. The objective lens is the heart of the TEM and the most critical of all the lenses. It forms an enlarged image of the illuminated portion of the specimen in a plane that is suitable for further enlargement by the projector lens. When electrons are bombarded on the specimen, some of the electrons are just deflected from heavy atoms present inside the sample. Thus in order to eliminate these scattered electrons from the image, an aperture is placed in the objective lens that will stop all those electrons that have deviated from the optical path. The smaller the aperture, the more of these scattered electrons will be stopped and the greater will be the image contrast. Finally, the projector lens is used to project the final magnified image onto the phosphor screen. It is in the projector lens that the majority of the magnification occurs. Thus the total magnification is a product of the objective and projector magnifications. A high vacuum is maintained inside the TEM column, in order to avoid the strong interactions of electrons with foreign matter which could result in contamination of the TEM column and thereby in the deflection of electrons. The normal imaging modes in a TEM are bright field, dark field and electron diffraction. In bright-field imaging a relatively small aperture is placed in the back focal plane of the objective lens, which allows only the direct beam to pass through the objective lens effectively, and the scattered electrons are blocked by the aperture. In this case, the image results from a weakening of the direct beam by its interaction with the sample as shown in Fig. 3.7 (A). In dark field imaging the direct beam is blocked by the aperture while one or more diffracted beams are allowed to pass the objective aperture. Since diffracted beams have strongly interacted with the specimen, they carry a lot of information about planar defects, stacking faults or particle size. The intensity of the scattered electrons is higher close to the optic axis and, more importantly, further away from the optic axis the electrons suffer from aberrations from the electromagnetic lenses. If the diffracted beam selected by the objective aperture is off-axis, then the image recorded in this way is called a “displaced aperture dark field” image; this situation is schematically depicted in Fig. 3.7 (B) However, dark-field imaging is improved (due to strongly reduced aberrations) if the diffracted beam is centered on the optic axis of the objective lens. As shown in Fig. 3.7 (C), this is possible by tilting the incident

beam and then a centered dark field image is recorded. If a large objective aperture is used to include both the direct beam and some of the diffracted beams, they will interfere with each other. This will create a phase contrast which is used to generate HRTEM images. If the point resolution of the microscope is sufficiently high and a suitable crystalline sample oriented along a zone axis, then high-resolution TEM (HRTEM) images are obtained [3.30, 3.31].

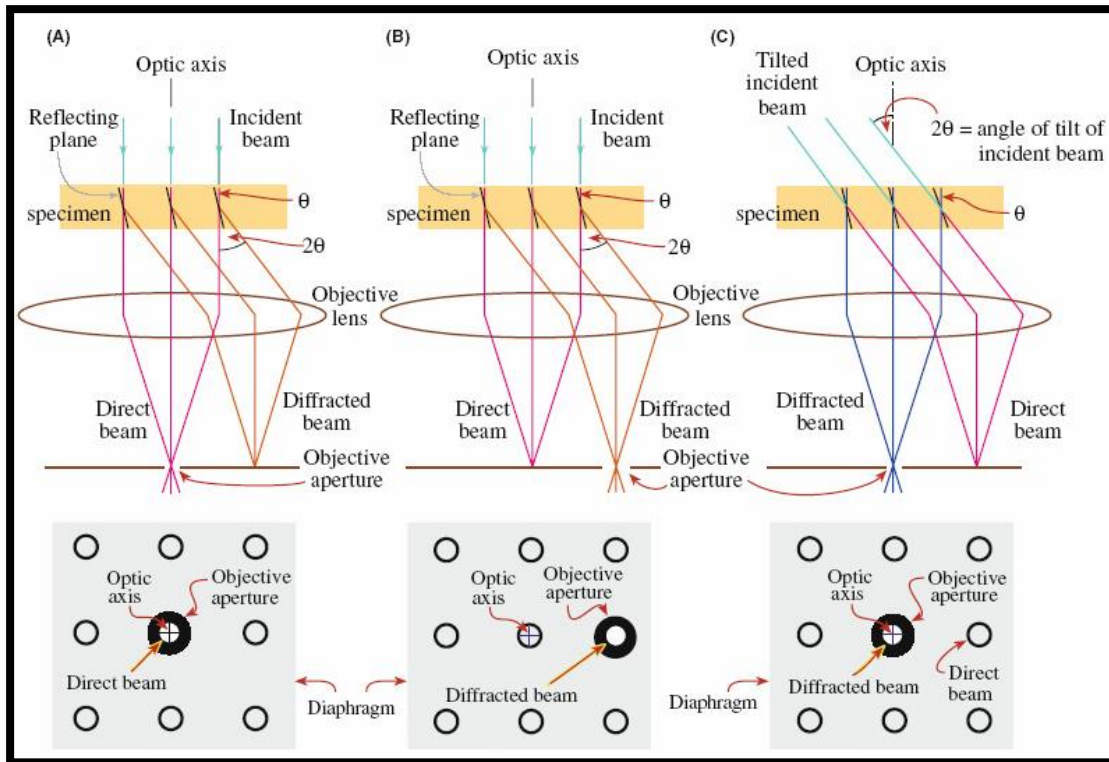


Fig. 3.7. Ray diagrams showing different operational modes in TEM. (A) Bright-field image formed from the direct beam; (B) Displaced-aperture dark-field image formed by using the aperture to select an off-axis diffracted beam; (C) Centered dark field image formed by tilting the incident beam such that the desired diffracted beam leaves the specimen centered to the optic axis of the objective lens. Figure adapted from Ref. [3.30].

When electrons elastically hit a sample, if the sample is crystalline, a diffraction pattern is created due to constructive interference under the conditions given by Bragg's law as explained in the XRD section. Instead of an objective aperture, now a selected area aperture is used to select the required area of the sample from which the diffraction pattern is obtained, as shown in Fig. 3.8. In this thesis, in order to investigate epitaxial thin films in both plan-view and cross section geometry using electron diffraction patterns, bright-field, and dark-field images, a Philips CM20Twin electron microscope was employed at primary beam energy of 200 kV.

The high resolution TEM images (HRTEM) and high resolution scanning TEM images (HRSTEM) were obtained using a Jeol 4010 at 400 kV and a FEI TITAN 80-300 at a working voltage of 300 kV, respectively.

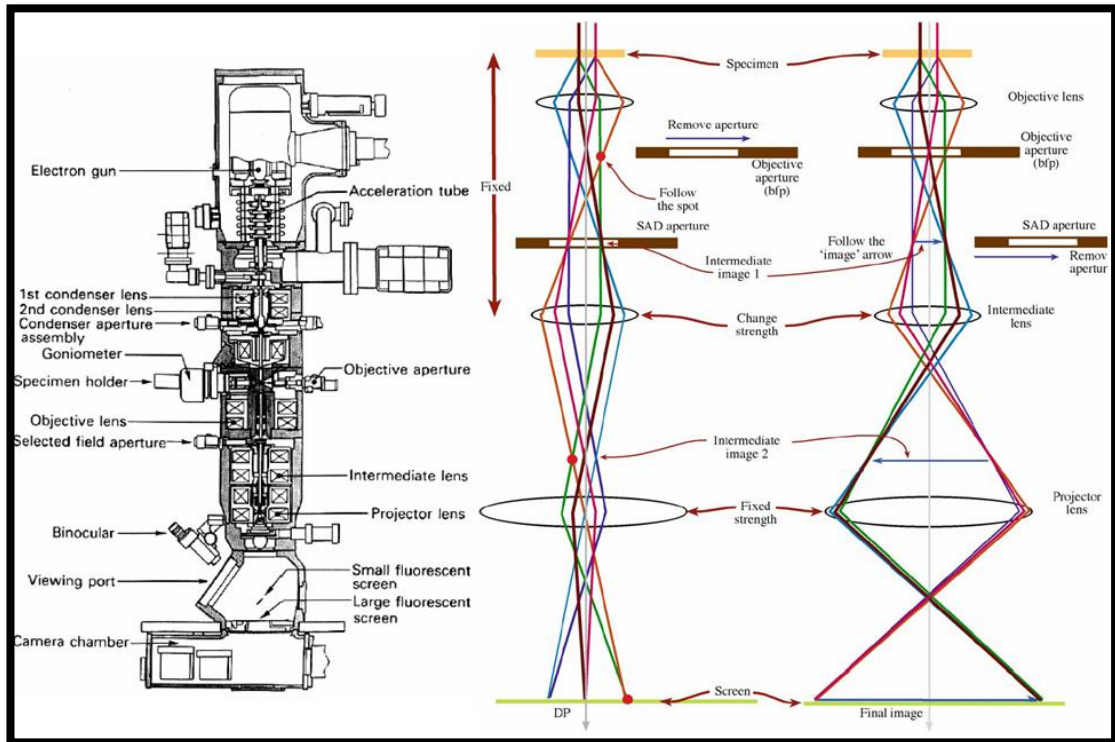


Fig. 3.8. (a) Cross section of a basic TEM [3.31]. Ray diagram of electron beams in TEM. (b) Selected area diffraction mode; (c) Imaging mode. Figure adapted from Ref. [3.30].

### Sample Preparation

Sample preparation is a necessary prerequisite for transmission electron microscopy. To be transparent to an electron beam, a sample must be made unimaginably thin; typically 100 nm or thinner. Many steps are involved to thin the sample. This is achieved by conventional method involving cutting, grinding, polishing, dimpling and ion milling. Most often the quality of the image is determined by the quality of the prepared specimen and not directly limited by the resolution of the TEM itself. Necessary care is required at each step during preparation in order to avoid artifacts. Both cross-sectional and plan-view specimens of samples are prepared by polishing and ion milling techniques. For the cross-section images, the sample is cut in two pieces of equal size and glued face-to-face. The glued sample is dried for 90 min at 150 °C under the constant pressure of a clamp. Further, it is cut in slices of 0.5 mm thickness and sanded and polished down manually to a thickness of 50-80  $\mu\text{m}$ . Next

the thickness of the slices is further reduced to 10-15  $\mu\text{m}$  with a dimple wheel and a polishing wheel attached to a Gatan Model 656 dimple grinder. The dimpled specimen is then glued on a copper ring with 1.5 mm diameter hole size using two-component epoxy resin which has to harden for 12 h. The region of the specimen outside the ring is removed. The sample is put into a Gatan Model 691 PIPS dual ion mill wherein the sample is thinned from one side by  $\text{Ar}^+$  bombardment. When a transmittable area becomes apparent the energy is reduced and the sample is polished from both sides to complete the preparation. For plan-view specimen preparation, a single slice of the sample having a thickness of 0.5 mm is polished from the substrate side only, with the film on the other side protected against damage. The rest of the specimen preparation procedure is similar to the one described above for cross section specimen. During ion milling the sample is only milled from the substrate side. In this way a hole from the back-side is produced, where the thin electron transparent edges of the hole contain the film, which can be observed in plan-view. More details on TEM methodology and sample preparation can be found in Ref. [3.30].

### 3.3 Electrical Properties

The ferroelectric properties of the films are characterized by measuring the polarization vs electric field (P-E) hysteresis loops by using an AixxACT TF Analyzer. Pt is sputtered as top electrode through a metal shadow mask of different sizes. Silver paste is used to connect the top electrode with the bottom electrode through a copper plate. The copper plate and the top electrode are contacted by W tips through a micromanipulator.

The setup for the ferroelectric measurements integrates the current with respect to the applied voltage delivering the polarization value. There might be different non switchable current contributions involved during the measurements, which can sum up as hysteresis loop in the final curve. The three major current contributions are: (1) displacement current, (2) conduction or leakage current, and (3) trapping current [3.32]. Thus a mathematical relationship for current and charge can be written as:

:

$$I(V) = I_L(V) + I_T(V) + I_D(V), \text{ where}$$

$$I_D = \frac{\partial D(V)}{\partial t} \text{ and } D = \epsilon_0 \epsilon E + P_S$$

$$Q(V) = \int_0^t I_L(V) dt + \int_0^t I_T(V) + D(V)$$

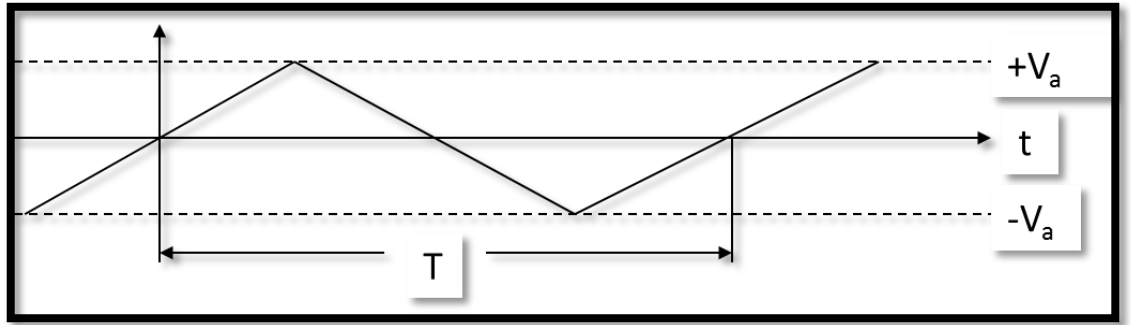


where  $I_L$ ,  $I_T$  and  $I_D$  are leakage, trap-emission and displacement currents respectively.  $P_s$  and  $Q$  are spontaneous polarization, and charge respectively. An ideal ferroelectric material should have negligible amount of leakage and trapping currents. Thus the above equations after ignoring the leakage and trapping current can be written as:

$$I(V) = \frac{\partial D(V)}{\partial t} = \epsilon_0 \epsilon_r \frac{\partial E}{\partial t} + \frac{\partial P_s}{\partial t} \quad 3.5$$

$$Q_s(V) = D(V) \quad 3.6$$

where  $Q_s$  is spontaneous charge. Triangular waveforms shown below were used to measure hysteresis curves. A typical waveform is shown below:



Now in order to convert the integral from the time scale to voltage scale, following equation can be used:

$$V = at \Rightarrow dt = \frac{1}{\alpha} dV, \text{ where } \alpha = 4V_a f \quad 3.7$$

After solving the equation 3.5 and 3.6 by using equation 3.7, the final relationships obtained for the charge and current can be written as:

$$Q_s(V) = \epsilon_0 \epsilon_r V + P_s(V) \quad 3.8$$

$$I = 4 \left( \epsilon_0 \epsilon_r + \frac{A}{d} \frac{\partial P_s}{\partial E} \right) V_a f \quad 3.9$$

Where,  $\epsilon_0$  is permittivity of vacuum,  $\epsilon_r$  is dielectric constant. As it is evident from the above equations, the hysteresis loops should not depend on the frequency whereas switching current depends on the measurement frequency. Thus P-V curves were recorded at different frequencies.

The dependence of the dielectric constant on the applied voltage is calculated from capacitance-voltage (C-V) measurements using a HP4194A Impedance Analyzer. Further, the phase transition measurements (C-T) are done in a cryostat by using liquid nitrogen.

## **Chapter 4.1 Results and discussions: Fabrication of cation-ordered PST films on SRO/STO**

This chapter discusses in detail the results obtained from the structural characterization of PST target and its epitaxial thin films prepared by PLD. The first section of this chapter describes the fabrication and structural characterization of the PST target. As explained in Chapter 1, thin films are important pillars for the development of modern technology. Thus, more efforts have been applied towards the fabrication of ferroelectric and relaxor thin films. Apart from the technological point of view, these materials and their respective thin films offer interesting physics. In its bulk state, PST is known as a normal ferroelectric or relaxor depending on the degree of cation-ordering. Although there are few reports about the degree of cation-ordering in sol-gel prepared films, cation-ordering in PLD grown films hasn't been reported so far. Thus the first part of this Chapter addresses fabrication of PST thin films by PLD, their microstructure, cation-ordering and electrical properties. PST has a rhombohedral structure and consequently larger polarization in the (111) direction in comparison to (100) direction. Thus two set of PST thin films with (100) and (111) orientations have been fabricated. The influences of microstructure and cation-ordering of the respective films on their electrical properties have been discussed. The last part of chapter will summarize the influence of thickness on the size of cation-ordered domains and various results obtained from the PST (100) and PST (111).

### **4.1.1 PST target**

PST thin films used in this work have been prepared using a self-made target generated by the solid-state reaction method. For the PLD process it is very important to have a high-density target with flat surfaces, as the quality and properties of the thin film very much depends on the surface and density of the targets [4.1.1]. Above 800 °C the volatility of Pb leads to a Pb deficient target due to a very high vapor pressure of PbO. In order to compensate for the Pb loss in the PST

target, 10% more PbO was used. The details of the PST target preparation are discussed in Chapter 3. The structure of the PST target was analyzed by XRD. The phase purity of the sintered target depends on the sintering time. It was found that the target which was sintered for five hours showed additional peaks indicating the presence of a secondary phase. The target which was sintered for ten hours showed a pure phase and all the peaks were identified assuming pseudocubic indexing [Fig. 4.1.1 (a)]. The density of the pure target has been calculated to be 80% of the theoretical value.

Based on the XRD measurements, a simulation was performed using Rietveld analysis (discussed in Chapter 3) in order to check out the phase purity. The simulations were carried out by using a  $Fm\bar{3}m$  space group. The results of these simulations as well as the difference between the simulated and experimental results are shown in Fig. 4.1.1 (b) of a target sintered for ten hours. The Rietveld refined parameters  $R_{wp}$ , and  $\chi^2$  are 0.1964, and 1.186 respectively.  $R_{wp}$  is called weighted profile R value. The fit of the calculated pattern to the observed data can be expressed numerically by agreement indices or  $R$  values.  $\chi^2$  is the ratio of  $R$  values of calculated and observed values. It should be around 1 for a good fit. Furthermore, the lattice parameter for the PST target as calculated from the fit is 8.142 Å, which is in good agreement with Ref. [4.1.2]. No pyrochlore phase was detected in this case. The degree of cation-ordering was measured in the PST target by calculating the order parameter  $S$ , which is defined as:

$$S^2 = \frac{I_{(1/2,1/2,1/2)} / I_{(1,1,1)} \text{ (observed)}}{I_{(1/2,1/2,1/2)} / I_{(1,1,1)} \text{ (calculated, } S = 1)} \quad 4.1.1$$

where  $I$  is the integrated intensity of the subscripted reflections. The value of the order parameter ( $S$ ) for completely ordered and disordered systems lies between 1 and 0, respectively [4.1.3]. The degree of cation-ordering has been found to be 85%.

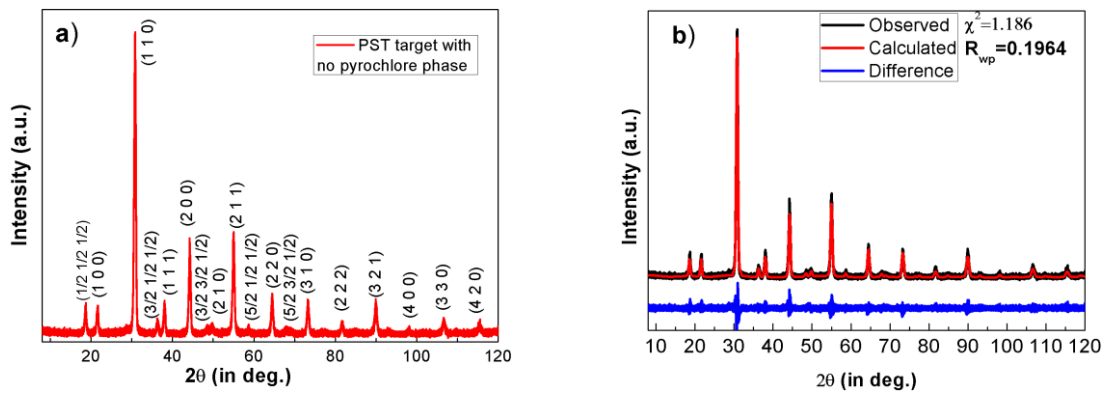


Fig. 4.1.1. (a) Observed XRD pattern. (b) Refined XRD pattern, blue pattern showing the difference between observed and calculated patterns.

### 4.1.2 Films deposition

It is very important to have an atomically flat substrate surface in order to have good quality growth of the top layer. As discussed in Chapter 2, an STO substrate has been used. It offers certain advantages compared to other substrates such as smaller mismatch when compared to LaAlO<sub>3</sub> (LAO) and greater stability when compared to MgO substrates. The mismatch between STO and PST (both considered to be pseudocubic) is -4.27%. This is smaller compared to the lattice mismatch between PST with LAO substrates. Also, there is a well-defined and simple procedure to etch and anneal the STO substrates in order to obtain well-defined TiO<sub>2</sub> terminated atomically flat terraces. The polished substrates (as obtained from the vendor *CrysTec GmbH*) were initially cleaned with distilled water and then etched in NH<sub>4</sub>F-HF solution for 18 to 20 seconds. The pH value of the solution was kept between 3.7 and 4.3. After the etching, the substrates were again cleaned with fresh distilled water, in order to remove the chemicals, and subsequently dried. Finally, the etched substrates were annealed at 900-1000 °C [4.1.4].

In order to enable electrical and piezoelectric measurements, PST films must be grown on conductive single crystal substrates. As the choices are very limited, a conductive epitaxial buffer layer is usually used as a bottom electrode. In the present case, SRO was used as a bottom electrode. Surface morphology of SRO determines the growth of the subsequent layers. Thus it is necessary to have a nearly perfect growth of SRO on STO. The lattice mismatch between STO and SRO is only 0.763% at RT (both considered pseudocubic). Because of a small lattice mismatch, SRO grows coherently on STO and hence promotes a good growth for the top oxide layer. Depending on the actual parameters, SRO can grow into three types of modes: step flow, step bunching or island mode. The growth mode can be tuned by changing the deposition parameters such as growth temperature, terrace width, and deposition flux. The bunching of SRO steps increases the surface roughness. Although this kind of growth might be attractive for use as templates for low dimensional structures, [4.1.5] it is however not desirable in the present case. Surface roughness and microstructure play an important role in the electrical properties of PST, as will be discussed later in the electrical measurements section. The most attractive growth mode is the one which keeps the substrate surface morphology unaltered. Thus, the step flow growth of SRO is highly desirable for promoting high quality growth of PST layers. The used STO substrates had a terrace width of about 200 nm, which corresponds to a miscut of about 0.1°. The deposition temperature was fixed to 700 °C for SRO growth during the entire deposition process. The background pressure was fixed to 0.141 mbar during the SRO deposition. It has been reported earlier that SRO grows in step bunching mode if the deposition flux is below a certain threshold value [4.1.6-4.1.7]. Thus we varied the deposition flux in order to get a step flow growth. In our case, films grown with a laser deposition flux of equal or less than 1.8 Jcm<sup>-2</sup> were found to have step bunching as shown in Fig. 4.1.2 (a). Upon increasing the laser flux between 2 to 2.5 Jcm<sup>-2</sup> the growth mode switched to a step flow growth

[Fig. 4.1.2 (b)]. A further increase in the laser flux to around  $2.8 \text{ Jcm}^{-2}$  lead to an island growth mode [Fig. 4.1.2 (c)], which is again not optimal.

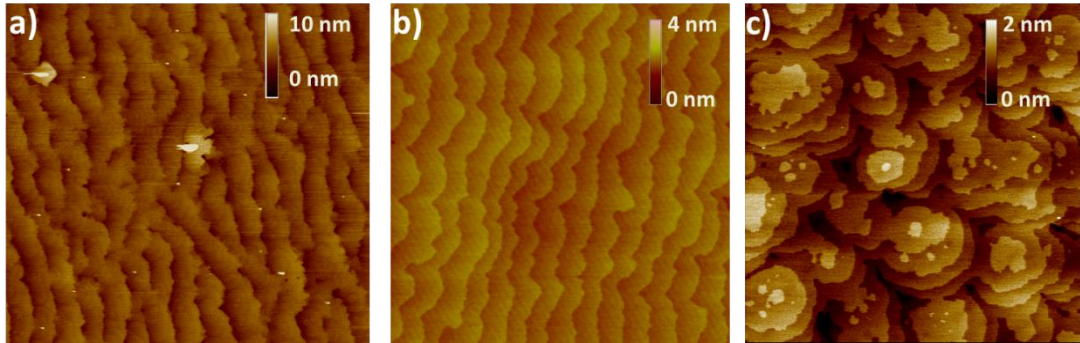


Fig. 4.1.2. Different growth modes of SRO depending on the deposition flux. (a) A  $10 \times 10 \mu\text{m}^2$  AFM image showing step bunching on using a low laser deposition flux of  $1.8 \text{ Jcm}^{-2}$ . (b) A  $4 \times 4 \mu\text{m}^2$  image showing a step flow growth with a used deposition flux of  $2 \text{ Jcm}^{-2}$  (c) An island growth mode ( $5 \times 5 \mu\text{m}^2$ ) at higher flux. For the island growth the laser flux was  $2.8 \text{ Jcm}^{-2}$ .

### PST thin films deposition

PST has a very narrow window of parameters, for the epitaxial growth of pure perovskite phase. The PST films deposited below and above  $550 \text{ }^\circ\text{C}$  were found to include of a pyrochlore phase. The films deposited with a higher laser fluence had a pyrochlore phase, whereas at low fluence poor ferroelectric properties were obtained. A similar kind of dependence was found for oxygen pressure. The films deposited at lower oxygen pressure were full of pyrochlore phases. The influence of some growth parameters on the microstructure and the electrical properties will be discussed later on in this chapter.

As discussed in Chapter 3, during the PST growth working pressure, laser fluence, laser frequency and substrate temperature were optimized to  $0.270 \text{ mbar}$ ,  $1.5 \text{ Jcm}^{-2}$ ,  $5 \text{ Hz}$  and  $550 \text{ }^\circ\text{C}$ , respectively. The distance between substrate and target was fixed to  $5.5 \text{ cm}$  for SRO and PST depositions. During the growth of PST films it was found that even a slight increase in temperature was capable of producing a pyrochlore phase. There is a fine balance between temperature and laser fluence for the growth of PST films without pyrochlore phase. Varying any one of the two parameters resulted in a pyrochlore phase. As the deposition temperature was increased to  $575 \text{ }^\circ\text{C}$  with a laser fluence of  $1.5 \text{ Jcm}^{-2}$ , a strong pyrochlore phase peak measurements as shown in Fig. 4.1.3 (a). A similar type of problem was found when the deposition flux was increased to  $2 \text{ Jcm}^{-2}$  while fixing the substrate temperature to  $550 \text{ }^\circ\text{C}$  as shown in Fig. 4.1.3 (c). Depositions under optimized conditions lead to a

pure perovskite phase as shown in Fig. 4.1.3 (b). The films were deposited *in-situ*, and after the deposition the films were cooled down to room temperature in a 1 bar oxygen atmosphere. Cooling in an oxygen atmosphere avoids the formation of oxygen vacancies. Films were cooled with a finite cooling rate of 5 °C /min.

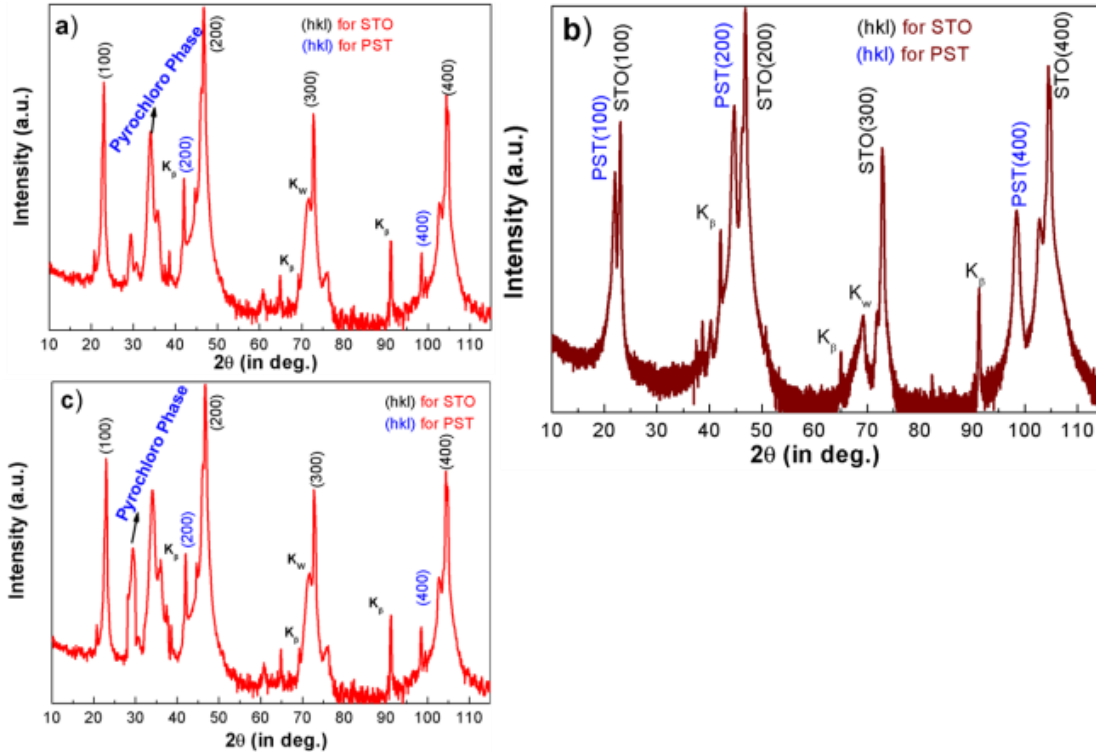


Fig. 4.1.3. XRD patterns obtained from different PST films deposited on SRO/STO. (a) A PST film deposited at 575 °C showing a pyrochlore phase; (b) An XRD of a pure perovskite phase of PST film deposited under optimized conditions; (c) A PST film having a pyrochlore phase deposited at high laser flux ( $2 \text{ Jcm}^{-2}$ ).

### 4.1.3 Microstructure of PST Films

As shown in Fig. 4.1.13. (b), the  $\theta$ - $2\theta$  scans for the films deposited under optimized conditions had a pure perovskite phase. Only (100) reflections were observed for both SRO and PST films, revealing *c*-axis oriented films. The additional peaks observed were identified as  $\text{CuK}_\beta$  radiation (marked by  $\mathbf{K}_\beta$ ), and a Tungsten (*W*) contamination of the X-ray target (marked as  $\mathbf{K}_w$ ). The SRO and STO peaks were not very well separated from each other especially for low angle reflections, because of their very similar lattice parameters. The out of plane lattice parameter for PST films has been calculated by using the XRD diffraction pattern, and it was found to be 4.047 Å

which is slightly less than the bulk lattice parameter. Further, in order to claim complete epitaxial growth of PST films, in-plane XRD measurements were performed. In these types of measurements, each of the material (STO, SRO and PST) was fixed at its respective  $2\theta$  angle for the (222) reflections and the sample was tilted by an angle ( $\psi$ ) of  $54.7^\circ$  in order to satisfy the Bragg condition for the particular (222) reflections. Then the sample was swept through azimuthal angles ( $\phi$ ), keeping all other angles fixed. The in-plane measurements for STO, SRO and PST contain four peaks for each material at the same azimuthal angle ( $\phi$ ), as shown in Fig. 4.1.4. This reveals that all the films were deposited cubically on substrates and onto each other.

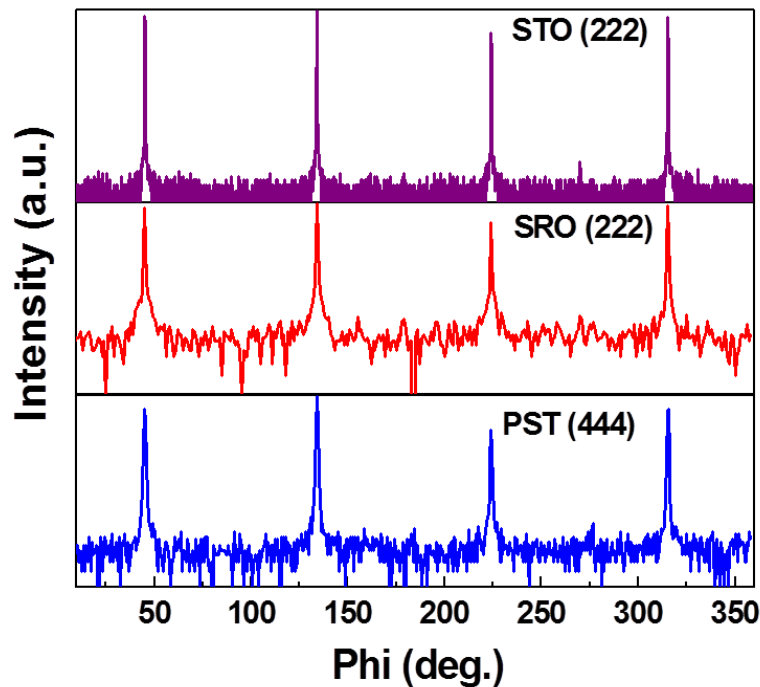


Fig. 4.1.4. A  $\phi$ -scan using the (222) reflections of PST and SRO thin films and of the STO substrate showing a four-fold symmetry. Four maximum intensity peaks appeared at an angle difference of  $\Delta\phi = 90^\circ$  to each other revealing a four-fold symmetry in the films.

The in-plane and out-of-plane epitaxial relationships between substrate (STO), electrode (SRO) and thin film (PST) have been found to be (001) PST// (001) SRO// (001) STO and (100) PST// (100) SRO// (100) STO, respectively (cubic indexing is used for SRO and PST). Furthermore, in order to check the PST and SRO growth quality on STO substrate, the full width at half maximum (FWHM) values for each layer, including STO substrate was calculated from in-plane measurements. The FWHM values along (222) reflections for STO, SRO, and PST were  $\sim 0.25^\circ$ ,  $0.89^\circ$ ,

and  $0.79^\circ$ , respectively. The FWHM values for SRO as well as for PST were quite close to the substrate values, confirming a good epitaxial growth.

The degree of cation-ordering in the PST films was calculated from the superstructure reflections. As the films are perfectly epitaxial, superstructure reflections thereby cannot be observed by normal  $\theta$ - $2\theta$  scans. In order to confirm cation-ordering in thin films, the sample was tilted by an angle  $\psi = 54.7^\circ$  so that the Bragg condition was fulfilled for the (111) planes. In order to observe the maximum intensity from (111) planes the azimuthal angle ( $\phi$ ) was fixed at the maximum intensity position obtained from  $\phi$  scans above. After calibrating the  $\phi$  and  $\psi$  angles, normal  $\theta$ - $2\theta$  scans were performed keeping all the other angles fixed. The superstructure reflections obtained in XRD measurements are shown below in Fig. 4.1.5.

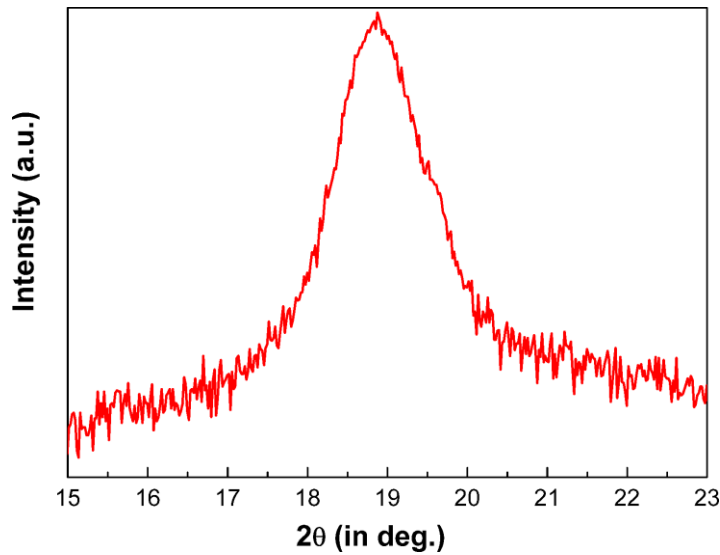


Fig. 4.1.5. A XRD pattern showing  $(\frac{1}{2} \frac{1}{2} \frac{1}{2})$  superstructure reflections near an angle of  $18.87^\circ$ .

The average degree of the cation-ordering was calculated by normalized integrated area of the superstructure peak  $(\frac{1}{2} \frac{1}{2} \frac{1}{2})$  to the normalized intensity of fully ordered PST. The reference peak (111) was used to normalize the intensity of the superstructure reflections in both fully ordered and experimentally obtained XRD patterns. Finally, using equation 4.1.1, the order parameter for two films of different thickness was found to be:  $S \sim 0.35$  for 60 nm and  $S \sim 0.38$  for 75 nm.

The surface morphology of the PST thin films was analyzed by AFM measurements. The measurements show a relatively smooth surface for the PST films grown under optimized conditions as shown in Fig. 4.1.6 (b). Terrace-type morphology was observed on the surface of the PST film, possibly due to a step bunching growth mode for the underlying SRO electrode film. The PST films have terraces with a step height of 3 nm, and the root mean square value of roughness for



the terraces was about 0.28 nm over an area of  $0.3 \times 0.3 \mu\text{m}^2$  signifying a flat and smooth surface, and revealing a good growth of PST over SRO and STO. However, the films grown under higher laser flux had very rough surfaces. The RMS value of roughness for these films was more than 2 nm for a  $4 \times 4 \mu\text{m}^2$  area. The films were grainy with average an grain size of 20 nm as shown in Fig. 4.1.6 (a).

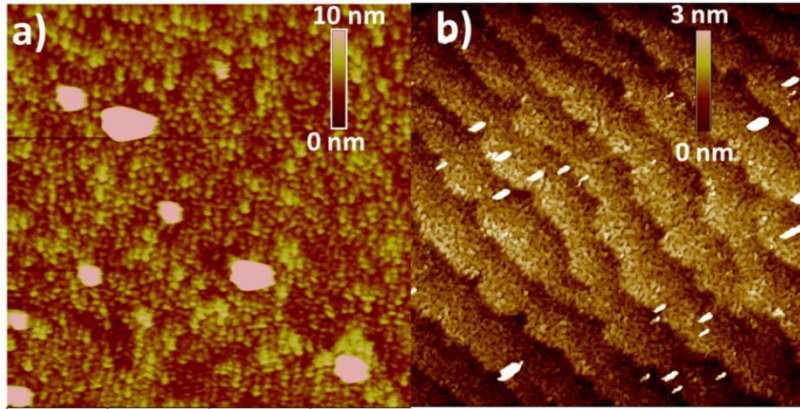


Fig. 4.1.6. An AFM image showing the topography of PST films. (a) A  $4 \times 4 \mu\text{m}^2$  image of PST film deposited with high flux showing a lot of droplets and high roughness. (b) A  $5 \times 5 \mu\text{m}^2$  optimized growth, showing the terrace-like structure induced by the substrate with low roughness.

#### 4.1.4 TEM investigations

The internal microstructure of the PST thin films was studied with TEM. Two optimized set of films with different thicknesses were analyzed by CM20T TEM, and HRTEM Jeol 4010. A cross-section TEM dark field image for the 60 nm thick PST film on 40 nm SRO is shown in Fig. 4.1.7. The other set of films has PST and SRO thicknesses of 77 nm and 78 nm, respectively. As shown by AFM (Fig. 4.1.6) SRO has good quality growth over STO substrate because of low lattice mismatch. Due to the large lattice mismatch between SRO and PST (3.53%), a high density of threading dislocations is observed in the cross-sectional TEM image shown in red circles in Fig. 4.1.7. In case of PST, when film thickness exceeds a critical thickness, misfit dislocations (MDs) are introduced to release the strain. The MDs give rise to threading dislocations (TDs) which propagate to the surface of the film. The critical thickness for the PST films was calculated and found to be around 6 nm by using Matthews and Blakeslee calculations [4.1.8]. The PST film's thickness is larger than the calculated critical thickness values, thus a high density of misfit dislocations is expected. The average spacing between the MDs was found to be approximately 10 nm, which is in accordance to theoretical values [4.1.8]. Fig. 4.1.8. shows an HRTEM image, where different defects inside the film can be seen. The defects in this figure are numbered. Defects numbers, 1 and 4 are threading defects while 2, 3 and 5 are misfit dislocations. The threading defect No. 1 extends through the entire

film through 1b, while defect No. 4 is terminated at 4b. A similar kind of threading dislocation emerging from the misfit dislocations and extending to the surface of the

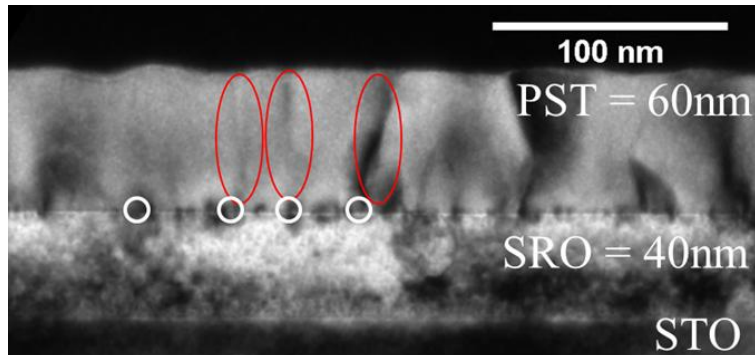


Fig. 4.1.7. A (010) cross-section dark-field image recorded using (002) reflections close to the [010] pole. Red colour circles highlight the threading dislocations. The white colour circles show the misfit dislocations.

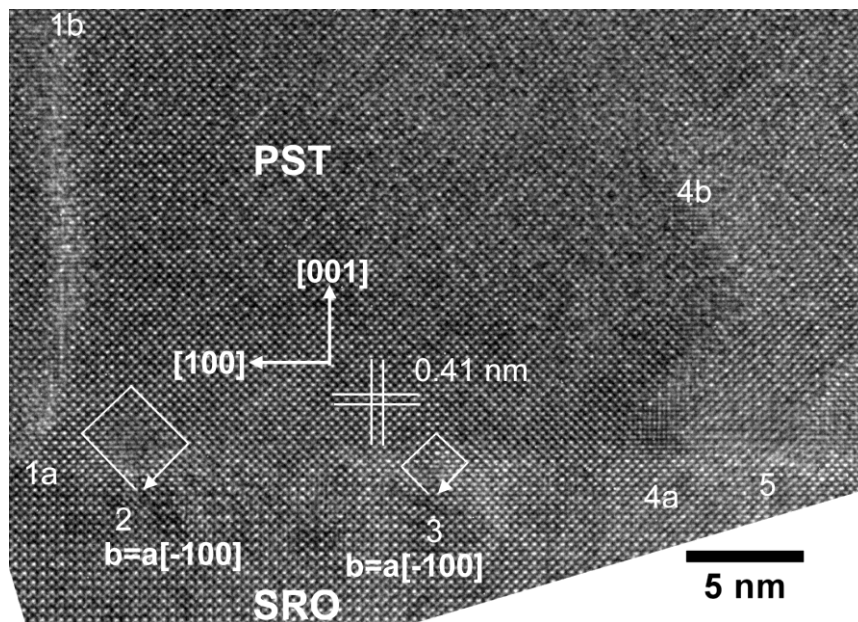


Fig. 4.1.8. A HRTEM cross-section image of the SRO-PST interface acquired along the [010] direction, showing the misfit and threading dislocations.

PST film is also indicated in Fig. 4.1.7 by red and white circles. Basically, misfit dislocations are a medium for PST films to release the misfit strain. More details about misfit dislocations and other dislocations can be found in Ref. 4.1.9. As it is clear from the cross-sectional image, PST has a columnar growth which can be attributed to a lattice mismatch between PST and underlying SRO layer. Moreover,

selected area diffraction (SAED) for the cross-section and the plane view sample is shown in Fig. 4.1.9 (a) and 4.1.9 (b), respectively. Only  $[100]$  type reflections were

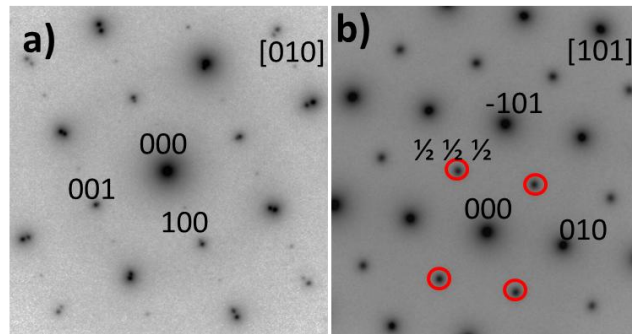


Fig. 4.1.9. TEM- SAED patterns for (a) cross-section sample along the  $[001]$  pole and (b)  $[101]$  poles of plane-view samples. The red colour circles highlights the set of superstructure reflections obtained.

obtained which supports the XRD measurements on epitaxial growth. It was found that in the case of the  $[101]$  pole position, additional sets of reflections were obtained which were indexed as  $(\frac{1}{2} \frac{1}{2} \frac{1}{2})$  reflections [shown in red circles in Fig. 4.1.8 (b)]. These reflections are called superstructure reflections. Similar reflections were observed in the XRD measurements. This supports our claim that PST thin films have a good degree of cation-ordering. Using superstructure reflections a dark field plane view image was obtained as shown in Fig. 4.1.10 (a-b). In the case of 60 nm thick PST films, the domain size of the cation-ordered regions was found to be 5 nm in a disordered matrix. The degree of cation-ordering was calculated by TEM investigations to be  $\sim 50\%$ . It was also found that for the 77 nm thick film, the domain size of cation-ordered regions was slightly larger than the PST 60 nm thick

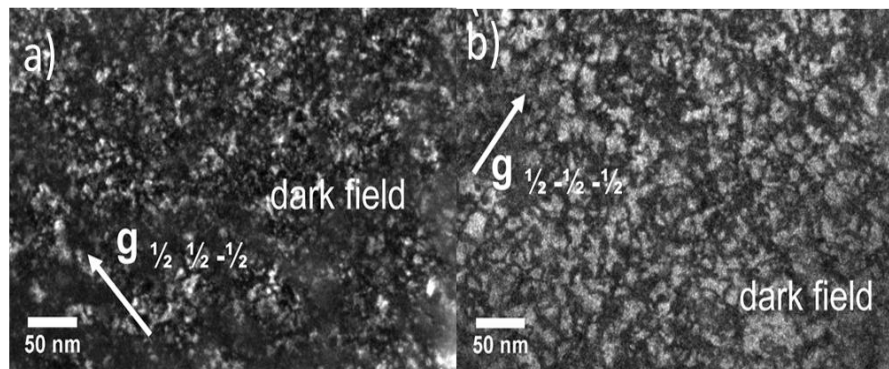


Fig. 4.1.10. A dark field plane view image captured by using  $(\frac{1}{2} \frac{1}{2} \frac{1}{2})$ - type reflections from two different PST films (a) Image of cation ordered domains of 5 nm size for 60 nm thick PST sample. (b) Cation ordered domain size of 10 nm for 77 nm thick PST film.

films. The ordered domain size was found to be  $\sim 10$  nm [Fig. 4.1.10 (b)]. An inverse Fourier-transform (IFT) image of the HRTEM image acquired along [110] direction at a very thin region for a 60 nm thick film is shown in Fig. 4.1.11.

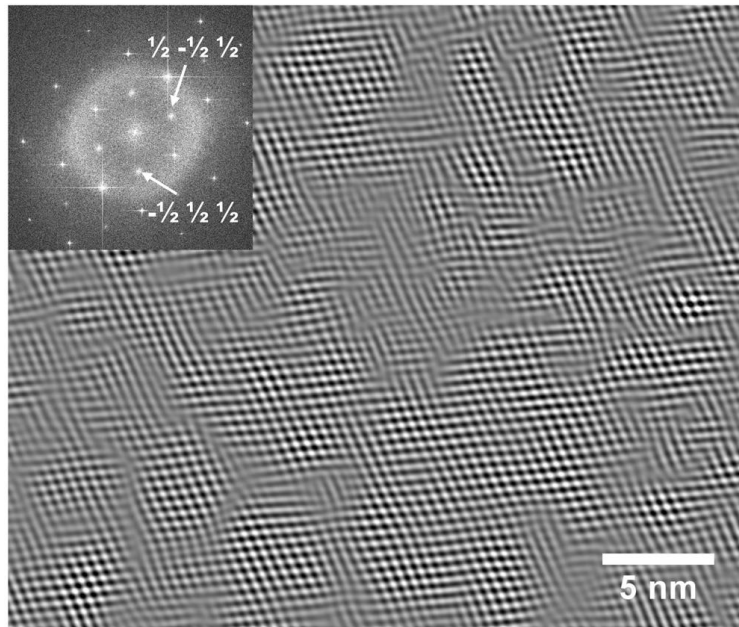


Fig. 4.1.11. IFT image using superstructure reflections of the HRTEM image acquired along the [110] direction at a very thin region. The Fourier transform of the HRTEM image is given in the inset.

The IFT image was formed using  $(\frac{1}{2} \frac{1}{2} \frac{1}{2})$  type superstructure reflections in the power spectrum (shown in the inset of Fig. 4.1.11) of the HRTEM image. Bright regions with a size of about 5 nm are observed. Further from SAED, a and c lattice parameters of the PST film were calculated to be 4.06 Å both, within measurement accuracy. In case of XRD the out-of-plane lattice parameter was smaller than that calculated through TEM. However, in the case of XRD a larger area of sample is analyzed, thus one can conclude that the average out of plane lattice parameter is 4.047 Å. Since in TEM the latter was found to be equal within our measurement accuracy, we can state that the strain in the PST film was completely relaxed.

#### 4.1.5 Electrical characterization of PST Films

The ferroelectric properties of PST thin films were analyzed using hysteresis loop measurements. The P-V loops were recorded at RT as well as at low temperatures. As explained in Chapter 3, top and bottom electrodes were connected using silver



paste. The electrical measurements were in top to bottom arrangement. The metal-ferroelectric-metal heterostructures needed for electrical measurements were obtained by sputtering the top platinum electrode through a metal mask. The role of bottom electrode was played by the epitaxial SRO layer. The P-V loops were recorded at 1 kHz frequency using a triangular waveform of applied voltage. Typical curves recorded at RT are shown in Fig. 4.1.12 (a-c). The hysteresis loop in Fig. 4.1.12 (a) belongs to a 60 nm thin film grown in optimized conditions.

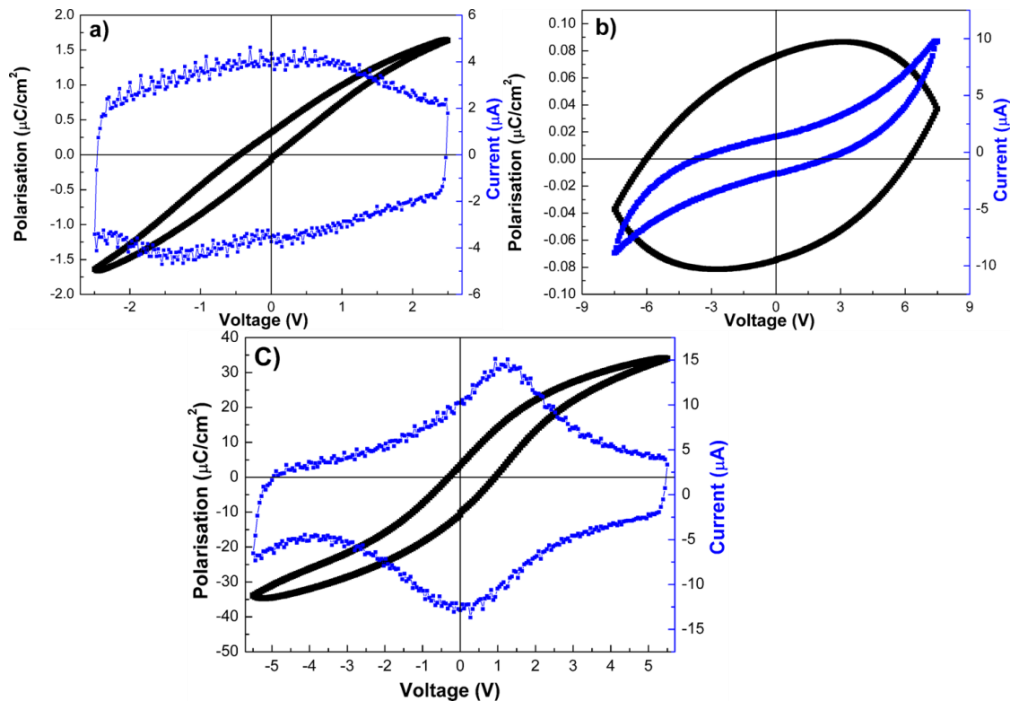


Fig. 4.1.12. Macroscopic polarization-voltage and switching current-voltage hysteresis curves of a PST film at RT. (a-c) ferroelectric hysteresis recorded for the (a) 60 nm thin film with 33% cation-ordering. (b) a film grown with higher flux and (c) a 77 nm thin PST film with 35% cation-ordering.

The films show ferroelectric properties with a remnant polarization  $P_r$  and a coercive voltage  $V_c$  of 0.3  $\mu\text{C}/\text{cm}^2$  and 0.28 V respectively. These values are higher than the previously reported one [4.1.10], which can be attributed to the influence of the cation-ordering and microstructure properties of these PST films. In addition, those films grown at a higher laser fluence and flux were found to have a rough surface morphology and a certain amount of pyrochlore phase, high leakage and no ferroelectricity as shown in Fig. 4.1.12 (b). Thus it is again obvious that it is crucial to control the growth of PST films in order to have a good microstructure, thereby engineering their ferroelectric properties. Fig. 4.1.12 (c) shows the hysteresis loop recorded for the 77 nm thick film. This film was found to show higher polarization when compared to the 60 nm thick film. The remnant polarization  $P_r$  and the coercive

voltage  $V_c$  of this PST film under the application of 5 V were found to be  $3.4 \mu\text{C}/\text{cm}^2$  and 0.6 V, respectively at RT. As discussed earlier in the TEM section, 77 nm thin films have larger-size ordered cation domains and more ordering than the 60 nm thin films. This leads to the conclusion that the degree of cation-ordering is responsible for the good ferroelectric properties. Ferroelectricity has also been investigated in low temperature range. The ferroelectric hysteresis loops have been measured for 60 nm thin films in the temperature range from 10 K to RT [Fig. 4.1.13].

In this case, the PST thin film was found to behave as a normal ferroelectric at low temperature. At 100 K, the remnant polarization  $P_r$  and the coercive voltage  $V_c$  of the PST film under the application of 5 V were found to be  $0.65 \mu\text{C}/\text{cm}^2$  and 0.55 V, respectively. As the temperature increases, the hysteresis loops become slimmer. No significant change either in the coercive field or in the remnant polarization was observed above 200 K. According to the superparaelectric model [4.1.11], relaxor materials were proposed to consist of polar nano regions (PNR) which have been proven experimentally [4.1.12-4.1.16]. On cooling in relaxors, the phase changes from a non-polar cubic to an ergodic relaxor phase. An ergodic phase consists of randomly distributed and oriented *PNR* in the cubic matrix. In an ergodic phase from the thermodynamical point of view, the average microscopic structural state over time does not yield any preferential polar direction. The temperature at which this phase transition occurs is known as burnt out temperature ( $T_B$ ). Below this temperature, *PNR* appear and are randomly oriented in different directions. On further cooling, *PNR* lose their dynamics to freeze into a non-ergodic phase, and sometimes directly into a ferroelectric state.

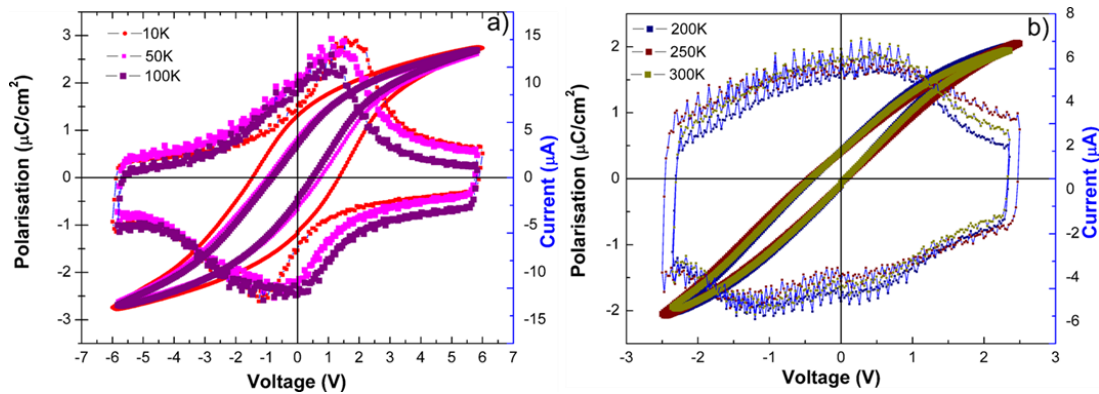


Fig. 4.1.13. (a-b) Macroscopic polarization-voltage and switching current-voltage hysteresis curves of a PST film at different temperatures.

A non-ergodic phase is cubic and on applying a strong electrical field it can be converted irreversibly into a ferroelectric state. In the case of PST, the phase transition temperature lies around RT or below, depending on the degree of cation-ordering. So at RT, PST thin films might be in the  $T_B$  temperature range. In this

range PST has randomly oriented PNR, which in response to the application of the electrical field transform into a ferroelectric state by aligning themselves in the opposite direction of the applied field. Upon further cooling, especially below 200 K, PST films enter into a proper ferroelectric state and hence show clear hysteresis and switching current-voltage characteristics.

The dielectric properties of these films were analyzed at RT. The dielectric constant for the 60 nm and 77 nm thick PST films was found to be 400 and 460 respectively, at 1 kHz frequency with losses lower than 0.01. These values are relatively low when compared to previously reported values on polycrystalline films [4.1.17]. A possible reason for this is the absence of extrinsic contributions to the dielectric constant, due to the high quality and the epitaxial nature of the PST films [4.1.18].

The local ferroelectric switching of the films was also investigated by PFM, as shown in Fig. 4.1.14. A modulation voltage of  $0.4 V_{\text{rms}}$  at 25 kHz was used and the tip loading force kept constant at 20 nN. When the films were scanned with an *ac* 0.4 V in the grown state, there was no signal observed as expected. In the second step, a  $3 \times 3 \mu\text{m}^2$  area was poled downwards by applying a voltage of +5 V for background poling. The background poling aligns the random ferroelectric domains in a direction opposite to the applied field. In the case of relaxors, randomly oriented polar regions align in the opposite direction to the applied *dc* field. Then, at the center, a smaller area of  $1 \times 1 \mu\text{m}^2$  was switched upwards by a voltage of -5 V. Thus, on scanning the whole  $3 \times 3 \mu\text{m}^2$  with an *ac* voltage of 0.4 V, the region poled with -5 V shows a different contrast, revealing that the films can be locally switched by applying an external voltage. An image of topography, phase and amplitude is shown in Fig. 4.1.14 (a-c.)

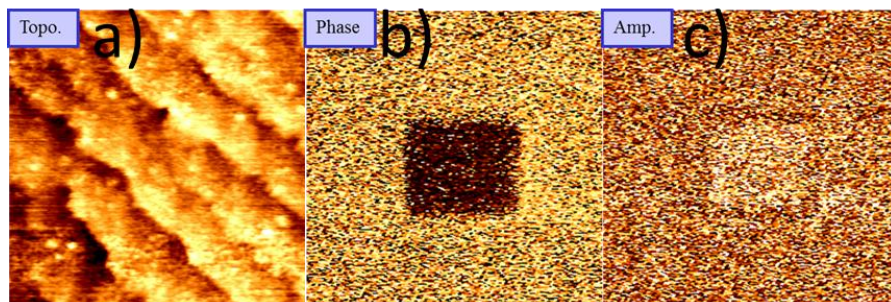


Fig. 4.1.14. A PFM piezoresponse image ( $3 \times 3 \mu\text{m}^2$ ) of a PST film (a) Topography of PST film (b-c) phase and amplitude image after switching a  $1 \times 1 \mu\text{m}^2$  area in the middle.

#### 4.1.6. Growth and microstructure of PST (111) thin films

PST has a rhombohedral structure. Thus, to explore maximum polarization, it is necessary to grow films in the (111) direction. PST (111) films were deposited on SRO/STO (111) substrates. While the (100) STO vicinal substrates are easy to obtain, the processing of STO (111) vicinal substrates is not documented. Substrates with a nominal miscut angle of  $0.1^\circ$  were cleaned in an ultrasonic bath and etched in  $\text{NH}_4\text{F}$ : HF=7:1 solution for 2 minutes and then heated at  $950^\circ\text{C}$  in  $\text{O}_2$  atmosphere for two hours. The AFM image of one of these substrates is shown in Fig. 4.1.15 (a). The step height of STO (111) terraces was found to be  $\sim 0.350$  nm. Both step height and terrace width were found to vary from substrate to substrate due to variations of the miscut angle. Moreover, some of the used substrates were having step heights of 0.151 nm and different step heights and widths were observed within one substrate. This shows that chemical etching does not reproduce a very clean and single step terraced (111) STO surface. An ideal etching on an STO (111) substrate should produce terraces of atomic step height (in this case  $\sim 0.25$  nm). This brings additional difficulties in growing high quality epitaxial (111) PST thin films. Similar growth conditions as

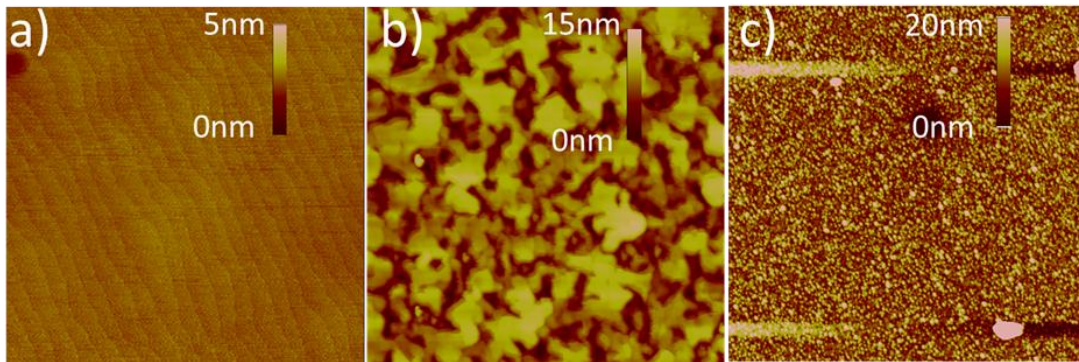


Fig. 4.1.15. AFM images recorded for (a) Etched and annealed STO (111) substrate showing irregular terraces for  $2 \times 2 \mu\text{m}^2$  area. (b) A  $2 \times 2 \mu\text{m}^2$  image of a PST thin film, showing island kind of growth. (c) Topography of PST film grown ( $1 \times 1 \mu\text{m}^2$ ) at higher temperature than the optimized temperature.

used for PST (100) and SRO (100) were used for the depositions of PST (111) and SRO (111). It was found that SRO does not grow in the step flow growth mode, but grows in the island mode which promotes later on a similar growth mode in PST films. Such island growth mode has been reported in literature for SRO (111). It is mostly due to irregular step terraces and different surface energy of STO (111) substrates [4.1.19]. A typical surface morphology of PST (111) films grown in situ



on SRO (111)/STO (111) is shown in Fig. 4.1.15 (b). The STO (111) substrate used for this growth had a surface roughness of  $\sim 0.2$  nm for a  $2 \times 2 \mu\text{m}^2$  area. The PST film has a surface roughness  $\sim 2.5$  nm for  $2 \times 2 \mu\text{m}^2$  area, which is significantly higher compared to PST (100) thin films. Similar to PST (100), PST (111) growth was very sensitive to temperature and laser fluence. Fig. 4.1.15 (c) shows a film grown at  $565$  °C with an optimized laser fluence of  $1.5 \text{ Jcm}^{-2}$ . With an increase in temperature, the film topography became grainier with average grain size of  $56$  nm. The film roughness increased and the RMS value of the roughness was found to be more than  $6$  nm for  $5 \times 5 \mu\text{m}^2$ .

The phase purity and epitaxy of PST (111) films was analyzed with XRD measurements. It was found that the films grown under optimized parameters have a pure perovskite phase without the presence of a pyrochlore phase. Fig. 4.1.16 (a-c) shows the normal  $\theta$ - $2\theta$  scans for PST thin films grown at different temperatures. Three sets of films were analyzed by XRD: One was grown at  $550$  °C and the other two sets were deposited at  $565$  °C and  $525$  °C, respectively.

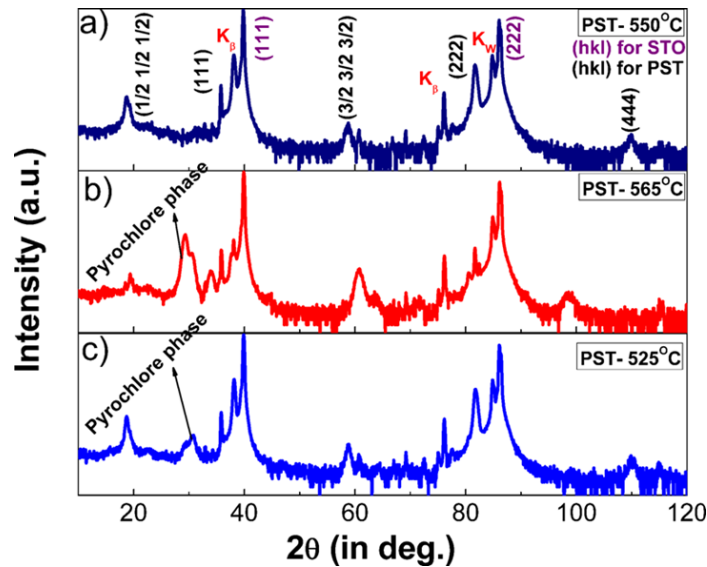


Fig. 4.1.16. XRD recorded for PST (111) films showing out-of-plane orientations (a) A pure perovskite phase film (b-c) PST films with a pyrochlore phase, grown at  $565$  °C and  $525$  °C.

As seen here, the two films which were grown at a temperature other than  $550$  °C were found to contain a pyrochlore phase. The PST films grown at optimized conditions were phase-pure and epitaxial. The superstructure reflections, which indicate the presence of cation-ordering, were directly observed in the  $\theta$ - $2\theta$  scans in the films. The degree of cation-ordering was calculated by using equation 4.1.1, and it was found to be around 33%. The in-plane-orientation of the PST films was evaluated by  $\varphi$ -scans performed for each layer including STO substrate. The  $\varphi$ -scans

were performed using the (200) reflections as shown in Fig. 4.1.17 (a-c). For the  $\phi$  scans, the sample was fixed at a specific value of  $2\theta$  for (200) reflections of each layer including STO substrate. In order to satisfy the Bragg condition for the (200) reflections, the sample was tilted at an angle  $\psi = 54.7^\circ$ . Keeping all other angles fixed, the sample was swept through an azimuthal angle from  $0^\circ$  to  $360^\circ$ . Three peaks were observed at same azimuthal angle for each material. Each of the peaks were separated from each other at an angle of  $\Delta\phi = 120^\circ$ , revealing a cube on cube

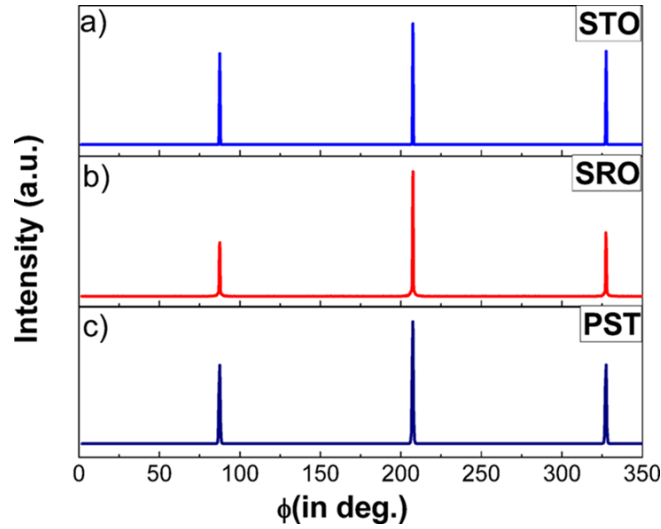


Fig. 4.1.17. A  $\phi$ -scan using the (200) reflections of PST and SRO thin films and of the STO substrate showing cube-cube growth, hence supporting cube on cube growth.

growth. The out-of-plane lattice parameter has been found to be 0.234 nm which is close to bulk value, showing that the films were relaxed. The FWHM values calculated from in-plane measurements are 0.69, 0.76 and 1.11 for STO, SRO and PST respectively, indicating a good crystallinity of epitaxial growth. The epitaxial relationship between substrate, electrode and PST film can be given as: (111) PST// (111) SRO// (111) STO.

The microstructure was studied through TEM investigations. The thickness of the films was determined from cross-sectional TEM. The thickness of SRO and PST has been found to be 90 nm and 85 nm respectively. A cross-sectional TEM dark field image with SAED patterns is shown in Fig. 4.1.18 (a-b). The SAED patterns revealed that the PST films were indeed epitaxial, supporting our XRD investigations. As shown clearly in the dark field image, the interface between STO and SRO is sharp and without misfit dislocations. In the case of PST, the interface was found to have misfit dislocations in order to relax the misfit strain. In

comparison to PST (100), PST (111) has a higher density of misfit dislocations. In the SAED patterns, similar kinds of superstructure reflections were observed as in the case of PST (100), thereby supporting the XRD results. The size of the ordering domains was determined from the dark field images acquired using  $(\frac{1}{2} \frac{1}{2} \frac{1}{2})$  reflections. A majority of ordering domains were found to be smaller than 4 nm in size.

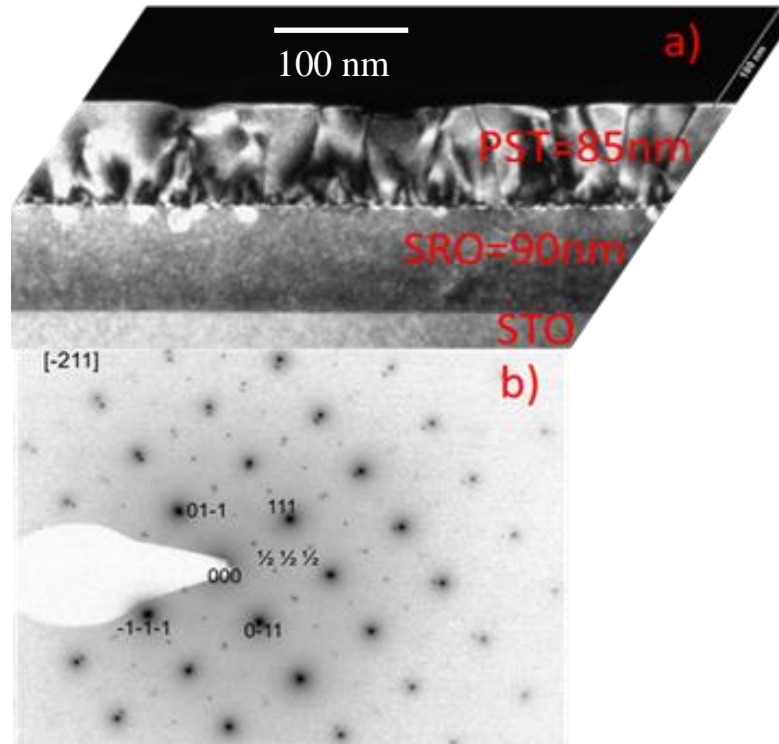


Fig. 4.1.18. (a) A cross-section dark-field image recorded along  $[-211]$  pole (b) SAED pattern of cross-section image showing superstructure reflections.

#### 4.1.7. Electrical characterization of PST (111) thin films

The ferroelectric properties of PST (111) thin films have been analyzed through hysteresis loop measurements at RT as well as low temperature. The P-V loops were recorded at RT and 100 K temperatures are shown in Fig. 4.16. As expected at low temperature PST behaves like a regular ferroelectric. The remnant polarization  $P_r$  and the coercive voltage  $V_c$  of the PST film under the application of 2.5 V were found to be  $3.58 \mu\text{C}/\text{cm}^2$  and 0.38 V, respectively. At RT, the remnant polarization  $P_r$  and coercive voltage  $V_c$  of the PST film under the application of 2 V were found to be  $2.27 \mu\text{C}/\text{cm}^2$  and 0.27 V, respectively, which is lower than the values observed for PST(100) films despite the favorable orientations along the polarization direction.

The most probable reason for the low values is the micro structure quality and cation-ordering. As discussed PST (111) thin films have a larger density of misfit defects, which could lead to deterioration of the ferroelectric properties. Another possible reason might be the size and amount of cation ordered regions which is less in this case compared to PST(100) films. As in the case of PST (100), the pyrochlore phase yields no ferroelectric properties. Moreover, the dielectric constant for these films at RT was found to be  $\sim 460$  which is almost equal to the PST (100) films. Similar to PST (100), at RT PST (111) films might also be in the  $T_B$  temperature range having

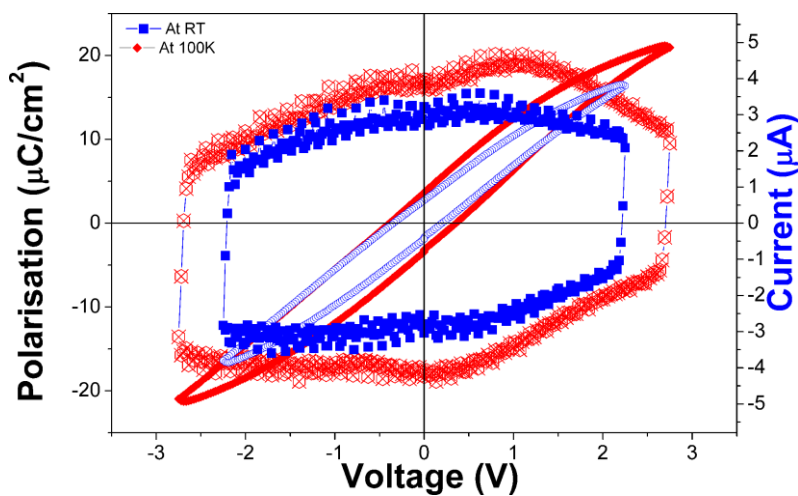


Fig. 4.1.19. Macroscopic polarization-voltage and switching current-voltage hysteresis curves of a PST film at RT (blue) and 100 K (red)

ergodic phase consisting of randomly distributed and oriented PNR. Thus, on application of electric field, ferroelectric properties were displayed by the films.

The local ferroelectric switching of the films was investigated by PFM. A modulation voltage of  $0.5 V_{\text{rms}}$  at 25 kHz was used and the tip loading force kept constant at 10 nN. At the deposited state, the thin films showed no response to the application of an ac electrical field. Following this, a  $3 \times 3 \mu\text{m}^2$  area was poled downwards by applying a voltage of +4 V for background poling. Then, at the center, a smaller area of  $1 \times 1 \mu\text{m}^2$  was switched upwards by a voltage of -4 V. This reveals clearly that films can be locally switched by applying an external voltage. The local ferroelectric response is shown Fig. 4.1.20.

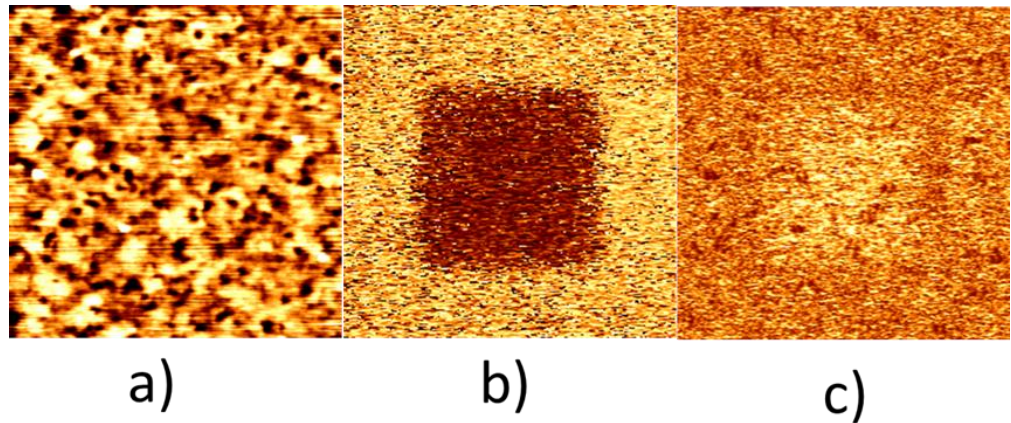


Fig. 4.1.20. PFM piezoresponse image ( $3 \times 3 \mu\text{m}^2$ ) of a PST(111) film (a) Topography of PST film; (b-c) A phase and amplitude image after switching a  $1 \times 1 \mu\text{m}^2$  area in the middle.

#### 4.1.8. Summary

Epitaxial (100)- and (111)-oriented PST thin films were grown using self-made PST targets. The produced films were epitaxial and were found to have cation-ordering which was confirmed through superstructure reflections obtained using XRD and TEM SAED patterns. These films show ferroelectric properties at RT as well as at low temperature. The microstructure and electrical quality of PST (100) films are better than compared to PST (111) films, however, the dielectric constant for both the films were less compared to the PST bulk and sol-gel reported values. Using PFM we have shown that films which initially show no piezoelectric response could be locally switched by applying an external field. The produced films show the cation ordered regions whose size was varied from 5 nm to 10 nm by increasing thickness, indicating that the size of the cation-ordering might depend on the thickness of the films. In the following chapter, we study the influence of reduction in the thickness of films on cation-ordering and ferroelectric properties.

## Chapter 4.2 Impact of strain on PST films

Recently there is extensive interest in the influence of strain on ferroelectric properties of functional oxides. Strain can be introduced into the films by different means such as: deposition far from thermodynamic equilibrium including quenching the films immediately after deposition, by using different substrates or electrodes with different lattice parameters, or simply by changing the thickness of the films. In the case of PST films, as discussed in the previous chapter, there is an important influence of the strain on the size of cation-ordered regions, and subsequently on the ferroelectric properties. Thus, the present chapter will address the influence of strain introduced in the PST films by using the lattice mismatch approach. The first section of the chapter deals with the deposition process and its details. In the next section the microstructure of thin PST films is discussed with the results obtained through XRD and TEM investigations. It was found that with scaling down the thickness of PST, the films became totally disordered, but were showing better ferroelectric properties. In the next section a detailed study of ferroelectric properties is included. An unusual behavior in the piezoelectric coefficient of the PST (100) thin films will be addressed.

### 4.2.1. Deposition of PST on LSMO-electroded STO substrates

STO substrates were etched and annealed in a similar way as discussed in Chapter 4.1.1. Further, in order to enable the electrical and piezoelectric measurements, PST films were grown on LSMO. The lattice mismatch between PST and LSMO is 6.31% at RT, which is high enough to introduce large strain into the PST thin films. In order to achieve good microstructure and ferroelectric properties of PST films, it is very important to grow smooth LSMO on STO substrates. The lattice mismatch between STO and LSMO is only 0.6% at room temperature which enables coherent growth of LSMO on STO substrates. It was found that the films, roughness was high when a 5 Hz laser frequency was used. Thus for having smooth growth of PST on LSMO, the laser frequency was optimized to 3 Hz.

### 4.2.2. Structural investigations

XRD  $\theta$ - $2\theta$  scans show (Fig. 4.2.1) only the  $(00l)$  reflections for both *LSMO* and *PST* films, revealing that the films were fully *c*-axis oriented.

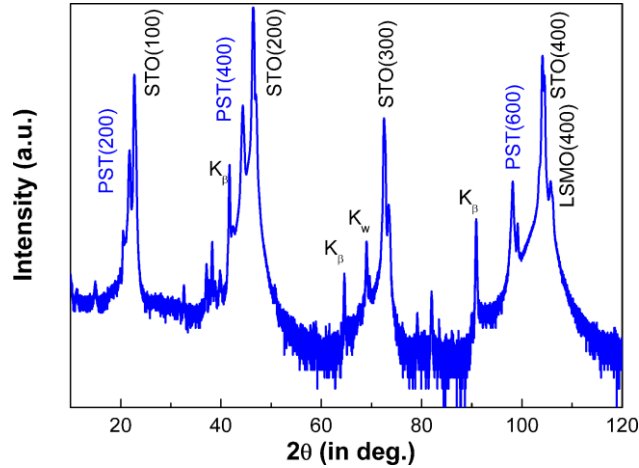


Fig. 4.2.1. Out-of-plane XRD patterns of a *PST* film deposited on *LSMO/STO* (001).

The *LSMO* and *STO* peaks overlap especially for low angle reflections, because of their very similar lattice parameters. The out-of-plane lattice parameter of *PST* films has been calculated using the XRD diffraction pattern, and it was found to be  $4.08 \text{ \AA}$  which is slightly higher than the bulk lattice parameter. In order to claim complete epitaxial growth of *PST* films, in-plane XRD measurements were performed. For this type of measurements, *STO*, *LSMO* was fixed at their respective  $2\theta$  angle for the (222) reflections. For *PST* (444) reflections were used. The in-plane measurements for *STO*, *LSMO* and *PST* contain four peaks for each material at the same azimuthal angle ( $\varphi$ ), as shown in Fig. 4.2.2. This reveals that all the films were deposited epitaxially cube on cube. The in-plane and out-of-plane epitaxial relationships between substrate (*STO*), electrode (*LSMO*) and thin film (*PST*) have been found to be (001) *PST*// (001) *LSMO*// (001) *STO* and (100) *PST*// (100) *LSMO*// (100) *STO*, respectively (cubic indexing is used for *LSMO* and *PST*). The full width at half maximum values (FWHM) of the (222) reflections for *STO*, *LSMO*, and *PST* were found to be  $\sim 0.29^\circ$ ,  $0.30^\circ$ , and  $0.60^\circ$ , respectively. The FWHM values for the *LSMO* as well as for *PST* are quite close to substrate values, confirming a good epitaxial growth. Epitaxy of the *PST* films was globally analysed by pole figure measurements (Fig. 4.2.3) performed by using (220) reflections. The pole figure shows that only four reflections at  $\psi=45^\circ$  and  $\varphi=0^\circ, 90^\circ, 180^\circ$  and  $270^\circ$  were observed which confirm the good in-plane orientation, almost single-crystal-like, of the prepared *PST* films. The extra four reflections with less intensity at the edge of the outer circle of the pole figure image signify the another set of (220) reflections present at  $\psi=90^\circ$ . In principle, these are valid sets of reflections. No cation-ordering was observed in



these films through XRD. This is a first indication that the reduction in the thickness has a strong influence on the degree of cation-ordering.

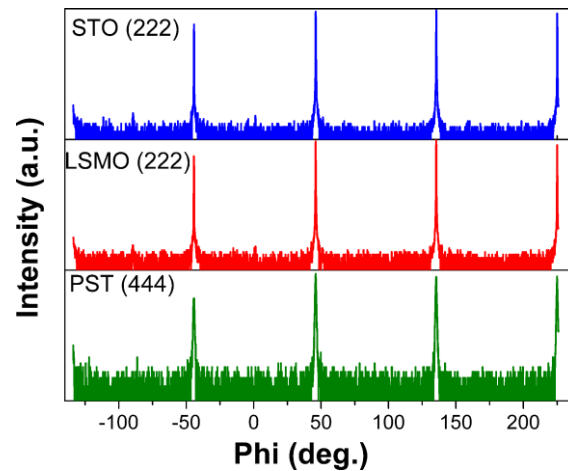


Fig. 4.2.2. A  $\phi$ -scan using the (222) and (444) reflections of STO, LSMO and PST thin films, respectively. For these scans the sample was tilted by an angle ( $\psi$ ) of  $54.7^\circ$ .

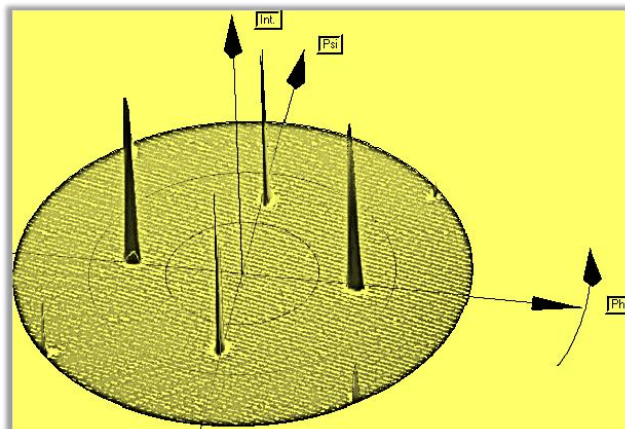


Fig. 4.2.3. (a) A Pole figure image showing only (220) intensity peaks observed at  $\psi=45^\circ$  and  $\psi=90^\circ$  for PST films. For pole figure measurements the  $2\theta$  angle was fixed for (220) reflections and the angles  $\psi$  (0-90) and  $\phi$  (0-360) were varied.

In order to analyze the status of strain present in the PST thin films, reciprocal space mapping (RSM) measurements were performed. Through reciprocal lattice mapping both in-plane and out of plane lattice parameters were measured. In order to determine the lattice parameters by RSM, a certain reflection which should not be perpendicular to any of the unit cell axes should be chosen. Otherwise, the lattice constant of this axis cannot be determined. In this study RSM investigations using the diffraction peaks of the (103) plane were performed. As discussed in Chapter 3,



in the RSM measurements normal  $2\theta/\omega$  scans are performed at different  $\omega$  values with an offset.

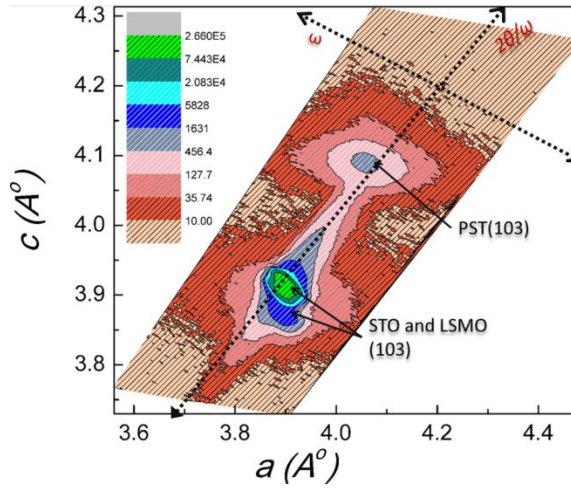


Fig. 4.2.4. The reciprocal space map of the (103) reflections from PST/LSMO/STO (001) epitaxial films. The scan directions  $2\theta/\omega$  and  $\omega$  of the two axes are also illustrated.

Following the analysis of RSM discussed in Chapter 3, for LSMO in-plane and out-of-plane lattice parameter of 3.88 Å and 3.87 Å, respectively were determined from Fig. 4.2.4. The in-plane and out-of-plane lattice parameter of PST were 4.05 Å and 4.09 Å, respectively. The difference between in-plane and out of plane lattice parameter values for PST films confirms that the films are compressively stressed on LSMO.

The surface morphology of the PST and LSMO thin films was checked by AFM measurements. The measurements show a smooth surface for LSMO as well as for the PST films [Fig. 4.6 (a-b)]. A step-flow growth was observed for the LSMO films. The PST films have the root mean square value of roughness about 0.6 nm over an area of  $4 \times 4 \mu\text{m}^2$  signifying a flat and smooth surface of PST on LSMO and STO.

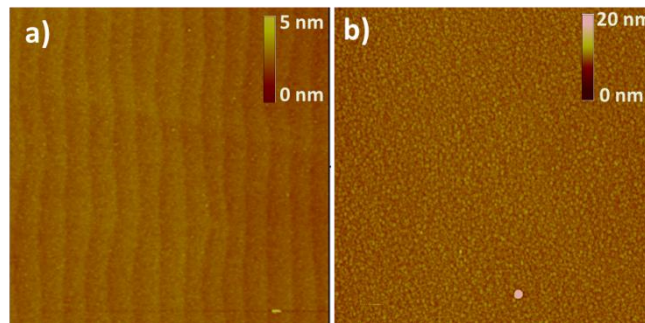


Fig. 4.2.5. A AFM image showing the topography of PST films. (a) A  $5 \times 5 \mu\text{m}^2$  image of LSMO film showing a step flow growth. (b) A  $4 \times 4 \mu\text{m}^2$  optimized growth of PST.

### 4.2.3 TEM investigations

The internal microstructure of the PST thin films was studied with TEM. A cross-section TEM image shown in Fig. 4.2.6. revealed that the thickness of PST and LSMO was 30 nm and 65 nm, respectively. It is very clear from the cross-sectional image that LSMO has coherently grown on STO substrates. Due to the large lattice mismatch between LSMO and PST of 4.91%, misfit dislocations (MDs) were formed at the PST-LSMO interface as shown in Fig. 4.2.6. The critical thickness for the PST films were calculated and found to be around 4 nm by using Matthews and Blakeslee

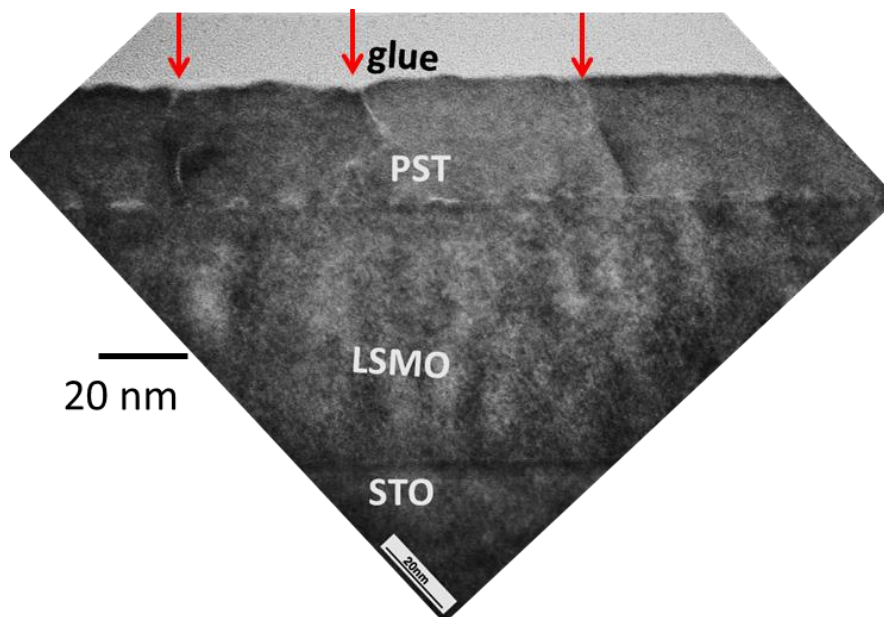


Fig. 4.2.6. A TEM cross-section image of the LSMO-PST interface acquired along the [110] direction, showing the threading dislocations (red arrows).

calculations [4.2.1]. The PST film thickness is larger than the calculated critical thickness values, thus a high density of MDs is expected. The average spacing between the MDs has been found to be around 10 nm which relatively well fits the theoretical values [4.2.2]. The defects indicated with the red colour arrows are threading defects while the other symbols in black colour indicate the misfit dislocations in HRTEM image. Threading dislocations were observed to emerge from many of the misfit dislocations and propagate to the surface of the film. As clear from the cross-sectional image, PST has a columnar growth which can be attributed to a very large lattice mismatch between PST and the underlying LSMO layer. The selected area diffraction (SAED) (only indexed for PST) for the sample in [110] direction reveal that the films are epitaxial (Fig. 4.2.7), which supports the XRD measurements on epitaxial growth. The additional set of reflections observed are similar to the superstructure reflections existing in the PST films. As discussed in XRD results, there was no superstructure reflections observed in the XRD patterns. To reveal the origin of the additional set of reflections in SAED, a cross-sectional

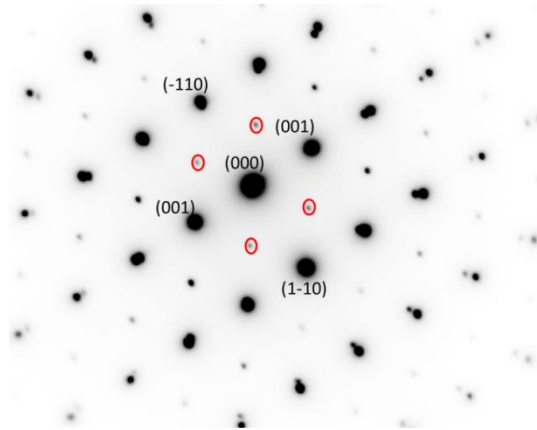


Fig. 4.2.7. TEM- SAED patterns for cross-section sample along  $[110]$  indexed for PST. The red colour circles are highlighting the set of additional reflections obtained.

dark field TEM image (Fig. 4.2.8.) was taken by using one of the additional obtained reflections. Only the LSMO layer was showing the contrast signifying the LSMO as the origin of these reflections. Thus in support to our XRD results, TEM confirms that there were no superstructure reflections in the PST material at RT.

In order to find the existence of cation-ordering at low temperature, TEM investigations were performed at low temperature (98 K). No superstructure reflections were observed at low temperature even. Similar to RT, an additional set

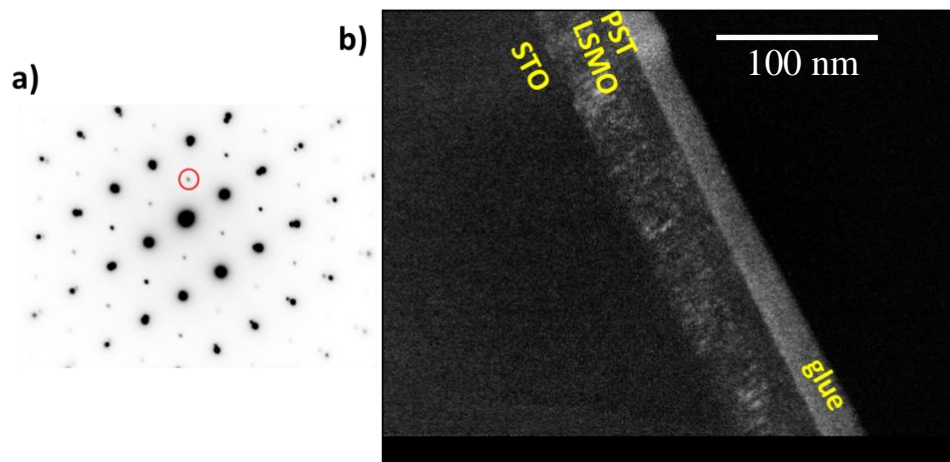


Fig. 4.2.8. (a) SAED patterns of PST/LSMO/STO heterostructure showing additional reflections in red colour circles at RT. (b) A Cross-section dark field image captured using the encircled red colour reflection revealing that the additional reflections belong to the LSMO layer.

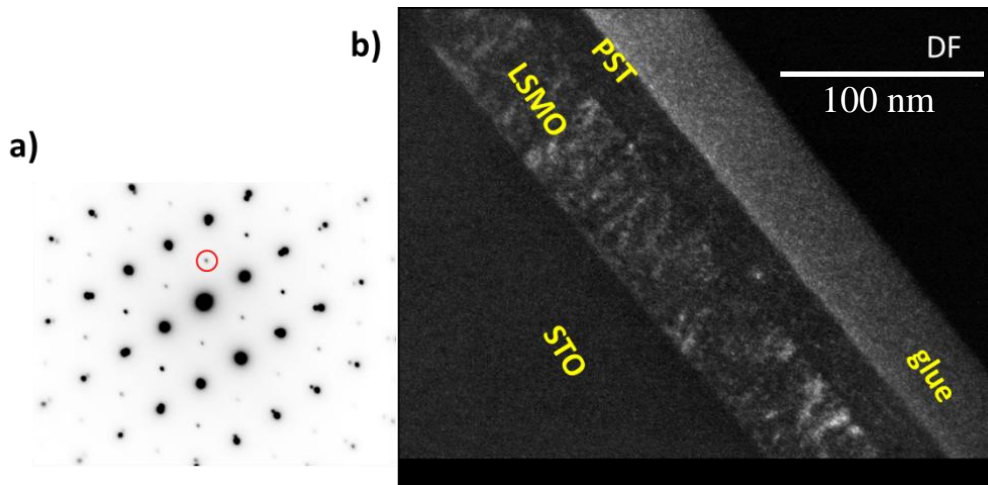


Fig. 4.2.9. (a) SAED pattern of the PST/LSMO/STO heterostructure showing additional reflections, one of which is shown in red colour circles at 98 K. (b) A Cross-section dark field image captured using the encircled red colour reflection revealing that the additional reflections belong to the LSMO layer.

of reflections was observed. Further, it was confirmed to be a part of LSMO layer rather than of PST layer as shown in Fig. 4.2.9. Thus with the reduction of thickness, no cation-ordering was observed at RT as well as low temperatures.

The in-plane and out-of-plane lattice parameters were calculated through SAED patterns with respect to the STO substrate as shown in Fig. 4.2.10.

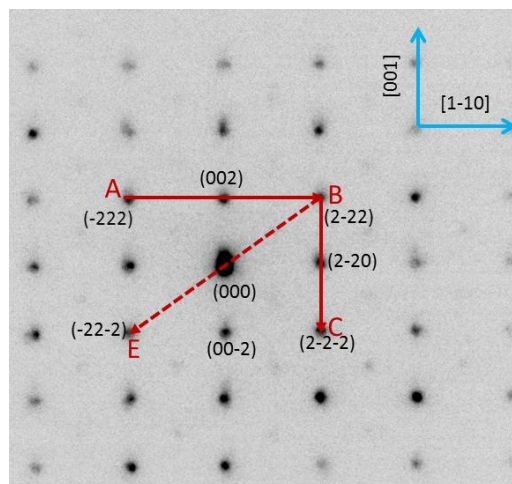


Fig. 4.2.10. (a) SAED pattern of PST in (110) direction confirming the tetragonality of the heterostructure.

For a cubic PST system, the ratio between AB/BC and the angle between AB and BE vectors should be 1.41 and  $35.26^\circ$ , respectively [4.2.3]. The observed values of the

ratio between AB/BC and the angle between AB and BE vectors for the investigated PST films were 1.43 and  $33.90^\circ$  which indicate that the film has a tetragonal distortion. This indicates that there is large misfit strain in the PST films. Since STO and LSMO both have smaller lattice parameters than PST, the PST films are strained in-plane and compressed in out-of-plane direction.

#### 4.2.4 Electrical characterization of PST Films

Macroscopic ferroelectric properties of PST (100) thin films deposited on buffered LSMO-electroded STO substrates were investigated at RT.  $P$ - $V$  and  $I$ - $V$  hysteresis loops were recorded using a triangular waveform of 1 kHz frequency as shown in Fig. 4.2.11. The films show ferroelectric properties with remnant polarization  $P_r$  and

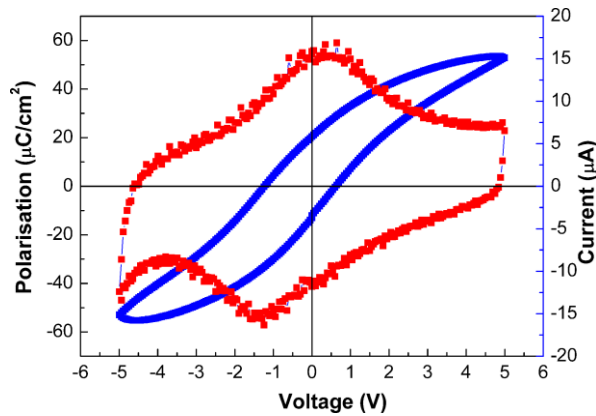


Fig. 4.2.11 Macroscopic polarization-voltage and switching current-voltage hysteresis curves of a PST/LSMO/STO heterostructure at RT.

coercive voltage  $V_c$  of  $17 \mu\text{C}/\text{cm}^2$  and 1.3 V, respectively. These values are higher than those of the cation-ordered thick films discussed in Chapter 4.1. The most probable reason for this enhancement in the ferroelectric properties is the tetragonal distortion in the PST films. Similar kind of stress effects are observed in other ferroelectric thin films [4.2.4-4.2.5]. The ferroelectric hysteresis loops measured in the temperature range from 10 K to 350 K [Fig. 4.2.12-4.2.13] reveal normal ferroelectric behavior at low temperatures. At 100 K, the remnant polarization  $P_r$  and coercive voltage are the same as for RT, although the hysteresis loops were more saturated and the spontaneous polarization was around  $40 \mu\text{C}/\text{cm}^2$ . This value is around 10 times higher in comparison to the 60 nm thin PST (100) films which were discussed in Chapter 4.1.1. PST films of 77 nm thickness with high cation-ordering discussed in Chapter 4.1.1 have the same spontaneous polarization as it was found in these highly stressed films. As the temperature increases, the hysteresis loops become slim, although some hysteresis loops look broader than the low-temperature curves.



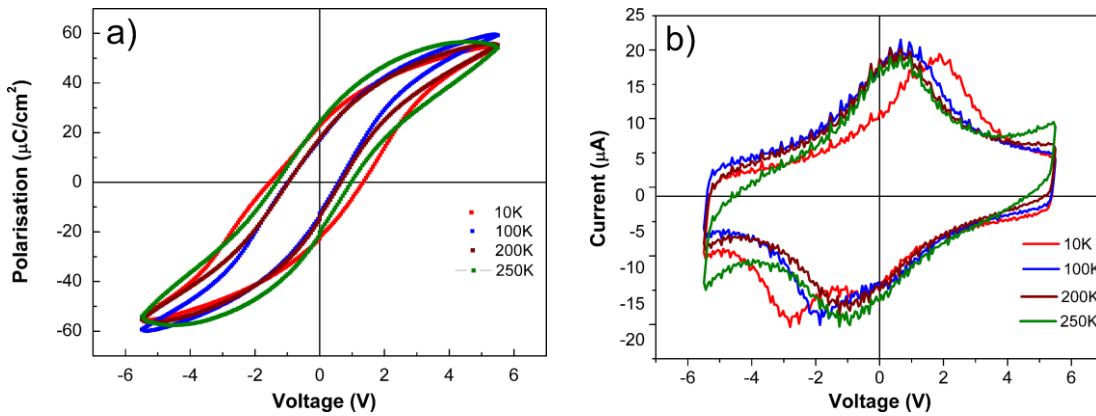


Fig. 4.2.12. (a) Macroscopic polarization-voltage and (b) switching current-voltage hysteresis measurement curves recorded at 1 kHz for low temperatures.

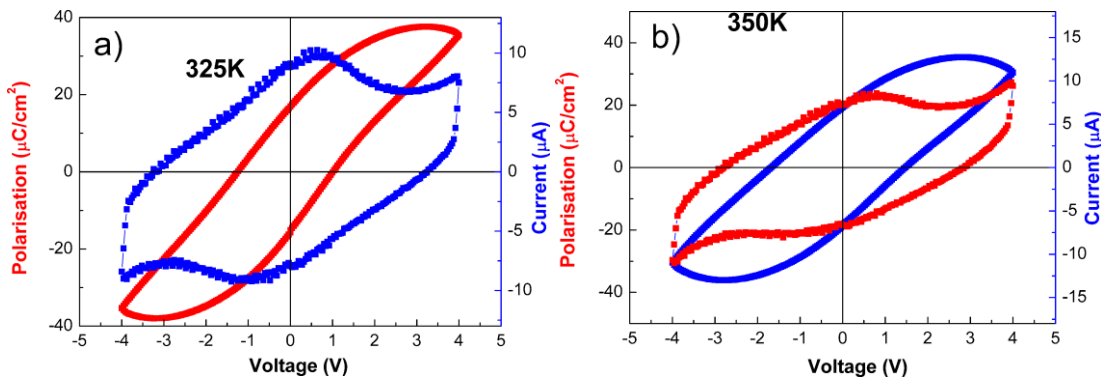


Fig. 4.2.13. Macroscopic polarization-voltage and switching current-voltage hysteresis curves of a PST/LSMO/STO heterostructure at (a) 325 K and (b) 350 K.

Contributions from leakage current are clear from the I-V curves. No significant change either in coercive field or in remnant polarization was observed above 100 K. There was a slight increase in leakage current at temperatures higher than RT, but nevertheless with good ferroelectric properties.

The C-V curves recorded at different temperatures with 100 kHz frequency are shown in Fig. 4.2.14. The C-V characteristics show butterfly shape, which are the finger-print characteristics of the ferroelectric switching. The results obtained from these curves at low as well as high temperatures are in accordance with the hysteresis loops measurements. At RT for a frequency of 100 kHz, the zero field values of the dielectric constant and loss tangent were around 350 and 0.15, respectively. As it is very clear from the ferroelectric measurements, the reduction in thickness of the PST films have helped in improving the ferroelectric properties compared to the influence of cation-ordering.

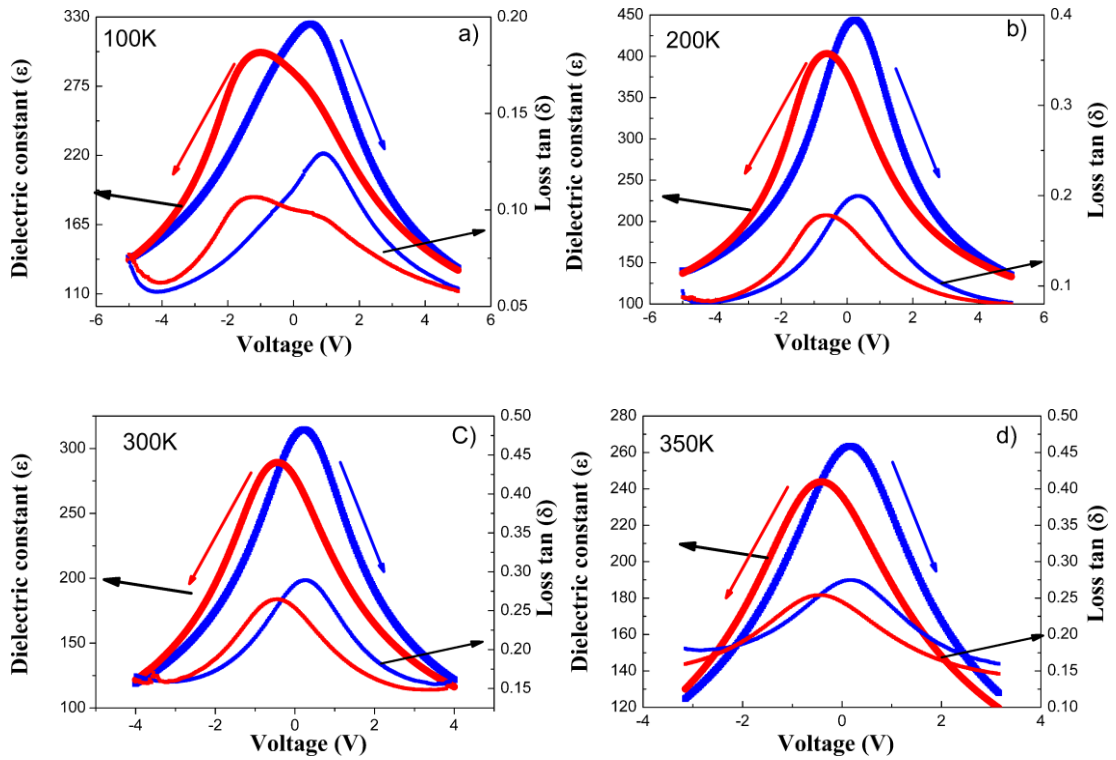


Fig. 4.2.14. Voltage dependent dielectric constant at different temperatures of a PST/LSMO/STO (100) heterostructure from C-V measurements assuming the plan-parallel capacitor model.

The local ferroelectric switching of the films was also investigated by PFM, as shown in the Fig. 4.2.15 (a-b). When the films were scanned with an  $V_{ac}$  of 0.7 V

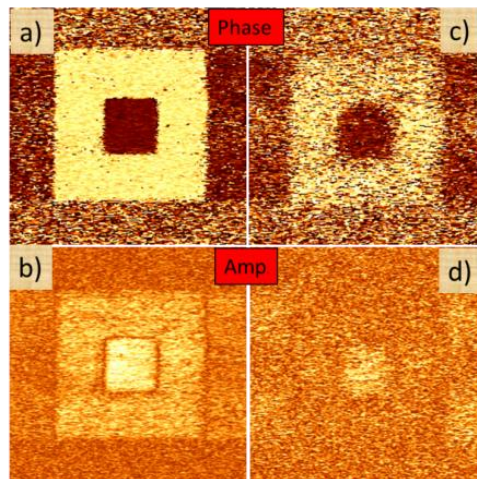


Fig. 4.2.15. PFM piezoresponse images ( $5 \times 5 \mu\text{m}^2$ ) of a strained PST film. (a-b) Phase and amplitude image after switching a  $1 \times 1 \mu\text{m}^2$  area in the middle. (c-d) Phase and amplitude after 1 hour revealing good retention characteristics. A modulation voltage of 0.7  $V_{rms}$  at 26 kHz was used and the tip loading force kept constant at 20 nN for scanning this image.

in the grown state, there was no signal observed. In a second step, a  $3 \times 3 \mu\text{m}^2$  area was poled downwards by applying a voltage of +5 V for background poling. The background poling aligns the random ferroelectric domains in a direction opposite to the applied field. In the case of relaxors, randomly oriented polar regions get aligned in an opposite direction to the applied  $dc$  field. Then, at the center, a smaller area of  $1 \times 1 \mu\text{m}^2$  was switched upwards by a voltage of -5 V. By scanning a larger area, the region poled with -5 V shows a different contrast revealing that the films can be locally switched by applying an external voltage. An image of phase and amplitude is shown in Fig. 4.2.15. Moreover, the contrast remained unchanged for more than one hour.

#### 4.2.5. Non-linear dielectric and piezoelectric behaviour of PST films.

The piezoelectric coefficient is usually determined by measuring the PFM signal amplitude at different excitation voltages. The amplitude of the PFM signal is given by:

$$S_{PFM} = kd_{zz} \cdot V_{ac} \quad 4.2.1$$

where  $k$  is a sensitivity constant of the AFM microscope obtained by measuring standard samples such as quartz,  $d_{zz}$  is the piezoelectric coefficient along the crystallographic direction of the investigated crystal and  $V_{ac}$  is the amplitude of the excitation signal. As it can be seen the relation is linear. This is valid for all the

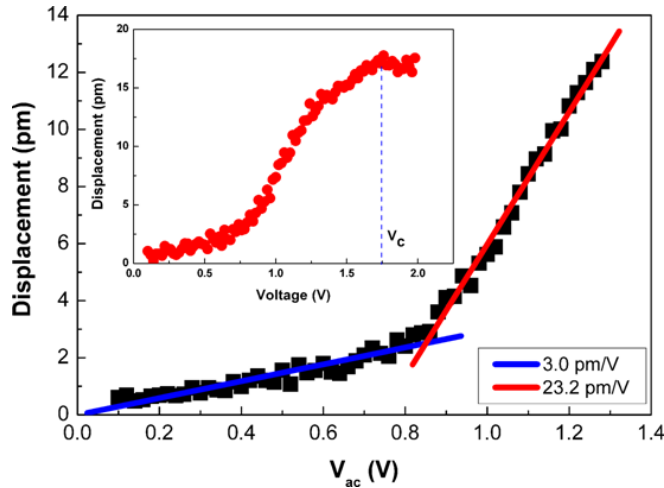


Fig. 4.2.16. Piezoresponse of the PST film as a function of the ac excitation voltage. The inset shows the PFM signal at higher voltage with a strong non-linear behavior at coercive voltage ( $V_c$ ).

ferroelectric materials for  $V_{ac}$  lower than the corresponding coercive voltage. At  $V_{ac}$  larger than coercive voltage the PFM signals drop significantly. The  $d_{zz}$  value is



given by the slope of the plot of  $S_{PFM}$  vs.  $V_{ac}$  in the  $V_{ac}$  range up to the coercive voltage. However, in the present case instead of one single slope, two slopes were observed for the PST films as shown in Fig. 4.2.16. The piezoelectric coefficient in the low voltage range ( $<0.8V$ ) is 3 pm/V. On applying a higher ac voltage, a sudden increase in the piezoelectric coefficient to 23.3 pm/V is observed. This significant increase in the effective piezoelectric coefficient of about one order of magnitude is observed at values well below the coercive voltage ( $V_c$ ). In this case  $V_c$  is 1.7 V as shown in inset of Fig. 4.2.16. The above effect is also shown in imaging using PFM. There is a strong and irreversible influence of the  $V_{ac}$  on the PFM signal. With the increase in amplitude of the ac voltage, the PFM signal becomes stronger. At  $V_{ac}=0.25$  V, there is only a noisy phase with low amplitude. However, at 0.50 V, a preferred direction of the phase signal was observed. As the voltages approach the coercive voltage, a strong signal of upward polarization (dark contrast / negative phase signal) was observed. It was observed that after applying a high ac field, the piezo response never came to its original value after removal of the external field, but

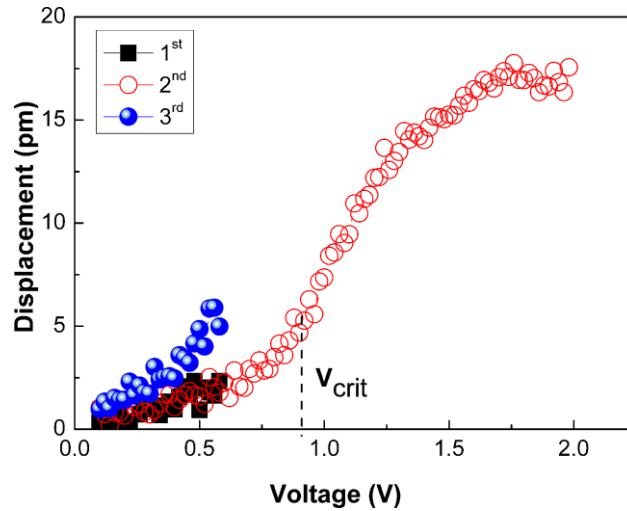


Fig. 4.2.17. Piezoresponse of the PST film as a function of the applied ac voltage showing increase in piezoelectric coefficient for the other cycle than before.

remains always higher than the previous value. Fig. 4.2.17 shows a piezoresponse curve recorded for three cycles. During the first cycle the voltage was swept from 0 V to low values under the critical field; the second scan was swept to the coercive voltage and a final scan in the low level range showed that the piezoelectric coefficient remains irreversible at high level. This behavior is rather unusual for a ferroelectric material. The piezoelectric coefficient for a (001) ferroelectric material with tetragonal symmetry can be given as [4.2.6]:

$$d_{33} = 2\varepsilon_{33}Q_{33}P_{33}^s \quad 4.2.2$$

where  $d_{33}$ ,  $\epsilon_{33}$ ,  $Q_{33}$  and  $P^s_{33}$  are longitudinal piezoelectric-coefficient, dielectric permittivity, electrostriction coefficient and spontaneous polarization, respectively. Thus the PFM amplitude can be influenced by three factors; dielectric constant, polarization, and/or electrostriction coefficient.

Since the electrostrictive coefficient is not expected to vary significantly and the voltages are well below the coercive voltage, so no significant polarization switching is expected. Thus, the non-linear behavior is expected to occur due to the dielectric constant. Therefore, macroscopic measurements of the dielectric constant at variable applied ac voltage were performed. A similar behavior like the piezoelectric response was found: a sharp increase in dielectric constant was observed around 0.6 V for 1 kHz as shown in Fig. 4.2.18 (a). Likewise, the dielectric constant changes irreversibly to a value higher than the pristine value as shown in Fig. 4.2.18 (a). The dielectric constant for the pristine sample at 0.1 V is 407 and after applying  $V_{ac}$  it was increased to 410 with around 0.035 losses for both the cycles. The critical field is also close to the value determined by PFM, although displacement values after the critical field in piezoelectric measurements (Fig. 4.2.17) are three times higher than the values observed before the critical field. In case of dielectric values this difference is very small in comparison to piezoelectric measurements. This difference in the enhancement values can be explained on the basis of local and average response. In the case of piezoelectric measurements, the response is local and thus it might be from a region which responds faster to the applied field as compared to other regions in the sample. In case of dielectric constant measurements, the response is rather global, thus lower than the local

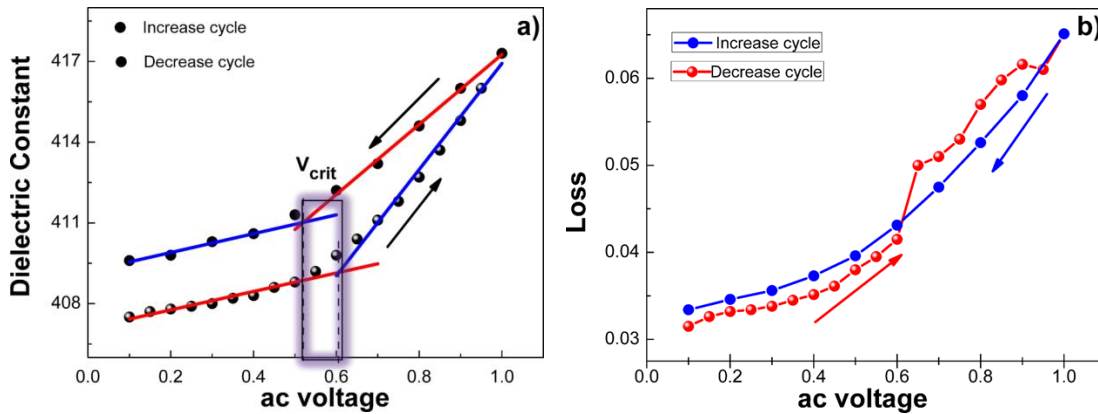


Fig. 4.2.18. (a) Dielectric constant variation of the PST film as a function of the applied ac voltage showing a sharp increase in dielectric constant at critical voltage  $V_{crit} = 0.5$  to  $0.6$  V and (b) Variation in dielectric loss with the applied voltage.

values. However, the slope of dielectric constant before and after the critical voltage are 3.4 and 20.12 which are quite similar to the values of the piezoelectric coefficient. Thus, it is highly probable that the non-linear piezoelectric behavior is due to this non-linear behavior of the dielectric constant.

The dielectric non-linearity is already reported in literature for few ferroelectric materials [4.2.7-4.2.8]. In this context, several phenomenological models have been proposed to explain the physical origin of the dielectric and piezoelectric anomalies [4.2.8]. Nevertheless, none of these models have gained universal acceptance yet, due to some contradictory experimental results [4.2.8]. The most probable mechanism for this dielectric non-linearity is explained on the basis of reversible and irreversible domain wall motion under applied external bias. This model is known under the generic name of Rayleigh model [4.2.9-4.2.10]. According to the Rayleigh model, the dielectric constant is a superposition of reversible and irreversible parts, the latter being field-dependent and can be given as:

$$\varepsilon = \varepsilon_{init} + \alpha_{\varepsilon} E$$

where  $\varepsilon_{init}$  is the reversible dielectric Rayleigh parameter and  $\alpha_{\varepsilon}$  is the irreversible parameter. Attempt to fit our data with this Rayleigh model failed. To check once more we have addressed the frequency dependence of the dielectric constant. According to the Rayleigh model, the non-linearity is reduced with increase in frequency [4.2.11-4.2.12]. In our case there was no reduction in non-linearity with the frequency.

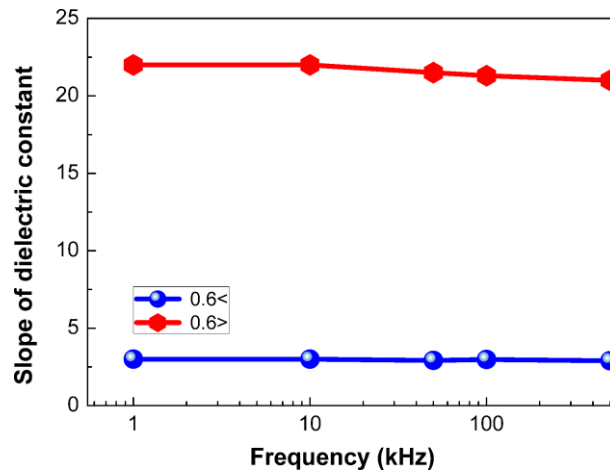


Figure 4.2.19 Variation of slope of dielectric constant with frequency. The blue color points show the slopes measured below  $V_{crit}$  and red color points are above it.

The magnitude of sharp increase was the same for all the frequencies as shown in Fig. 4.2.19. In literature it is reported that in the non-linear region of the dielectric constant the losses are highly dependent on frequency and there is a sharp increase in losses [4.2.12], but in the PST, no such kind of phenomenon was observed as shown in Fig. 4.2.19. The Rayleigh model explains the dielectric non-linearities on the basis of domain wall motion. In case of relaxors like PST, there are no ferroelectric

domains in the classical way. As it was discussed, there are only polar nano-domains. The possible mechanisms for this kind of non-linearity are thus:

- 1) Percolation of the polar regions in case of PST relaxors films. The concept of PNR is very well known. Under the influence of the ac-field, these PNR regions oscillate and interact with each other. During this process PNRs in the disordered matrix may percolate. As the ordered phase of the PNRs have higher dielectric and ferroelectric properties as compared to disordered regions, the dielectric properties are enhanced at high field. This effect is manifest only above a threshold voltage where in this case it might be 0.6 V for a 30 nm thick film which is equivalent to a 200 kV/cm of applied field. After the removal of the field, not all the PNRs come back to their original state, certain amount of PNR remaining percolated which results in an enhancement in the dielectric properties.
- 2) A field-driven phase transition from normal tetragonal phase to some other phase with high dielectric constant.

In order to check the second hypothesis *i.e.* if our PST films are near to a phase transition point, the temperature dependence of the dielectric constant was

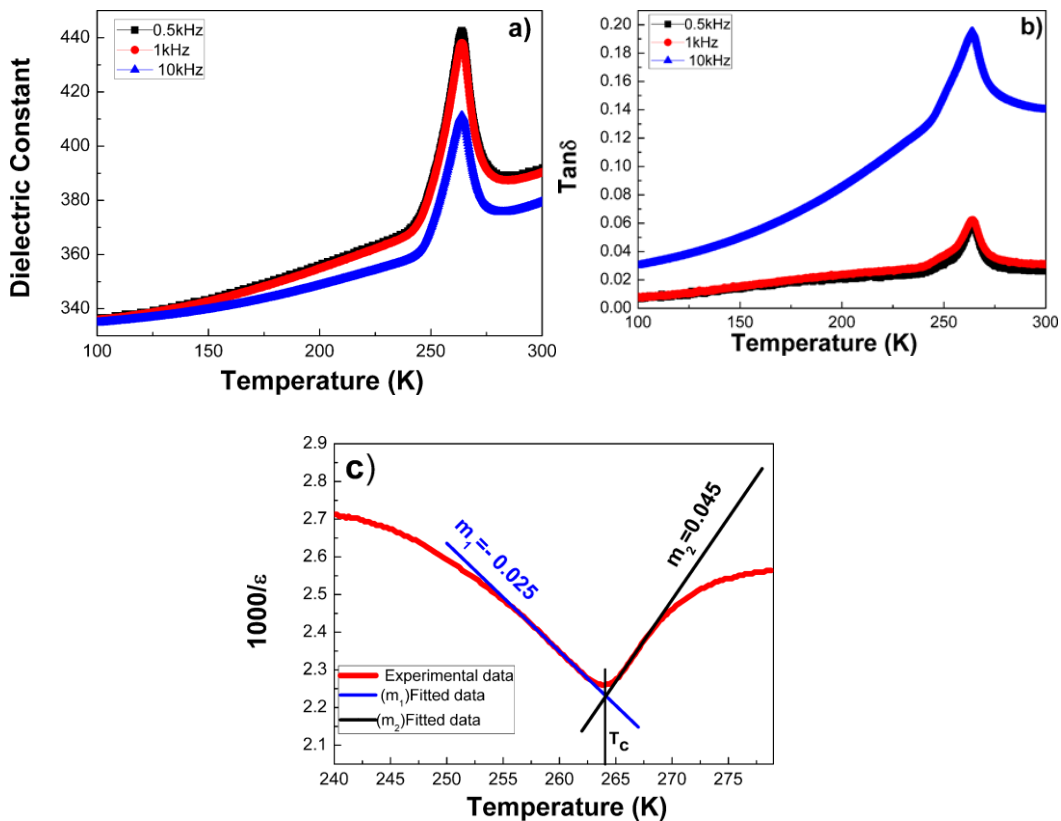


Fig. 4.2.20 (a) Temperature dependence of dielectric permittivity for three different frequencies. (b) Losses measured as a function of temperature for different frequencies. (c) Shows the reciprocal of the dielectric permittivity experimental data fitted to the Curie-Weiss law.

measured. The measurements were performed by using a small ac voltage of 0.1 V to avoid the influence of the applied voltage on the phase transition. A typical curve recorded for three different frequencies is shown in Fig. 4.2.20. In case of relaxors a diffuse and frequency dependent dielectric constant maximum is generally expected [4.2.13], but our data show very sharp dielectric maxima independent of frequencies. The dielectric maxima for all the frequencies are observed at around 265 K. The transition resembles a second order phase transition but with paraelectric phase at low temperatures and ferroelectric phase at RT.

In order to check whether the Curie-Weiss law is valid at  $T < T_c$ , we plotted the reciprocal values of the dielectric constant ( $\epsilon$ ) vs. temperature as shown in Fig. 4.2.20 (c). The slopes of  $\epsilon$  before  $T_c$  are about two times larger than the slope after  $T_c$ . This is also a finger-print characteristic of a second order phase transition [4.2.14]. As there is no phase transition reported in literature in this temperature range, so it was assumed that this second order phase transition belongs to phase transition from the tetragonal ferroelectric phase to another ferroelectric phase which might be specific only for the stressed thin films.

#### 4.2.6 Summary

Epitaxial (100)-oriented PST thin films have been grown on LSMO/STO (100) substrates. In order to find the influence of strain on the cation-ordering and ferroelectric properties, the PST films were deliberately strained by reducing the thickness. Detailed XRD, TEM and low temperature TEM analyses show that strain plays an important role in cation-ordering in PST thin films. By scaling down the thickness, the PST films are fully strained on LSMO/STO (100) as shown by RSM and TEM measurements. The in-plane compressive strain of 1% destroys the cation-ordering at all the temperatures from 100 K to 300 K. Nevertheless, thin PST films exhibit better ferroelectric properties in a temperature range from 10 K to 350 K in comparison to the cation-ordered thick films discussed in the previous chapter. Using PFM we have shown that the films which initially show no piezoelectric response could be locally switched by applying an external field. The local switching response of the films was unchanged for more than one hour, suggesting that the films have decent retention characteristics. The piezoelectric response shows an unusual non-linear behavior. The piezoelectric coefficient was found to be 3 pm/V at low field and increases to 23.2 pm/V in the high field. The threshold was about 0.8 V which is equivalent to a 200 kV/cm field. Similar effect was observed in dielectric permittivity under the application of a variable ac voltage. The most probable mechanism of this effect is percolation of nano-polar regions in PST. Phase transition measurements show a second-order ferroelectric to ferroelectric phase transition at 265 K.

PST is a promising material for pyroelectric sensors because of its high figure of merit. Thus, integration of PST on silicon substrates is desirable. In the next

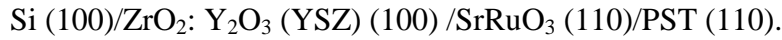
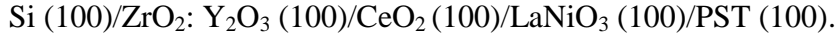
Chapter, the possibility of epitaxial growth on silicon substrates using appropriate buffer layers, but also on the control of the crystallographic orientation is discussed.

## **Chapter 4.3 Integration with Si**

The growth of oxide thin films on oxide single-crystal substrates is not suitable for Si-based applications. However, for the industrial applications oxide films have to be grown on Si substrates. Direct growth of functional oxides on Si is usually accompanied by interdiffusion or chemical reactions that degrade both Si and functional oxides. The epitaxial integration of functional oxides on Si substrates has been proven to be possible using buffer layers between Si and the functional oxides. During the selection of buffer layers, important issues like lattice mismatch, thermal expansion coefficient, chemical reactions, interdiffusion, crystal structure, etc. need to be taken into consideration. For instance, cubic yttria-stabilized (10 mol%) zirconia (YSZ) and  $\text{CeO}_2$  were two buffer layers extensively used for deposition of superconductive thin films on Si. Zirconium (Zr) is one of the few metals with a higher affinity to  $\text{O}_2$  than Si, or equivalently the reaction enthalpy of Zn with  $\text{O}_2$  is lower than that of Si to  $\text{O}_2$ . This makes YSZ inert to Si and prevents oxidation of Si during the deposition in the  $\text{O}_2$  atmosphere. During the last decade, YSZ was used intensively to stop inter-diffusion between the Si substrate and the top layers deposited on it. The second buffer layer ( $\text{CeO}_2$ ) was employed to change the epitaxial relationship and orientation of the following electrode layer, thereby altering the orientation of the top layer as in our case. This chapter deals with the details of deposition process and structural and electrical investigations of the PST films on Si. PST (100) and PST (110) epitaxial thin films were grown on buffered Si substrates: microstructure and epitaxial relationships were investigated through XRD and TEM. Both the sets of films were cation-ordered, as confirmed by XRD measurements. The influence of the film microstructure on the electrical properties was investigated through electrical measurements. Unusual behavior was observed in the piezoelectric coefficient of the PST (100) thin films as will be presented here. At the end of the Chapter the temperature dependence of the dielectric permittivity is discussed.

### 4.3.1. Deposition of PST films on buffered Si substrates

In order to achieve high quality epitaxial growth of PST films, the following two heterostructures were grown on Si substrates:



In the first heterostructure (H1)  $\text{LaNiO}_3$  (LNO) was used as the bottom electrode while in the other (H2), SRO was used. All the films were deposited *in-situ* by ablating stoichiometric targets of YSZ,  $\text{CeO}_2$ , LNO and PST with a 5 Hz repetition rate. The Si (100) substrates were cleaned with acetone and ethanol before mounting onto the substrate heater and loading them in the PLD chamber. The base pressure in the chamber was  $5 \times 10^{-7}$  mbar before raising the substrate temperature. An epitaxial YSZ thin layer was deposited on a natively oxidized Si wafer, with a laser fluence of  $2 \text{ J/cm}^2$  at  $750 \text{ }^\circ\text{C}$  temperature for three minutes (900 pulses) in the base pressure and then the  $\text{O}_2$  pressure was increased to  $6.5 \times 10^{-4}$  mbar. For the first heterostructure,  $\text{CeO}_2$  and LNO films were deposited at  $750 \text{ }^\circ\text{C}$  and  $650 \text{ }^\circ\text{C}$  in  $5.5 \times 10^{-4}$  mbar and  $0.4$  mbar  $\text{O}_2$  pressures, respectively with a laser fluence of  $2 \text{ Jcm}^{-2}$  each. For the second heterostructure SRO was deposited at  $700 \text{ }^\circ\text{C}$  in  $0.141$  mbar  $\text{O}_2$  with a fluence and repetition of  $2 \text{ Jcm}^{-2}$  and  $5 \text{ Hz}$  respectively. The epitaxial PST films were deposited at  $550 \text{ }^\circ\text{C}$  with a laser fluence of  $1.5 \text{ Jcm}^{-2}$  for both heterostructures. For electrical measurements, Pt top electrodes were deposited through a metal shadow mask (electrode size of ca.  $40 \times 40 \text{ } \mu\text{m}^2$ ) by RF-sputtering at RT.

### 4.3.2. Structural investigations

Both the heterostructures were structurally characterized by XRD. For the first heterostructure only (001) reflections were observed, revealing that the films are c-axis oriented as shown in Fig. 4.3.1 (a). On the other hand, for heterostructure (H2) only (001) reflections were observed for YSZ and (*hk*0) reflections for SRO and PST as shown in Fig. 4.3.1 (b).

In order to check the in-plane epitaxy for the heterostructure H1,  $\varphi$ -scans were performed using the (220) reflections of each material. For these scans the sample was tilted by  $\psi=45^\circ$  and the  $2\theta$  value fixed for the (220) reflection for all layers. In-plane measurements showed that all films have a four-fold rotational symmetry, which confirms the epitaxial growth of all the layers. Both YSZ and  $\text{CeO}_2$  films show the same rotational angle ( $\varphi$ ) as of Si for the (220) reflection, confirming cube-on-cube epitaxial growth. The (220) reflections of LNO (considered pseudocubic) and the PST are shifted by an azimuthal angle ( $\varphi$ ) of  $45^\circ$  with respect to the buffer layers and thereby to the substrate. This in-plane rotation of LNO on  $\text{CeO}_2$  is due to a better lattice match between  $\text{CeO}_2$  and LNO if the latter rotates by  $45^\circ$ .



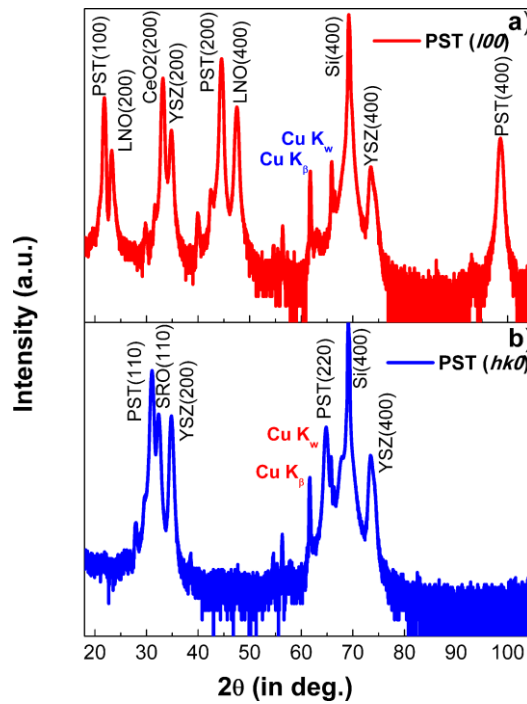


Fig. 4.3.1. XRD patterns obtained from the PST films deposited (a) LNO/CeO<sub>2</sub>/YSZ/Si (b) SRO/YSZ/Si.

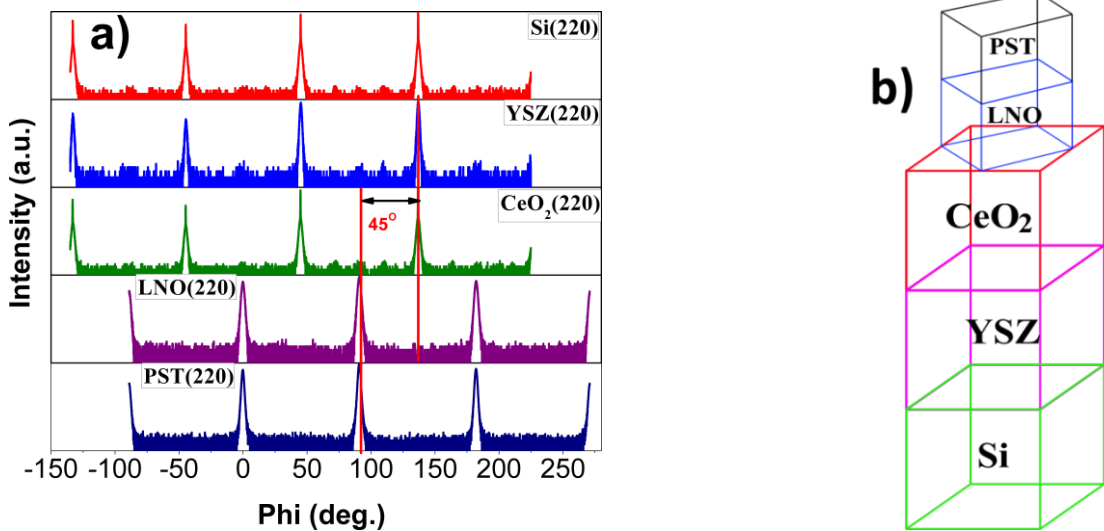


Fig. 4.3.2. (a)  $\phi$ -scan for PST on LNO/CeO<sub>2</sub>/YSZ/Si showing LNO and PST has 45° in-plane rotation with respect to CeO<sub>2</sub>/YSZ/Si. (b) A schematic showing the 45° rotation.

LNO has a (pseudocubic) bulk lattice parameter of 0.386 nm which allows an almost ideal crystallographic adjustment for LNO to grow diagonally on CeO<sub>2</sub>, with a unit-cell lattice parameter of 0.541 nm. This results in influencing the growth of the PST

film with the same 45° degree rotation with respect to the buffer layers and the Si substrate as shown in Fig. 4.3.2 (b) in the top and side views. The in-plane and out-of-plane epitaxial relationship between the films, buffer layers and substrate was found to be [011] PST // [011]<sub>pc</sub> LNO // [010] CeO<sub>2</sub> // [010] YSZ // [010] Si and (100) PST // (100)<sub>pc</sub> LNO // (100) CeO<sub>2</sub> // (100) YSZ // (100) Si (cubic indexing is used for all; pc - pseudocubic), respectively. The full width at half maximum (FWHM) values along (220) reflections for Si, YSZ, CeO<sub>2</sub>, LNO, and PST are ~0.17, 1.44, 0.18, 1.64, and 1.35, respectively, indicating good crystallinity and epitaxial growth of PST, LNO and buffers layers on Si substrate.

In order to analyse the epitaxial relationship between the PST film and the substrate, pole figure measurements were performed [Fig. 4.3.3 (a)] by using (220) reflections for the PST. For pole figure measurements, the 2θ angle was fixed for (220) reflections and the angles ψ (0-90) and φ (0-360) were varied. The pole figure shows that only four reflections at ψ=45° and φ= 0°, 90°, 180° and 270° were observed which confirms the good in-plane orientation, almost single-crystal-like, of the prepared PST films. The global degree of order is calculated by using the equation 4.1.1 from the XRD data. An order parameter of 0.42 was estimated for the PST films, which shows that the films are cation-ordered to a large extent. The superstructure reflections observed by XRD is shown in Fig. 4.3.3 (b).

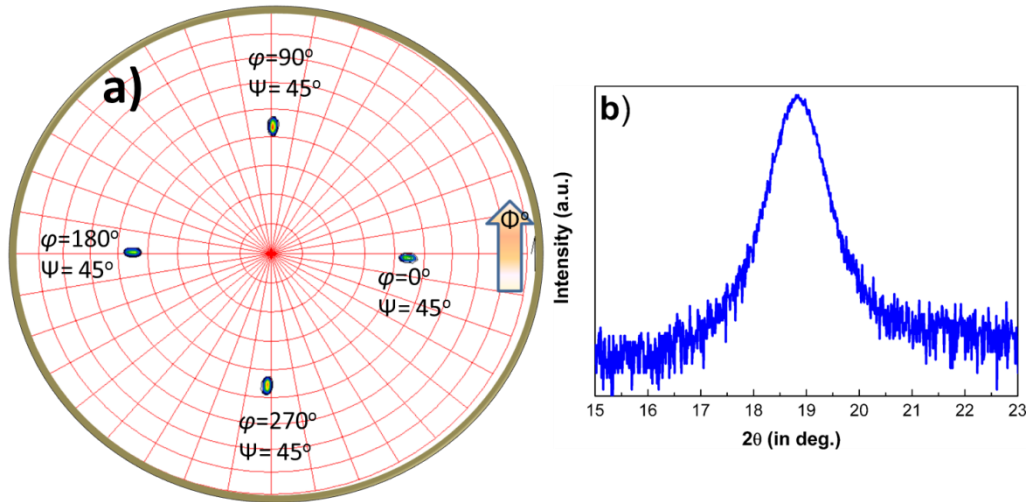


Fig. 4.3.3. (a) Pole figure image showing only four maximum intensity peaks for PST, supporting the global epitaxy of PST films. (b) A superstructure reflection obtained for PST thin films tilted at ψ=54°.

In order to determine whether the heterostructure H2 is epitaxial, and to confirm the crystallographic orientation, φ and pole figure XRD scans were performed. The in-plane measurements are shown a Fig. 4.3.4 (a). The measurement conditions are the same for the heterostructure H1. As both SRO and PST have (110) out-of-plane orientations, the in-plane measurements were performed by using (200) reflections. For SRO and PST, 2θ was fixed for the (200) reflection with a tilt of ψ=45°. For Si and YSZ, as expected, ideal four fold symmetry was observed.

However, for SRO and PST, four identical sets of peaks positioned around the reflections corresponding to Si (202) were observed. A perfect epitaxy would require only two peaks positioned at the Si (202) position. The four peaks show the presence of twin domains in the films. Furthermore, the intensity of these SRO and PST peaks was divided over two peaks situated with an  $\phi$  angle difference ( $\Delta \phi$ ) of  $\sim 20^\circ$ . This in-plane rotation corresponds to an alignment of the SRO [111] and PST [111] unit-cell body diagonal with the [110] face diagonal of YSZ. A top view of the heterostructure is illustrated in Fig. 4.3.4 (b). This type of in-plane epitaxy has been observed earlier by Lee *et al* [4.3.1]. The out-of-plane and in-plane epitaxial relationship between the films, buffer layers and substrate was found to be (100) PST // (100) SRO // (100) YSZ // (100) Si and (110) PST // (110) SRO // (100) YSZ // (100) Si, respectively.

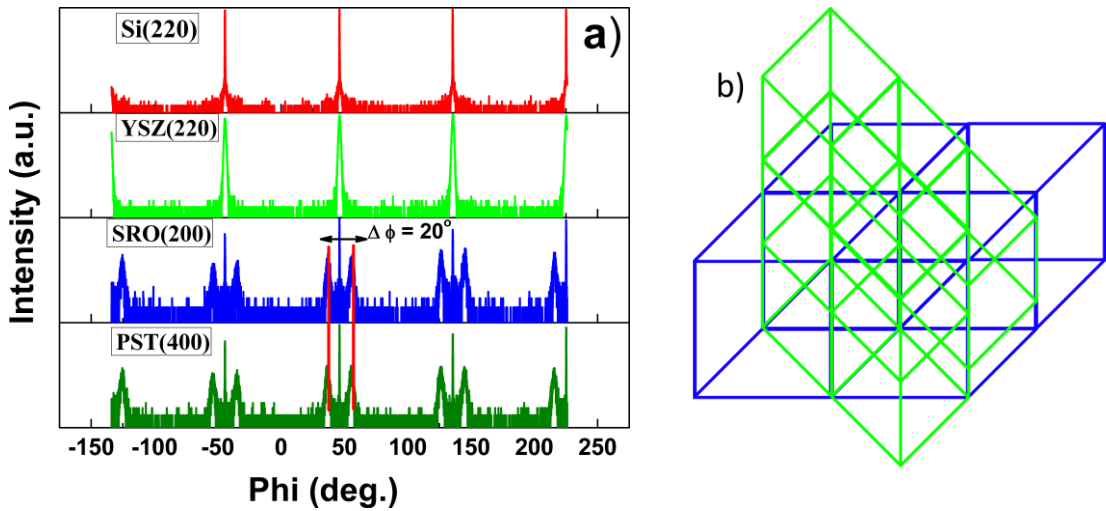


Fig. 4.3.4. (a)  $\phi$ -scan for PST on SRO/ YSZ/ Si showing that SRO and PST have twin domains; (b) A schematic showing the SRO diagonal growth on YSZ.

The FWHM values along (220) reflections for Si, YSZ, and (200) for SRO, and PST are  $\sim 0.17$ , 1.44, 1.64, and 1.35, respectively, indicating good crystallinity and epitaxial growth of PST, LNO and buffers layers on the Si substrate.

In order to check the epitaxial relationship of PST films, XRD pole figure measurements were performed. The sample was fixed at  $2\theta$  for a (200) reflection of PST and curves were recorded by varying  $\phi$  ( $0^\circ$ - $360^\circ$ ) and psi ( $\psi$ ) ( $0^\circ$ - $90^\circ$ ) values. Similar to  $\phi$ -scans, only four sets of peaks were observed. This shows PST has been grown epitaxially on global scale as shown in Fig. 4.3.5 (a). In this case, the cation-ordering parameter is estimated to be 0.31, which shows the films are cation ordered as well. The superstructure reflection observed by XRD is shown in Fig. 4.3.5 (b).

In order to analyze the status of strain present in PST thin films, reciprocal space mapping (RSM) measurements were performed. Through reciprocal lattice mapping both in-plane and out-of-plane lattice parameters were measured. As explained in Chapter 4.2, in order to determine the lattice parameters by RSM, a

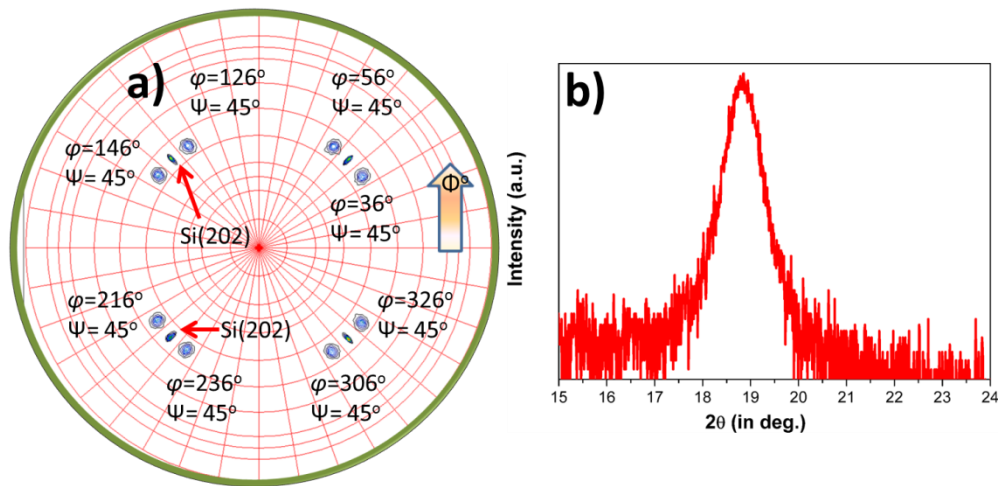


Fig.4.3.5. (a) Pole figure measurement confirming the global epitaxy for the PST films. (b) Superstructure reflections obtained for PST films by tilting it at  $\psi=35.3^\circ$ .

certain reflection which should not be perpendicular to any of the unit cell axes should be chosen. Otherwise, the lattice constant of this axis cannot be determined. In case of heterostructure H1, (440) reflections for Si, YSZ, CeO<sub>2</sub> and (204) reflections for LNO, PST were selected for the measurements. Using the relationship 3.3 and 3.4 (Chapter 3), the lattice parameters were calculated. Fig. 4.3.6 (a) shows the reciprocal space maps of CeO<sub>2</sub>/YSZ/Si (001) epitaxial films.

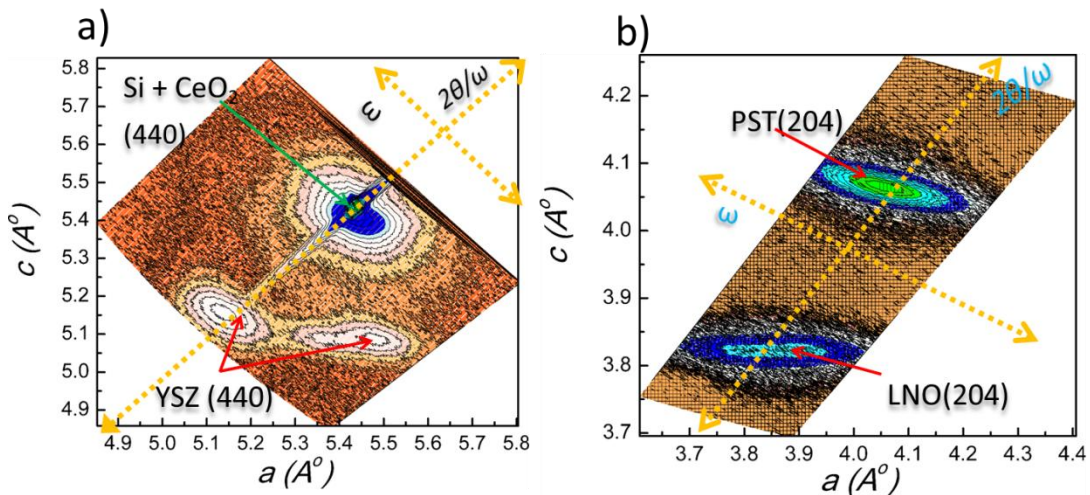


Fig.4.3.6. The reciprocal space maps of the (a) (440) reflections from CeO<sub>2</sub>/YSZ/Si (001) epitaxial films and (b) (204) reflections from PST/LNO (001) epitaxial films. The scan directions  $2\theta/\omega$  and  $\omega$  of the two axes are also illustrated.

The lattice parameter of CeO<sub>2</sub> is close to that of Si, therefore the reciprocal lattice point of CeO<sub>2</sub> overlaps with that of Si. The in-plane and out-of-plane lattice parameter of Si and CeO<sub>2</sub> have been found to be 5.43 Å. This shows that the CeO<sub>2</sub> layer is fully relaxed on the Si substrate. In case of YSZ two interconnected reciprocal space patterns were observed. As it can be clearly seen from the Fig. 4.3.6 (a), few layers of YSZ are having the same in-plane lattice parameter as that of Si. The in-plane and out-of-plane lattice parameter values of these few layers of YSZ are 5.43 Å and 5.10 Å, respectively. This indicates that only few YSZ layers were tensile stressed. With increase in thickness of the YSZ layer, the films start to relax and exhibit another reciprocal pattern connected with the stressed layers pattern. The RSM measurements of the LNO and PST are shown in Fig. 4.3.6 (b). The in-plane and out-of-plane values are tabulated in table 4.3.1. The difference between in-plane and out-of-plane lattice parameter values for the LNO film confirms that the films are tensile stressed. The in-plane and out-of-plane parameters for the top PST layer shows that the PST film is relatively relaxed on the LNO electrode, although there is still a slight difference in the in-plane and out-of-plane lattice parameters. In case of heterostructure H2, it was difficult to measure the RSM as the SRO and PST films were strongly twinned.

<i>Material</i>	<i>In-plane parameter (Å)</i>	<i>Out-of-plane parameter (Å)</i>
<b>Si</b>	5.43	5.43
<b>YSZ</b>	5.14	5.14
<b>CeO<sub>2</sub></b>	5.43	5.43
<b>LNO</b>	3.87	3.82
<b>PST</b>	4.07	4.05

Fig.4.3.1. Tabulated values of in-plane and out-of-plane lattice parameters for the different layers including the Si substrate.

### 4.3.3 TEM investigations

The internal microstructure and thickness of PST, electrode and buffer layers were determined by TEM investigations. The cross-section TEM with SAED patterns for H1 is shown in Fig. 4.3.7 (a-b) indicating the epitaxial growth of the PST film on the LNO bottom electrode layer. The SAED pattern confirms the exact cube-on-cube epitaxy of CeO<sub>2</sub>, YSZ (001) on Si (001). For the sake of clarity these are visualized



by the orange ( $\text{CeO}_2$ ) and blue (YSZ) colours squares formed by their corresponding reflections in Fig. 4.3.7 (b). PST and LNO films have been observed to have  $45^\circ$  in-plane rotation with respect to Si and buffer layers as shown by the red and green squares respectively, which is in agreement with the XRD investigations. As compared to PST and LNO layers, the buffer layers have a better quality of growth. This can be understood on the basis of lattice mismatch to Si which is less when compared to LNO and PST. The heterostructures have a high density of misfit

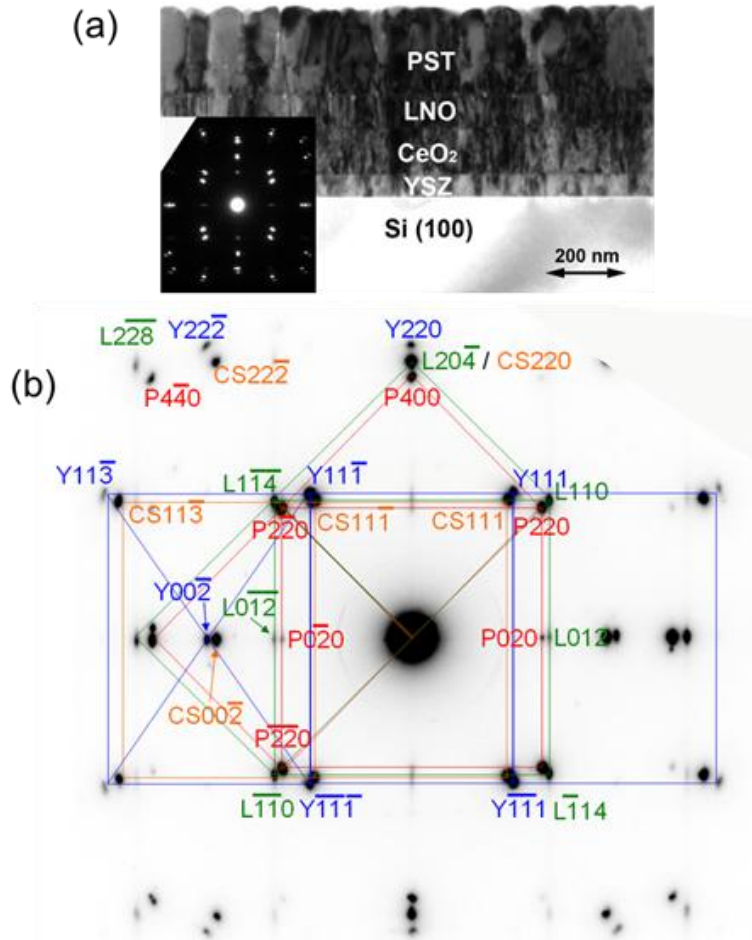


Fig. 4.3.7. (a) Cross-section TEM image of a grown heterostructure showing the thickness of the films and buffer layers. The thickness of PST, LNO,  $\text{CeO}_2$  and YSZ was found to be 200 nm, 80 nm, 115 nm, and 55 nm respectively. Inset: SAED pattern confirming the epitaxial growth of all the layers. (b) Indexed SAED pattern from the inset of (a), however, rotated by  $90^\circ$  for convenient indexing. LNO is indexed hexagonally here. The substrate orientation had been assumed to be Si (010). (P – PST; L – LNO; Y – YSZ; CS –  $\text{CeO}_2$  and Si;  $\text{CeO}_2$  and Si are not discernable from each other.)

dislocations. Threading dislocations were observed to emerge from the misfit dislocations and propagate into the surface of the PST film. PST and LNO have in-plane rotation with respect to substrate and buffer layers, which results in different contrast of the grains in the TEM image due to the different diffraction intensities of the azimuthally rotated domains.

The cross-sectional TEM image with SAED patterns for Si (100)/YSZ (100)/SrRuO<sub>3</sub> (110)/PST (110) is shown in Fig. 4.3.8 (a-b). The thickness of YSZ, SRO and PST were found to be 85 nm, 50 nm, and 90 nm respectively. The PST/SRO interface shows a specific roof-like morphology while the YSZ is flat and smooth. The SAED patterns show the epitaxial growth of each layer on Si substrate in accordance with our XRD investigations. An amorphous SiO<sub>2</sub> layer of 2 nm was observed between the interface of YSZ and Si in HRTEM investigations. This oxide layer is usually formed during the growth process of YSZ layer due to the diffusion of O<sub>2</sub> from YSZ to Si. No interdiffusion was observed between different interfaces in heteroepitaxial growth.

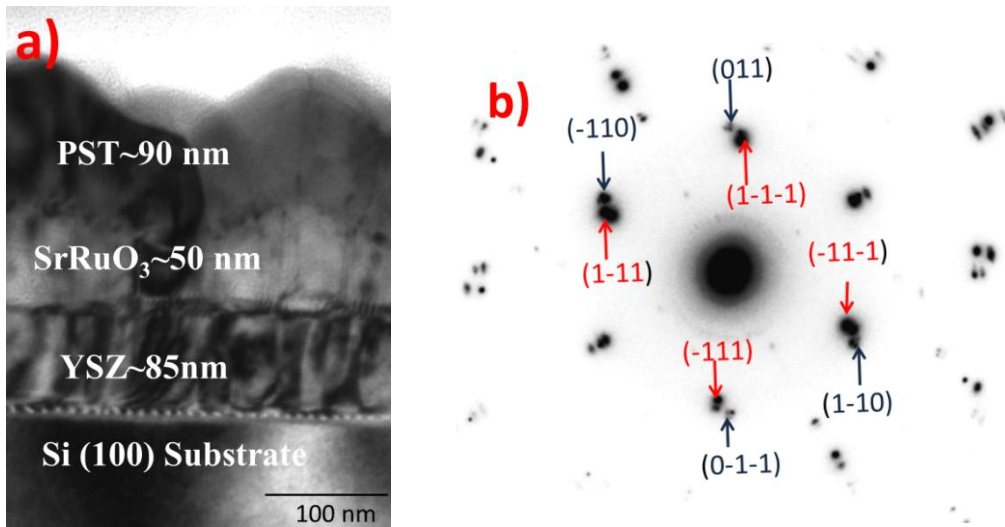


Fig. 4.3.8. (a) Cross-section TEM image of a grown heterostructure. (b) Indexed SAED pattern. Red colour indexing belongs to Si and YSZ, and dark blue colour indexing belongs to SRO and PST layers.

#### 4.3.4. Electrical measurements

Macroscopic ferroelectric properties of PST (100) and PST (110) thin films deposited on buffered Si substrates were investigated at RT as well as at low temperatures. P-V and I-V hysteresis loops recorded for H1 at RT using a 1 kHz frequency by using a triangular waveform is shown in Fig. 4.3.9 (a). The loops recorded for the heterostructure H2 at RT were leaky and high leakage current hindered the ferroelectric properties. A P-V and I-V hysteresis loop recorded for this



heterostructure at 100 K is shown in Fig. 4.3.9 (b). As it can be seen the loops are lossy even at low temperature. The apparent values of remnant polarization  $P_r$  and coercive voltage  $V_c$  are  $18 \mu\text{C}/\text{cm}^2$  and 2 V, respectively for H2. As discussed in the TEM section, PST on SRO has a high density of defects because of large misfit, which induces strain and twin domains in both SRO and PST. The high defect density degrades the electrical properties of the PST thin films.

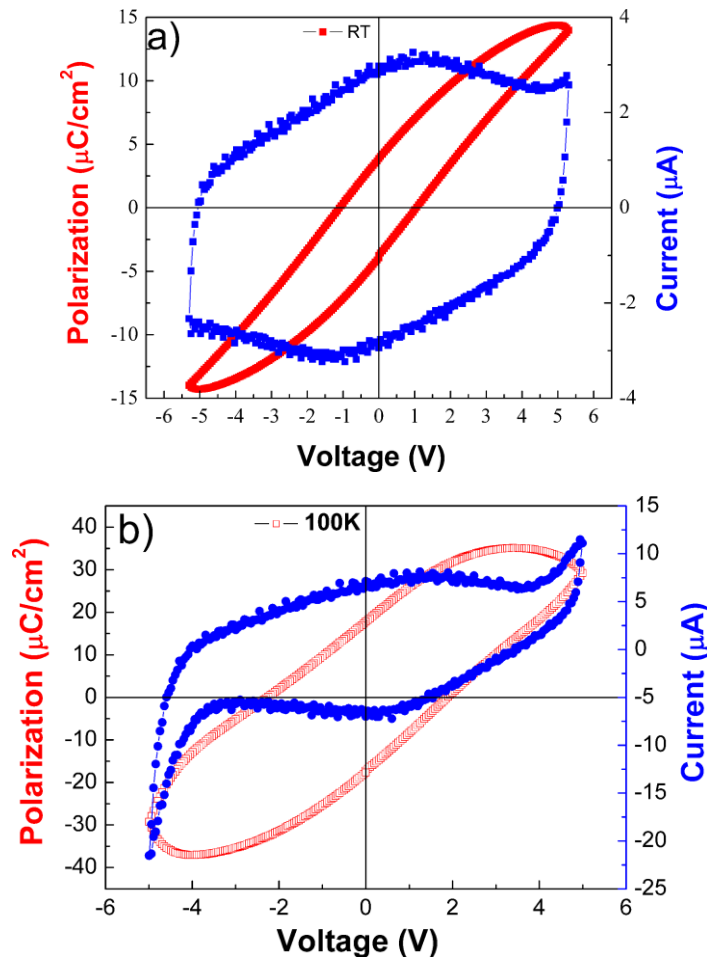


Fig. 4.3.9. Macroscopic polarization-voltage and switching current-voltage hysteresis measurement curves of (a) a Si (100)/YSZ (100)/CeO<sub>2</sub> (100)/LaNiO<sub>3</sub> (100)/PST (100) measured at RT. (b) Si (100)/YSZ (100)/SrRuO<sub>3</sub> (110)/PST (110) at 100K.

As discussed in Chapter 3 in electrical measurement techniques, simple hysteresis loops measured at a single frequency are not a sufficient condition for a material to be a true ferroelectric. In order to find the true nature of hysteresis, P-V and I-V curves were measured at 100 Hz, 1000 Hz and 2000 Hz frequencies. Typical curves are shown in Fig. 4.3.10. As clear from the I-V curves, there is a strong frequency dependence of the switching currents, which demonstrate that the films are truly ferroelectric. For H1 at RT, the remnant polarization  $P_r$  and coercive voltage  $V_c$

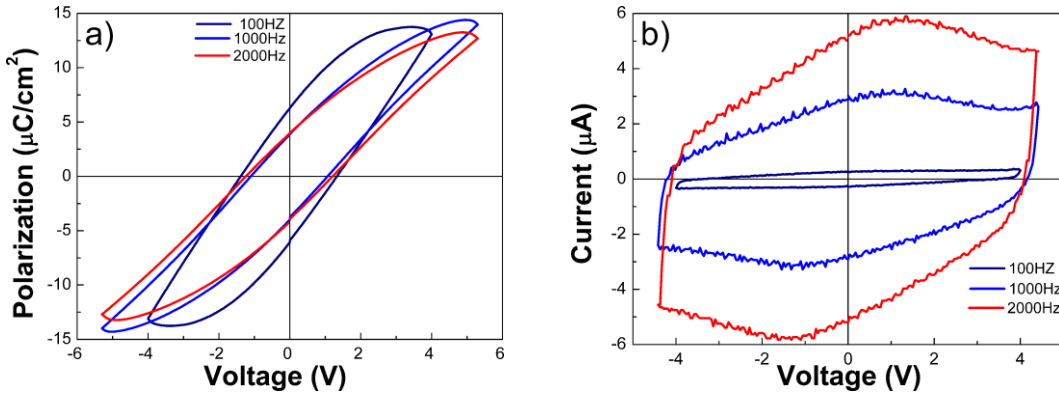


Fig. 4.3.10. Macroscopic polarization-voltage and current-voltage hysteresis curves recorded at 0.1, 1 and 2 kHz for H1.

are about  $4 \mu\text{C}/\text{cm}^2$  and 1.2 V, respectively. The ferroelectric properties investigated for H1 at low temperatures are shown in Fig. 4.3.11. The films demonstrated good ferroelectric properties at low temperatures.

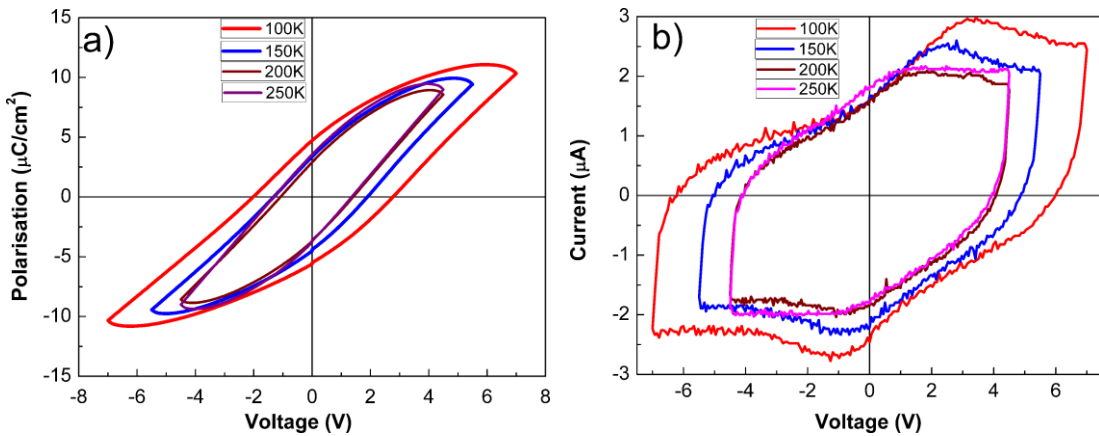


Fig. 4.3.11. (a) Macroscopic polarization-voltage and (b) switching current-voltage hysteresis measurement curves recorded at 1 kHz at various temperatures from 100 K to 250 K.

The hysteresis started to become slim with increase in temperature. The remnant polarization  $P_r$  and coercive voltage  $V_c$  are about  $5.23 \mu\text{C}/\text{cm}^2$  and 2.39 V, respectively at 100 K. These values are less when compared to the PST (110) values, as expected because of the rhombohedral structure of PST. The films are also ferroelectric at high temperatures (Fig. 4.3.12).

With the increase in temperature, hysteresis loops became slimmer showing that the PST films are reaching the  $T_B$  range. Nevertheless, 400 K films were

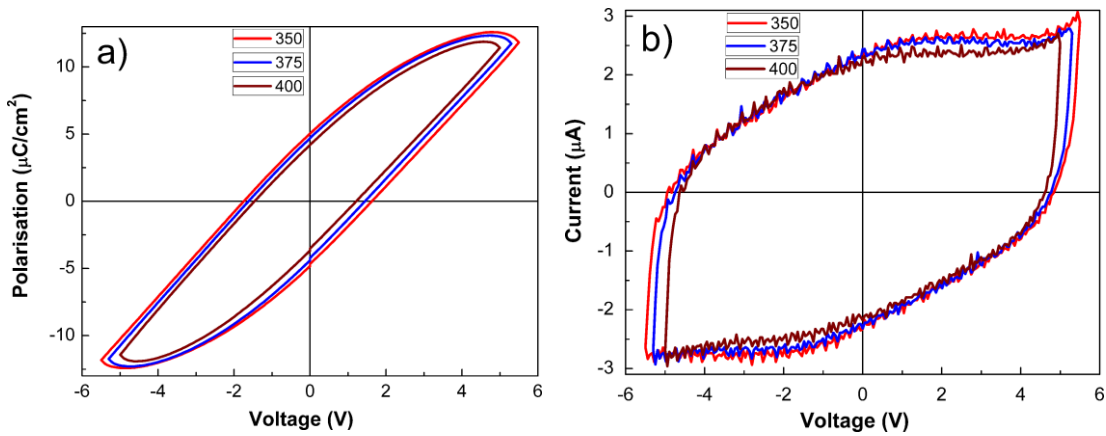


Fig. 4.3.12. (a) Macroscopic polarization-voltage and (b) switching current-voltage hysteresis measurement curves recorded at 1 kHz for high temperatures.

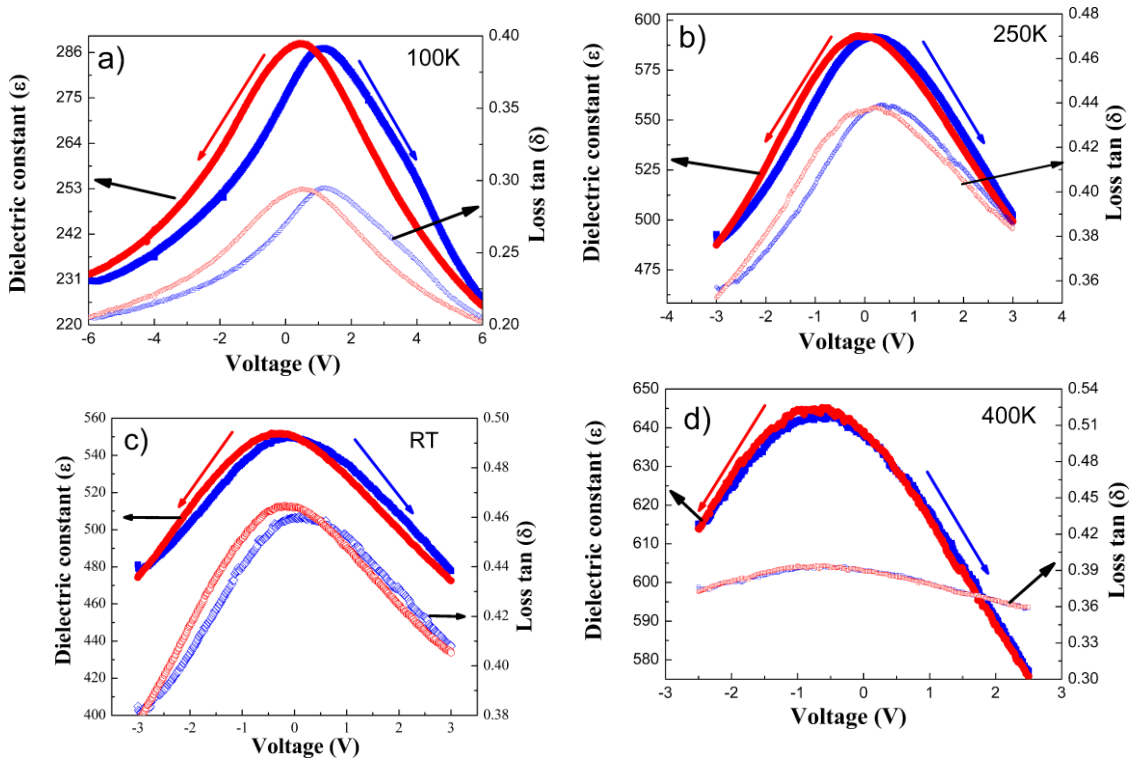


Fig. 4.3.13. Voltage-dependent dielectric constant at different temperatures of a PST/LNO/CeO<sub>2</sub>/YSZ/Si from C-V measurements assuming the plan-parallel capacitor model.

showing the ferroelectric properties. The ferroelectric properties were confirmed by measuring the field dependent dielectric constant. Dielectric constants were calculated from the capacitance measured by a Hewlett Packard 4194A impedance

analyzer using a small ac signal of 100 mV. The C-V curves were recorded for different temperatures at 100 kHz frequency as shown in Fig. 4.3.13. The results obtained from these curves at low as well as high temperatures are in accordance with the hysteresis loop measurements. At RT for a frequency of 100 kHz, the value of the dielectric constant and loss tangent were around 560 and 0.4, respectively, at 0 V. It can be found that with the increase in temperature, there is increase in dielectric constant, although at 250 K, the dielectric constant is larger as compared to 300 K. This will be discussed in a later section.

#### 4.3.5. Non-linear dielectric and piezoelectric behaviour of PST films.

The piezoelectric properties of PST thin films were investigated through PFM measurements. As explained in Chapter 4.2, the piezoelectric coefficient is usually determined by measuring the PFM signal amplitude at different excitation voltages. The  $d_{zz}$  value is given by the slope of the plot of  $S_{PFM}$  vs.  $V_{ac}$  in the low  $V_{ac}$  range. However, similar to the PST/ LSMO/ STO heterostructure, instead of getting one single slope two slopes were observed as shown in Fig. 4.3.14.

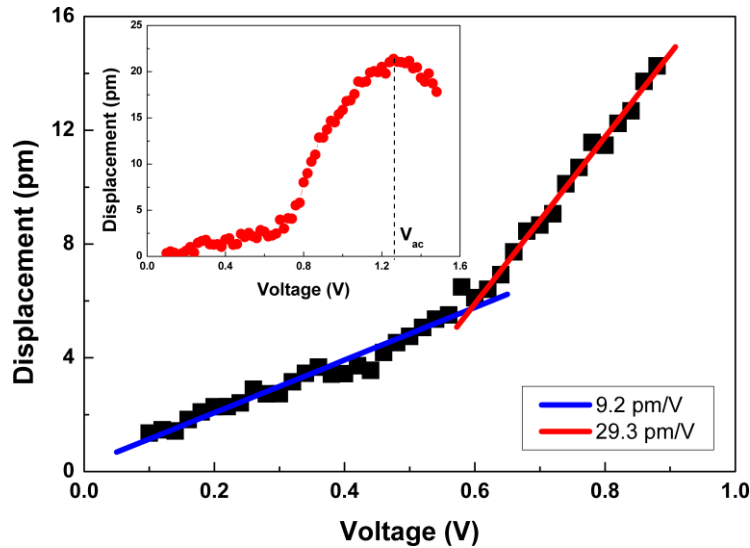


Fig. 4.3.14. Piezoresponse of the PST film as a function of the applied voltage. PFM signal at higher voltage showing strong non-linear behavior at coercive voltage ( $V_c$ ).

The piezoelectric coefficient in the low voltage range ( $<0.6V$ ) is 9.2 pm/V. On applying a higher ac voltage, a sudden increase in the piezoelectric coefficient to 29.3 pm/V was observed. This is observed at  $V_{ac}$  values well below the coercive voltage ( $V_c$ ). In this case  $V_c$  is around 1.2 V as shown in inset of Fig. 4.3.14. The above effect was also shown in imaging using PFM. It was shown that there is a

strong and irreversible influence of the  $V_{ac}$  on the PFM signal. With the increase in amplitude of ac voltage, the PFM signal becomes stronger. At  $V_{ac}=0.25$  V, there is only a noisy phase with low amplitude. However, at 0.50 V, a preferred direction of the phase signal was observed. As the voltages approaching the coercive voltage, a strong signal of upward polarization (dark contrast/negative phase signal) was observed as shown in Fig. 4.3.15 (a-d). Similar to PST/ LSMO/ STO, the effect of the applied ac voltage is irreversible. It was observed that on applying a high ac field, the piezo-response never returned to its original value after removal of the external field, but remains always higher than its previous value. Fig. 4.3.16 shows a piezo-response curve recorded for three cycles.

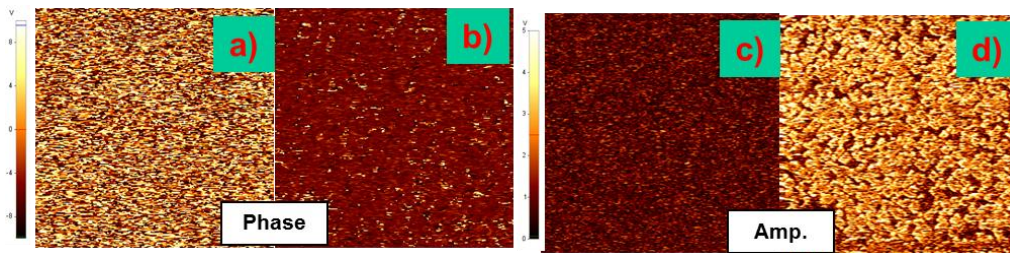


Fig. 4.3.15. A PFM piezo-response image ( $3 \times 3 \mu\text{m}^2$ ) of a PST film. (a-b) A phase image scanned with 0.25 V and 1 V, respectively; (c-d) An amplitude image scanned with 0.25 V and 1 V, respectively, showing the strong change from low piezo-response to high piezoresponse with applied ac voltage.

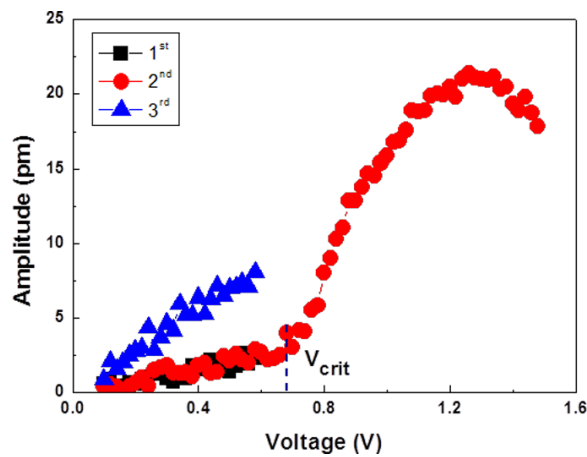


Fig. 4.3.16. Piezoresponse of the PST film as a function of the applied ac voltage showing an increase in the piezoelectric coefficient for the other cycle than before.

The first cycle was swept from 0 V to low values under the critical field; the second scan was swept to the coercive voltage and a final scan in the low level range showed that the piezoelectric coefficient remained irreversible at high level. As explained in

Chapter 4.2, this kind of behavior is unusual for a ferroelectric material. According to equation 4.2.2, the PFM amplitude can be influenced by three factors: dielectric constant, polarization and electrostriction coefficient.

In order to find which one of the above factors is responsible for the non-linear behavior, macroscopic measurements of dielectric constant at variable applied ac voltage were performed. Similar to the piezoelectric response, a sharp increase in dielectric constant was observed near 0.6 V for 1 kHz as shown in Fig. 4.3.17 (a). As in the case of piezoelectric coefficient, the dielectric constant never came back to the virgin value of dielectric constant, but it remains higher than the pristine value as shown in Fig. 4.3.17 (a). The dielectric constant for the pristine sample at 0.1 V was found to be 525 and for reverse cycle it was found to be 531 with 0.09 losses for both the cycles. The critical field is close to the value determined by PFM. Thus, it is highly probable that the non-linear piezoelectric behavior is due to this non-linear behavior of the dielectric constant.

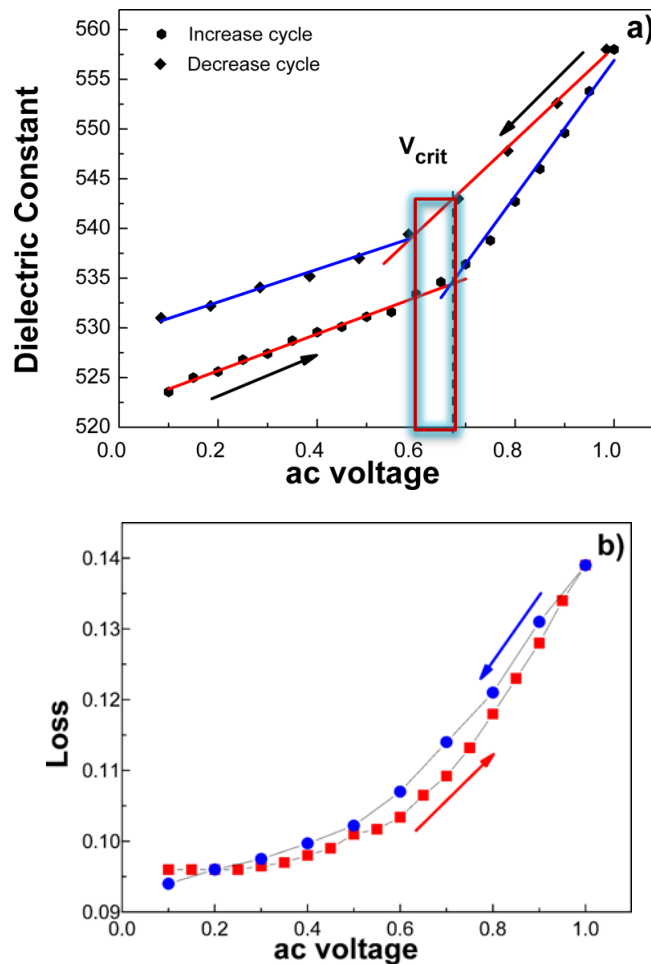


Figure 4.3.17 (a) Dielectric constant variation of the PST film as a function of the applied ac voltage showing a sharp increase in dielectric constant at critical voltage  $V_{crit} = 0.6$  to  $0.7$  V. (b) Variation in dielectric loss with the applied voltage.

Also, in order to check this we have addressed the frequency dependence of dielectric constant additionally. According to the Rayleigh model, the non-linearity is reduced with increase in frequency [4.3.2]. In our case there was no reduction observed in non-linearity with the frequency. The magnitude of sharp increase was the same for all the frequencies as shown in Fig. 4.3.18. In literature it is reported that in the non-linear region of dielectric constant the losses are highly dependent on frequency and there is a sharp increase in losses, but in the PST, no such phenomenon was observed. Further, as explained in the previous Chapter the Rayleigh model explains the dielectric non-linearities on the basis of domain wall motion. Relaxors like PST do not possess classical ferroelectric domains. As it was shown, there are only polar nano-domains. The possible mechanism for this kind of dielectric non-linearity is explained in Chapter 4.2.5.

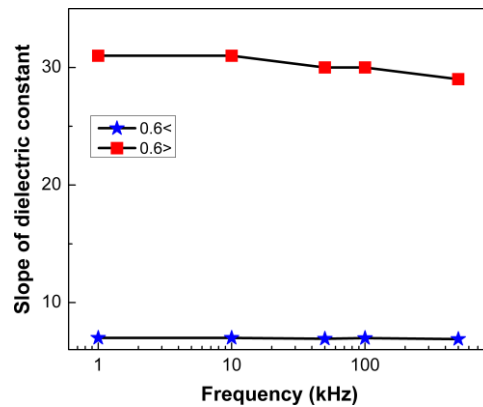


Figure 4.3.18 Variation of slope of dielectric constant with frequency. The blue color points show the slopes measured below  $V_{crit}$  and red color points are above it.

Similar to the PST/LSMO/STO heterostructure, the possibility of a phase transition near to RT was checked by dielectric constant variations with temperature. The measurements were performed by using a small ac voltage of 0.1 V to avoid the influence of applied voltage on phase transition. A typical curve recorded for four different frequencies is shown in Fig. 4.3.19. In case of relaxors, a diffuse and frequency dependent dielectric constant maximum is generally expected [4.3.3]. But our data show very sharp dielectric maxima independent of frequencies. The dielectric maxima for all the frequency are observed around 275 K. By scanning the temperature from low to high values, the dielectric constant was found to rise up constantly. At the transition temperature it dropped sharply after which it decayed slowly. The transition resembles a first order phase transition but with paraelectric phase at low temperatures and ferroelectric phase at RT.

In order to check whether the Curie-Weiss law is valid at  $T < T_o$ , we plotted the reciprocal values of dielectric constant ( $\epsilon$ ) vs. temperature as shown in Fig. 4.3.19



(c). From the low temperature range the Curie-Weiss temperature ( $T_o$ ) is about 270 K.

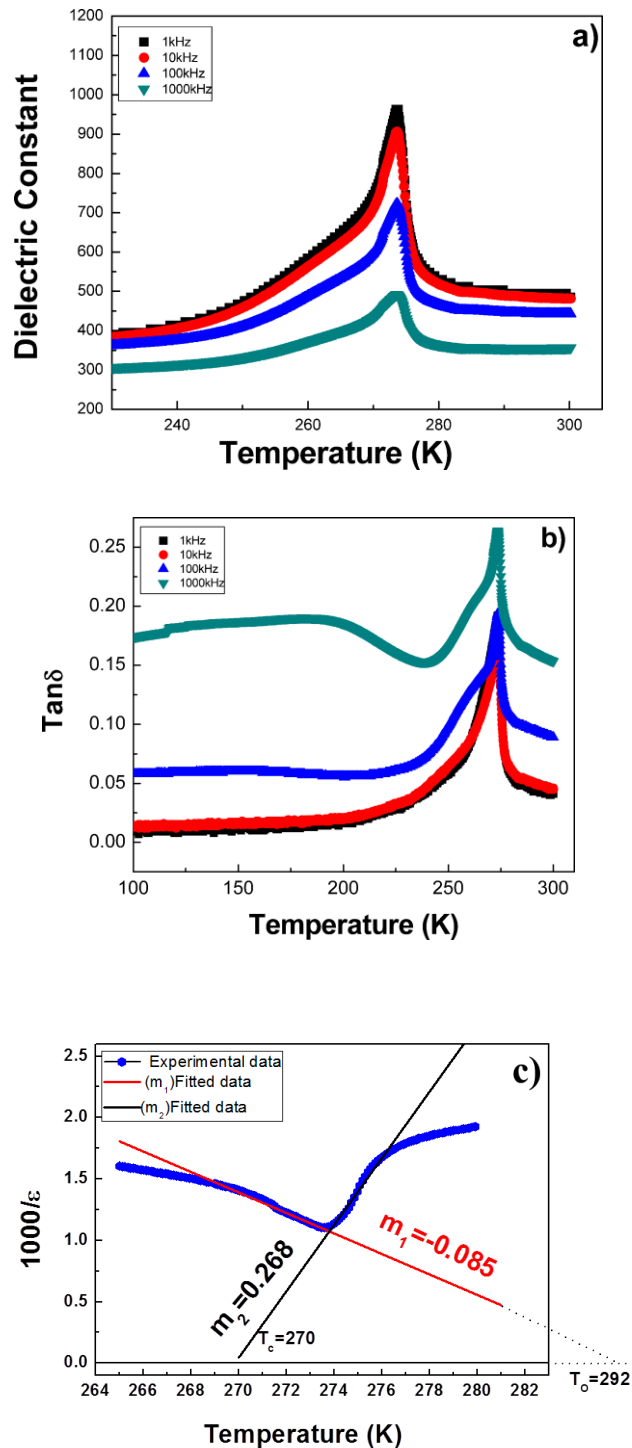


Fig. 4.3.19. (a) Temperature dependence of dielectric permittivity for four different frequencies. (b) Losses measured as a function of temperature for different frequencies. (c) Shows the reciprocal of the dielectric permittivity experimental data fitted to the Curie-Weiss law.



The slopes of  $\epsilon$  before  $T_c$  are about four times larger than the slope after  $T_c$ . This is also a finger print characteristic of first order phase transition [4.3.4]. This first order phase transition might describe a ferroelectric-ferroelectric phase transition which is specific only for the thin films.

### 4.3.6 Summary

Epitaxial (100) and (110) oriented PST thin films have been grown successfully on buffered Si substrates. The films deposited on CeO<sub>2</sub> and YSZ buffered Si substrates were found to have in-plane 45° rotation with respect to Si. PST films deposited on only YSZ buffered Si substrates were found to have an out-of-plane rotation with respect to the Si substrates. PST (110) films proved to have twin domains which degraded the ferroelectric properties. All the films showed 1:1 chemical ordering, which was confirmed through superstructure reflections obtained using *XRD* measurements. The PST (100) films exhibit good ferroelectric properties in a temperature range from 100 K to 400 K. The ferroelectric properties of PST (110) were hindered by a high leakage current originating most probably from twin domains and other microstructure defeats. The dielectric constant and loss tangent for PST (100) films were around 560 and 0.4, respectively, at 100 kHz. The piezoelectric response shows an unusual non-linear behavior. The piezoelectric coefficient at low voltages was found to be 9.2 pm/V. At high field, the piezoelectric coefficient increases to 29.3 pm/V. The threshold was about 0.6 V which is equivalent to a 30 kV/cm field. A similar effect was observed in dielectric permittivity under the application of variable ac voltage. The most probable mechanism of this effect is percolation of nano-polar regions in PST. Phase transition measurements show a first-order ferroelectric to ferroelectric phase transition at 270 K. This work on buffered Si substrates shows we are one step closer to using epitaxial PST in Si based technology.

## Chapter 5 Conclusions and future prospectus

In this study, epitaxial and ferroelectric  $\text{PbSc}_{0.5}\text{Ta}_{0.5}\text{O}_3$  (PST) films have been successfully grown by pulsed laser deposition. In literature there was up to now no report addressing the cation-ordering status in epitaxial PST films prepared by PLD. Thus we took this challenge as an opportunity to explore effects related to the cation-ordering processes in the films. The fabricated films were thoroughly structurally characterized by XRD, (HR) TEM, and AFM. The macroscopic ferroelectric and dielectric properties of the films were investigated by ferroelectric loops and capacitance-voltage loops, respectively. The local ferroelectric and piezoelectric properties were investigated by piezoelectric force microscopy measurements. The influence of growth parameters on microstructure and electrical properties is discussed in this work. The degree of cation-ordering was studied in the PST films by varying the thickness of the films. Especially the influence of scaling down the film thickness on cation-ordering and ferroelectric properties is investigated. From this research, the following major conclusions have been made:

- Epitaxial, highly cation-ordered and ferroelectric PST (100) films were fabricated on SRO/STO (100) from a self-made target. It was found that the films were highly sensitive to the growth conditions. Depositions at other than optimized conditions were resulting in a very rough surface morphology and pyrochlore phase. The film deposition conditions show equilibrium between deposition temperature and laser flux for having films without pyrochlore phase. The films grown in optimized conditions have terraces with a step height of about 3 nm, and the root mean square value of roughness for the terraces was about 0.28 nm over an area of  $0.3 \times 0.3 \mu\text{m}^2$  signifying a flat and smooth surface. Along with films deposited at high laser flux and temperature, two optimized set of films with 60 nm and 77 nm thickness were studied for investigating the influence of cation-ordering with thickness. The phase confirmed by XRD measurements was pure perovskite phase. The in-plane and out-of-plane XRD measurements confirm a perfect cube on cube

and epitaxial growth. The degree of cation-ordering calculated from the superstructure reflections obtained in the in-plane XRD for PST films of 60 nm and 77 nm thickness was 33% and 35%, respectively. TEM investigations showed that SRO has coherent growth on STO, although the PST/SRO interface has a high density of misfit dislocations. The average spacing between misfit dislocations was around 10 nm which was in good agreement with theoretical formulations. The superstructure reflections obtained in TEM SAED patterns further confirm the cation-ordering in these films and support the XRD results. There was an interesting observation that thin films (60 nm) have an ordered domain size of 5 nm and thick films (77 nm) have 10 nm. This shows that cation-ordering depends on film thickness. The influence of cation-ordering and microstructure was investigated by electrical measurements. It was found that the films prepared with high flux and at a temperature higher or/and lower than optimum temperature (550 °C) show high leakage and no ferroelectricity. On the other hand, films deposited under the optimized conditions showed good ferroelectric properties. At RT, a remnant polarization of  $0.3 \mu\text{C}/\text{cm}^2$  and coercive voltage of 0.28 V were found for the 60 nm thin films. For the 77 nm thick films, the remnant polarization and coercive voltage were found to be  $3.4 \mu\text{C}/\text{cm}^2$  and 0.6 V, respectively at RT. In comparison to 60 nm thin films, the higher values of remnant polarization and coercive voltage for 77 nm thick films were attributed to the influence of the higher degree of cation ordering and larger size of domains compared to the former case. The dielectric constant for the 60 nm and 77 nm thick films was found to be 400 and 460 respectively, at 1 kHz frequency with losses lower than 0.01 at RT. The lower values of dielectric constant in comparison to the already reported values for polycrystalline films, were attributed to the absence of extrinsic contributions such as domain walls, grain boundaries *etc.* The local switching properties of the films were confirmed through PFM measurements.

Since PST has a rhombohedral structure with polarization pointing in (111) direction, PST (111) films were deposited on SRO/STO (111) substrates. The films have a pure perovskite phase with 33% degree of cation-ordering. In comparison to the PST (100) films, the (111)-oriented films were having higher surface roughness. TEM investigations show that the films were cation-ordered, but have a high density of misfit dislocations at the PST/SRO interface compared to the (100)-oriented films. This has been attributed to the larger mismatch in the former case than the latter. The influence of a high density of misfit dislocations was observed in the ferroelectric properties. At RT, the remnant polarization and coercive voltage of (100)-oriented film were found to be  $2.27 \mu\text{C}/\text{cm}^2$  and 0.27 V, respectively, which are lower than the values observed in case of (100)-oriented film.

- The effect of in-plane strain on the PST films was studied by scaling down the thickness to 30 nm and using LSMO as bottom electrode. The film shows an ideal epitaxial growth with four-fold symmetry. The in-plane and out-of-plane lattice parameter measured by reciprocal lattice mapping for the PST films were 4.05 Å and 4.09 Å, respectively, which shows that the films are under compressive stress. No cation-ordering was observed in the films, which is attributed to the thickness and strain effect in the films. The film investigated by TEM shows no degree of cation-ordering at RT as well as at low temperatures. Structural investigations suggest that the structure of strained PST films is rather tetragonal. The influence of tetragonality is obvious in the electrical properties of PST films. The remnant polarization and coercive voltage increased to 17  $\mu\text{C}/\text{cm}^2$  and 1.3 V, respectively compared to (100)-oriented films. A strong non-linearity was observed in piezoelectric behaviour. The local piezoelectric coefficient increases drastically from 3 pm/V to 23.3 pm/V at a critical voltage of 0.6 V. A similar non-linear behavior has been observed in case of the dielectric constant. The critical field of both piezoelectric coefficient and dielectric constant is the same within the experimental error. Thus it has been concluded that this unusual behavior is largely due to the non-linear behavior of the dielectric constant. The dielectric non-linearity in ferroelectrics is generally explained on the basis of reversible and irreversible domain wall motion in the framework of the Rayleigh model. In the present case the observed non-linearity does not fit well with the Rayleigh model. In order to explain the dielectric non-linearity, two mechanisms were considered: 1) percolation of polar nano regions and 2) field induced phase transition. In order to check the possibility of a field induced phase transition, the temperature dependence of the dielectric constant was measured. A second-order ferroelectric to ferroelectric phase transition at 265 K was observed.
- PST films have been grown on Si substrates by using YSZ and  $\text{CeO}_2$  as buffer layers and  $\text{LaNiO}_3$  (LNO) as bottom electrode. The PST films (200 nm) were (100) oriented with in-plane rotation by an azimuthal angle of  $45^\circ$  with respect to the buffer layers and implicitly the substrate as confirmed by XRD and TEM investigations. The in-plane and out-of-plane lattice parameters measured by reciprocal lattice mapping showed that the PST films were relaxed. The films were having 42% degree of cation-ordering. Because of the larger mismatch between PST and the underlying layers, PST shows columnar growth with high density of misfit dislocations. The ferroelectric properties were investigated in the temperature range from 100 K to 400 K. The remnant polarization and coercive voltage at RT are about 4  $\mu\text{C}/\text{cm}^2$  and 1.2 V, respectively for the PST (100) films. The dielectric properties were investigated in the temperature range of 100 K to 400 K showing a dielectric constant of 560 for 100 kHz frequency at RT. Similar to the PST (100) on

LSMO/STO (100), a strong non-linearity was observed in the piezoelectric and dielectric response. In contrast, the phase-transition measurements show in this case a first order ferroelectric-ferroelectric phase transition, which might be related to cation-ordering.

In case of the second heterostructure, PST films were deposited on SRO as bottom electrode. The films were epitaxial with (110)-orientations with respect to the Si (100) substrate. The in-plane measurements revealed the presence of twin domain inside the PST films. The films were cation-ordered and 33% degree of cation-ordering was calculated through superstructure reflections obtained in XRD measurements. The TEM investigations show that the films had a roof like morphology and a higher density of misfit dislocations in comparison to the first heterostructure. The presence of a high density of microstructure defects influenced the ferroelectrics properties of the films. The films show a high leakage current at RT which hinders the ferroelectric properties of PST films. However at 100 K, the apparent values of remnant polarization and coercive voltage are about  $18 \mu\text{C}/\text{cm}^2$  and 2 V, respectively.

### **Future prospects and outlook**

As we know, in the recent years there has been considerable interest in relaxors. In comparison to normal ferroelectrics, these materials are comparatively new and thus offer plenty of room to explore new and exciting physics leading to new applications. As shown here, PST is a very interesting system. Dielectric non-linearity is one of the puzzles which believed to be the result of percolation of polar nano regions and it needs further attention. In order to confirm this hypothesis in a definitive manner, neutron scattering and other structural experiments with the applied field are necessary. The phase transitions observed in case of ordered and disordered films open new questions. Before the present experimental evidence, bulk relaxors such as PST showed a diffuse and frequency dependent dielectric constant maximum. However in our films, neither was it diffuse nor frequency dependent. Thus it might be useful to do more structural and electrical investigations, in order to understand the influence of the strain on relaxor materials. I would therefore like to conclude my thesis by stating that the present work is just one more step in understanding the fascinating world of relaxor ferroelectrics. There is enough room in this relaxor world to not let you relax!

## References

### Chapter 1

- 1.1. R. E. Cohen. *Nature* **441**, 941 (2006).
- 1.2. Z. Kutnjak, J. Petzelt, and R. Blinc. *Nature* **441**, 956 (2006).
- 1.3. R. W. Whatmore. *Ferroelectrics* **118**, 241 (1991).
- 1.4. N. M. Shorrocks, R. W. Whatmore, and P. C. Osbond. *Ferroelectrics* **106**, 387 (1991).
- 1.5. A. Sosnin. *Semiconductor Physics Quantum Electronics & Optoelectronics* **3**, 489 (2000).
- 1.6. W. F. Kosonocky. *Optoelectronics* **6(2)**, 173 (1991).
- 1.7. C. Lucas. *Sensors and Actuators A* **25-27**, 147 (1991).
- 1.8. N. M. Shomks, S. G. Porter, R. W. Whatmore, A. D. Parsons, J. N. Gooding, and D. J. Pedder. *SPIE -Int.Soc.Opt.Eng.* **1320**, 88 (1990).
- 1.9. R. Watton. *Integr.Ferroelectr.* **4(2)**, 175 (1994).
- 1.10. William. D. Nothwang, and Arnold Goldberg. *The AMPTIAC Quarterly*, **8**, 111(2004).
- 1.11. A. Patel, P. C. Osbond, N. M. Shorrocks, R. C. Twiney, R. Whatmore, and R. Watton. *Proc. IEEE Int. Symp. Appl. Ferroelectr.* **9**, 647 (1994).
- 1.12. M. Kondo, K. Maruyama, and K. Kurihara. *FUJITSU Sci. Tech. J.***38**, 46 (2002).
- 1.13. C. D. Meekison, K. Z. Baba-Kishi, R. Watton, and M. A. Todd. *Integr.Ferroelectr.* **8**, 283 (1995).
- 1.14. M. A. Todd, P. P. Donohue, J. C. Jonesa, D. J. Wallis, M. J. Slater, M. A. Harper, and R. Watton. *Integr.Ferroelectr.* **25**, 113 (1999).
- 1.15. S. H. Pyke, K. Z. Baba-Kishi, R. Watton, and M. A. Todd. *Integr.Ferroelectr.* **4**, 25 (1994).
- 1.16. R. Watton. *Integr.Ferroelectr.* **4**, 175 (1994).
- 1.17. Z. Huang, M. A. Todd, R. Watton, and R. W. Whatmore. *J. Mats. Sci.* **33**, 363 (1998).
- 1.18. K. Brinkman, Y. Wang, D. Su, A. Tagantsev, P. Muralt, and N. Setter. *J. Appl. Phys.* **102**, 044110 (2007).
- 1.19. D. Liu and D. Payne, *J. Appl. Phys.* **77**, 3361 (1995).
- 1.20. A. Patel, N. Shorrocks, and R. Whatmore. *Ferroelectrics* **134**, 343 (1992). J. A. Bearden. *Rev. Mod. Phys.* **39**, 78 (1967).

- 1.21. C. J. Brierley, C. Trundle, L. Considine, R. W. Whatmore, and F. W. Ainger. *Ferroelectrics* **91**, 181 (1989).
- 1.22. S. Murakami, D. Popovici, K. Satoh, M. Matsumoto, M. Noda, and M. Okuyama. *Sens. Mater.* **16**, 231 (2004).
- 1.23. C. Bjormander, K. Sreenivas, A. M. Grishin, and K. V. Rao. *Appl. Appl. Phys. Lett.* **67**, 58 (1995).

## Chapter 2

- 2.1. D. Jones, S. Prasad, and J. Wallace. *Advanced Ceramic Materials*, **122–124**, 71(1996).
- 2.2. P. J. Curie and P. Curie. *Bull. Soc. Min. de France* **3**, 90 (1880).
- 2.3. J. Valasek. *Phys. Rev.* **15**, 537 (1920).
- 2.4. J. C. Slater. *J. Chem. Phys.* **9**, 16 (1941).
- 2.5. B. Wul and I. M. Goldman. *C. R. Acad. Sci. USSR* **46**, 12(1945).
- 2.6. M. E. Lines and A. M. Glass. *Principles and Applications of Ferroelectric and Related Materials*. Clarendon Press Oxford (2004).
- 2.7. K. A. Rabe, T. J.-M., and C. H. Ahn (eds.). *Physics of Ferroelectrics: A Modern Perspective*. Springer-Verlag (2007).
- 2.8. G. Shirane, S. Hoshino, and K. Suzuki. *Physical Review* **80**, 1105 (1950).
- 2.9. B. T. Matthias and J. P. Remeika. *Phys. Rev.* **76**, 1886 (1949).
- 2.10. W. P. Mason and B. T. Matthias. *Phys. Rev.* **74**, 1622 (1948).
- 2.11. J. C. Slater. *Phys. Rev.* **78**, 748 (1950).
- 2.12. W. Cochran. *Phys. Rev. Lett.* **3**, 412 (1959).
- 2.13. P. W. Anderson. In *Fizika Dielektrikov* (edited by G. I. Skanavi), Moscow (1960).
- 2.14. Hans Mueller. *Annals of the New York Academy of Sciences* **40**, 321 (1940).
- 2.15. A. F. Devonshire. *Philos. Mag.* **40**, 1040 (1949).
- 2.16. A. F. Devonshire. *Philos. Mag.* **42**, 1065 (1951).
- 2.17. J. A. Gonzalo, and B. Jiménez. *Ferroelectricity*. WILEY-VCH Verlag GmbH & Co. KGaA (2005).
- 2.18. W. Massa. *Crystal structure determination*. Springer-Verlag (2004).
- 2.19. R. V. Gaines, H. C. W. Skinner, E. E. Foord, B. Mason, and A. Rosenzweig. *Dana's new mineralogy*. JohnWiley & Sons, Inc. (1997).
- 2.20. L. W. Martin, Y.H.Chu, and R. Ramesh. *Materials Science and Engineering R* **68**, 89 (2010).
- 2.21. S. N. Ruddlesden, and P. Popper. *Acta. Crystallogr.* **11**, 54 (1958).
- 2.22. L. D. Landau. *Phys. Z. SowjUn*, 11, 26, (1937); L. D. Landau, and E. M. Lifshitz. *Statistical Physics*, Pergamon, London, (1959).
- 2.23. A. F. Devonshire. *Phil. Mag.*, **40**, 1040(1949); *Adv. Phys.*, **3**, 85, (1954).
- 2.24. K. Uchino. *Ferroelectric Devices*, Marcel Dekker Inc, New york, (2000).
- 2.25. K. Hirota, S. Wakimoto, and D. E. Cox. *J. Phys. Soc. Jpn.*, **75**, 111006 (2006).
- 2.26. G. A. Samara. *Solid State Physics*, **56**, 239 (2001).
- 2.27. G. A Samara. *Phys. Rev. B*, **71**, 224108 (2005).
- 2.28. A. A. Bokov, and Z.G. Ye. *J. Mater. Sci.*, **41**, 31(2006).
- 2.29. G. A. Smolenskii. *J.Phys.Soc.Japan* **28**, 26 (1970).
- 2.30. G. A. Smilenskii, V. A. Isupov, A. I. Agranovskaya and S. N. Popov. *Soviet Phys.-Solid State* **2**, 2584 (1961).

## References

---

- 2.31. L. E. Cross, *Ferroelectrics* **76**, 241 (1987).
- 2.32. D. Viehland, S. J. Jang, L. E. Cross, and M. Wutting. *J. Appl. Phys.* **68**, 2916 (1990).
- 2.33. V. Westphal, W. Kleemann and M. D. Glinchuk. *Phys. Rev. Lett.* **68**, 847 (1992).
- 2.34. M. T. Anderson, K. B. Greenwood, G. A. Taylor, and K. R. Poeppelmeier. *Prog. Solid State Chem.* **22**, 197 (1993).
- 2.35. T. Sebastian. *Dielectric Materials for Wireless Communication*. Elsevier Science (2008).
- 2.36. W. Dmowski, M. K. Akbas, P.K. Davies, and T. Egami. *J.Phys. and Chem. of Solids* **61**, 229 (2000).
- 2.37. V. Marinova, B. Mihailova, T. Malcherek, C. Paulmann, K. Lengyel, L. Kovacs, M. Veleva, M. Gospodinov, B. Guttler, R. Stosch, and U. Bismayer. *J. Phys.Condens. Matter* **18**, L385 (2006).
- 2.38. T. Yamanaka, N. Hirai, and Y. Komatsu. *Am. Mineral.* **87**, 1183 (2002).
- 2.39. N. D. Zakharov, K. Satyalakshmi, G. Koren, and D. Hesse. *J. Mater. Res.* **14**, 4385 (1999).
- 2.40. J. J. Randall and R. Ward. *J. Am. Chem. Soc.* **81**, 2629 (1959).
- 2.41. C. B. Eom, R. B. Van Dover, J. M. Phillips, D. J. Werder, J. H. Marshall, C. H. Chen, R. J. Cava, R M. Fleming, and D. K. Fork. *Appl. Phys. Lett.* **63**, 2570 (1993).
- 2.42. C. Wang and M. H. Kryder. *Phys. Scr.* **78**, 035601 (2008).
- 2.43. H. R. Von, J. Wecker, B. Holzapfel, L. Schultz and K. Samwer. *Phys. Rev. Lett.* **71**, 2331 (1993).
- 2.44. J.-L. Maurice, F. Pailloux, A. Barthelemy, O. Durand, D. Imhoff, R. Lyonnet, A. Rocher and J.-P Contour. *Phil. Mag.* **83**, 3201 (2003).
- 2.45. D. K. Fork, D. B. Fenner, G. A. N. Connell, J. M. Phillips, and T. H. Geballe. *Appl. Phys. Lett.* **57**, 1137 (1990).
- 2.46. S. J. Wang, C. K. Ong, L. P.You, and S. Y. Xu. *Semicond. Sci. Technol.* **15**, 836 (2000).
- 2.47. A.R. James, A. Pignolet, S. Senz, N.D. Zakharov, and D. Hesse. *Solid State Communications.* **114**, 249 (2000).
- 2.48. W. Matthews and A. E. Blakeslee. *J. Crystal Growth* **27**, 118 (1974).
- 2.49. S. Y. Hu, Y. L. Li, and L. Q. Chen. *J.Appl.Phys.* **94**, 2542 (2003).
- 2.50. R. E. Leuchtner and K. S. Grabowski. Ferroelectrics. In D. B. Chrisey and G. K. Hubler (eds.). *Pulsed Laser Deposition of Thin Films*. John Wiley & Sons, Inc. (1994).
- 2.51. G. Rosenfeld, B. Poelsema, and G. Comsa. *Epitaxial growth modes far from equilibrium*. In D. A. King (ed.) *The chemical physics of solid surfaces*. Elsevier Science B.V. (1997).
- 2.52. K. Sangwal and R. Rodriguez-Clemente. *Surface morphology of crystalline materials*. Trans Tech Publications (1991).

## Chapter 3

- 3.1. L. Corraera, and S. Nicoletti. *Materials Science and Engineering B* **32**, 33 (1995).



- 3.2. S. Fahler, and H. U. Krebs. *Applied Surface Science*, **61**, 96-98 (1996).
- 3.3. K. L. Saenger. Angular distribution of ablated material. In D. B. Chrisey and G. K. Hubler (eds.). *Pulsed Laser Deposition of Thin Films*. JohnWiley & Sons, Inc. (1994).
- 3.4. H. M. Smith and A. F. Turner. *Applied Optics* **4**, 147 (1965).
- 3.5. H. Schwarz, and H. A. Tourtellotte. *J. Vac. Sci Technol.* **6**, 373 (1968).
- 3.6. D. Dijkkamp and T. Venkatesan. *Appl. Phys. Lett.* **51**, 619 (1987).
- 3.7. D. Bauerle, M. Dinescu, R. Dinu, J. Pedarnig, J. Heitz, R. Schwodiauer, S. Bauer, and S. Bauer-Gogonea. Pulsed-laser deposition and characterization of thin films. In C. Galassi, M. Dinescu, K. Uchino, and M. Sayer (eds.). *Piezoelectric materials: Advances in science, technology and applications*. Kluwer Acad. Publ. (2000).
- 3.8. I.W. Boyd. *Laser Processing of Thin Films and Microstructures*, Springer Verlag, Germany (1987).
- 3.9. T. Venkatesan, X. D. Wu, A. Inam, and J. B. Wachtman. *Appl. Phys. Lett.* **52**, 1193 (1988).
- 3.10. R. KellyMennig. *J. Chem. Phys.* **92**, 5047 (1990).
- 3.11. C. R. Phipps *et al.* *J. Appl. Phys.* **64**, 1083 (1988).
- 3.12. N.G. Basov, V.A. Danilychev, Y.M. Popov, D.D. Khodkevich. *Zhourn. Eksperim. Fisika i Tekhnika Pis. Red.* **12**, 473 (1970).
- 3.13. H. von Bergmann, U. Stamm. Principles of Excimer Lasers. In D. Basting and G. Marowsky (eds.). *Excimer Laser Technology*. Springer-Verlag (2005).
- 3.14. A. Ostendorf, U. Stamm, and T. Temme. Proc. 2nd Int. Symp. *Laser Precision Microfabrication (LPM2001)*, (Singapore, 2001).
- 3.15. Z. Zhu, X. J. Zheng, and W. Li. *J. Appl. Phys.* **106**, 054105 (2009).
- 3.16. H. C. Wang and W. A. Schulze. *J. Am. Ceram Soc.* **73**, 1228 (1990).
- 3.17. R. E. Leuchtner and K. S. Grabowski. Ferroelectrics. In D. B. Chrisey and G. K. Hubler (eds.). *Pulsed Laser Deposition of Thin Films*. John Wiley & Sons, Inc. (1994).
- 3.18. P. F. Fewster: *X-ray scattering from semiconductors*. Imperial College Press (2003).
- 3.19. R. A. Young. *The Rietveld Method*. Oxford University Press. Inc. (1993).
- 3.20. <http://journals.iucr.org/j/issues/2001/02/00/hw0089/hw0089bdy.html>.
- 3.21. G. Binnig, C. F. Quate, and Ch. Gerber. *Phys. Rev. Lett.* **56**, 930 (1986).
- 3.22. P. Guthner and K. Dransfeld. *Appl. Phys. Lett.* **61**, 1137 (1992).
- 3.23. M. Alexe, C. Harnagea, D. Hesse, and U. Gösele. *Applied Physics Letters*, **79**, 242 (2001).
- 3.24. A. Gruverman, A. Kholkin, A. Kingon, and H. Tokumoto. *Appl. Phys. Lett.* **78**, 2751 (2001).
- 3.25. B. J. Rodriguez, A. Gruverman, A. I. Kingon, R. J. Nemanich, and J. S. Cross. *J. Appl. Phys.* **95**, 1958 (2004).
- 3.26. G. Suyal, E. Colla, R. Gysel, M. Cantoni, and N. Setter. *Nanolett.* **4**, 1339 (2004).
- 3.27. S. N. Magonov and M.-W. Hwangbo. *Surface Analysis with STM and AFM: Experimental and Theoretical Aspects of Image Analysis* (VCH, Weinheim, 1996).
- 3.28. M. Alexe and A. Gruverman. *Nanoscale Characterisation of Ferroelectric Materials: ScanningProbe Microscopy Approach*. Springer, Berlin (2004).
- 3.29. <http://www.asylumresearch.com/Applications/PFMAppNote/PFMAppNote.shtml>

- 3.30. D. B. Williams and C. B. Carter. *Transmission Electron Microscopy*. Plenum Press, New York and London (1996).
- 3.31. R. F. Egerton. *Physical Principles of Electron Microscopy: An Introduction to TEM, SEM, and AEM*. Springer (2005).
- 3.32. L. Pintilie and M. Alexe. *Appl. Phys. Lett.* **87**, 112903 (2005).

### Chapter 4.1

- 4.1.1. K. Suu, T. Masuda, Y. Nishioka, and N. Tani. ISAF-XI, New York: IEEE, **19** (1998).
- 4.1.2. K. Brinkman, Y. Wang, D. Su A. Tagantsev, P. Muralt, and N. Setter. *J. Appl. Phys.* **102**, 044110 (2007).
- 4.1.3. W. Dmowski, M. K. Akbas, P. K. Davies, T. Egami. *J. Phys. Chem. Solids.* **61**, 229 (2000).
- 4.1.4. M. Lippmaaa, K. Takahashib, A. Ohtomoa, S. Ohashic, T. Ohnishic, N. Nakagawaa, T. Satod, M. Iwatsukid, H. Koinumac, and M. Kawasakia. *Mat. Sci. Eng.* **56**, 111 (1998).
- 4.1.5. E. Patella, A. Sgarlata, F. Arciprete, S. Nufriis, P.D. Szkutnik, E. Placidi, M. Fanfoni, N. Motta and A. Balzarotti. *J. Phys. Condens. Matter.* **16**, S1503 (2004).
- 4.1.6. M. Yoon, H. N. Lee, W. Hong, H. M. Christen, Z. Zhang, and Z. Suo. *Phys. Rev. Lett.* **99**, 055503 (2007).
- 4.1.7. W. Hong, H. N. Lee, M. Yoon, H. M. Christen, D. H. Lowndes, Z. Suo, and Z. Zhang. *Phys. Rev. Lett.* **95**, 095501 (2005).
- 4.1.8. J. W. Matthews, *Epitaxial Growth, Part B*, Ed. J. W. Matthews, p. 559 (Academic, New York, 1975).
- 4.1.9. B. I. Birajdar, A. Chopra, M. Alexe, and D. Hesse. *Acta Materialia. No. A-11-331R1* (2011).
- 4.1.10. S. Murakami, D. Popovici, K. Satoh, M. Matsumoto, M. Noda, and M. Okuyama, *Sens. Mater.* **16**, 231 (2004).
- 4.1.11. L. E. Cross, *Ferroelectrics.* **76**, 241 (1987).
- 4.1.12. G. Burns and F. H. Dacol. *Sol. Stat. Commun.* **48**, 853 (1983).
- 4.1.13. S. B. Vakhrushev, B. E. Kvyatkovsky, A. A. Nabereznov, N. M. Okuneva and B. P. Toperverg. *Ferroelectrics.* **90**, 173 (1989).
- 4.1.14. A. Nabereznov, S. Vakhrushev, B. Dorner, D. Strauch and H. Moudden. *Eur. Phys. J.* **11**, 13 (1999).
- 4.1.15. K. Hirota, Z. G. Ye, S. Wakimoto, P. M. Gehring and G. Shirane. *Phys. Rev. B.* **65**, 104105 (2002).
- 4.1.16. S. Vakhrushev, A. Nabereznov, S. K. Sinha, Y. P. Feng and T. Egami. *J. Phys. Chem. Solids.* **57**, 1517 (1996).
- 4.1.17. K. Brinkman, Y. Wang, D. Su, A. Tagantsev, P. Muralt, and N. Setter. *J. Appl. Phys.* **102**, 044110 (2007).
- 4.1.18. Pintilie, I. Vrejoiu, D. Hesse, G. LeRhun, and M. Alexe. *Phys. Rev. B.* **75**, 224113 (2007).
- 4.1.19. D. Rubi, A.H.G. Vlooswijk, B. Noheda. *Thin Solid Films.* **517**, 1904 (2009).

### Chapter 4.2

- 4.2.1. J. W. Matthews, *Epitaxial Growth, Part B*, Ed. J. W. Matthews, p. 559 (Academic, New York, 1975).
- 4.2.2. J. E. Ayers: *Heteroepitaxy of semiconductors: Theory, growth, and characterization*. CRC Press (2007).
- 4.2.3. W. Dmowski, M. A. Akbas, P. K. Davies, and T. Egami. *J. Phys. Chem. Solids* **61**, 229 (2000).
- 4.2.4. S. Choudhury, Y. L. Li, L. Q. Chen, and Q. X. Jia. *Appl. Phys. Lett.* **92**, 142907 (2008).
- 4.2.5. H. Ma, L. Chen, J. Wang, J. Ma, and F. Boey. *Appl. Phys. Lett.* **92**, 182902 (2008).
- 4.2.6. A.F. Devonshire. *Theory of barium titanate - part II*, *Philos. Mag.* **42**, 1065 (1951).
- 4.2.7. A. K. Tangsev and A. E. Glazounov. *Phys. Rev. B.* **57**, 18 (1998).
- 4.2.8. D. Kobor, A. Hajjaji, J. E. Garcia, R. Perez, A. Albareda, L. Lebrun, D. Guyomar. *J. Mod. Phys.* **1**, 211 (2010).
- 4.2.9. D. A. Hall and P. J. Stevenson. *Ferroelectrics* **228**, 139 (1999).
- 4.2.10. D. A. Hall. *Ferroelectrics* **223**, 319 (1999).
- 4.2.11. X. W. Zhang, X. Liu, Z. R. Liu and B. L. Gu. *J. Phys.: Condens. Matter.* **12**, 5929 (2000).
- 4.2.12. N. B. Gharba, S. T. McKinsty and D. Damjanovic. *J. Appl. Phys.* **100**, 044107 (2007).
- 4.2.13. T. Tsurumi, K. Soejima, T. Kamiya and M. Daimon. *Jpn. J. Appl. Phys.* **33**, 1959 (1994).
- 4.2.14. M. E. Lines and A. M. Glass: *Principles and Applications of Ferroelectric and Related Materials*. Clarendon Press Oxford (2004).

### Chapter 4.3

- 4.3.1. H. N. Lee, D. Zakharov, S. Senz, A. Pignolet, and D. Hesse. *Integrated Ferroelectrics.* **39**, 73 (2001).
- 4.3.2. X. W. Zhang, X. Liu, Z. R. Liu and B. L. Gu. *J. Phys.: Condens. Matter.* **12**, 5929 (2000).
- 4.3.3. T. Tsurumi, K. Soejima, T. Kamiya and M. Daimon. *Jpn. J. Appl. Phys.* **33**, 1959 (1994).
- 4.3.4. D.A. Draeger and S. Sing. *Solid State Comm.* **9**, 595 (1971).

## **Eidesstattliche Erklärungen**

Hiermit erkläre ich, dass ich die vorliegende Arbeit selbstständig und ohne fremde Hilfe verfasst, andere als die von mir angegebenen Quellen und Hilfsmittel nicht benutzt und die den benutzten Werken wörtlich oder inhaltlich entnommenen Stellen als solche kenntlich gemacht habe.

Anuj Chopra

Halle (Saale), den 17.03.2011

Hiermit erkläre ich, noch keine vergeblichen Promotionsversuche unternommen zu haben.

Anuj Chopra

Halle (Saale), den 17.03.2011

## **Acknowledgements**

This thesis has been performed at Max Planck Institute of Microstructure Physics, Halle. At this point I would like to thank all those who contributed towards the success of this work. First and foremost, I would like to thank the late Prof. Dr. Ulrich Gösele for having faith in me for this Ph.D. position.

I would like to take this opportunity to express my deep sense of gratitude to my supervisor Prof. Dr. Dietrich Hesse for his expert guidance and continuous encouragement throughout the course of this work. It was a rare honor and educative experience working with him. His stimulating scientific discussions at every stage of my research, constant motivation and invaluable inputs considerably contributed to the completion of this work. His eternal care and protectiveness towards his students has set an exemplary example to being a mentor that I one day dream to become. I also admire his utmost dedication in the time he spent in correcting my amateur language in this thesis particularly in the time of his illness.

I am immensely thankful to my daily supervisor Dr. Marin Alexe for being such a wonderful and friendly person. I am forever indebted for his contribution in influencing my career and personality. The innumerable discussions (about science and life!) during the progress of my work are gratefully acknowledged. I am sincerely thankful to his intellectual support and creative criticism which led me to generate my own ideas and made my work interesting and enjoyable. I remember whenever I started my day with his pleasant smile 😊 I got good results. Besides ferroelectrics, I learnt many good qualities (especially patience and positive attitude) from him. As a matter of fact, I used to call him as “Gurudev”. During my delays, he used to tell me about German strict time tables. I learnt from him that when you are in Rome, be a Roman but in Germany be ahead in time. I got my lesson and will try to follow the time wherever I stay. 😊

I also thank Dr. Stephan Senz for his fruitful discussions about XRD measurements and Dr. Yunseok Kim for his assistance with PFM measurements.

## *Acknowledgements*

---

I am deeply thankful to Dr. Balaji. I. Birajdar and Dr. Andreas Berger for their valuable efforts and assistance in TEM measurements. My special thanks to Daniel Pantel for helping me in electrical measurements.

I thank to Frau Ina Goffin for reading and correcting the thesis and Frau Julia Duche for taking the pain to write the German version of the summary at a very short notice.

I express my special thanks to Frau Sina Swatek, Frau Mareike Herrman, Frau Silvana Götze for TEM sample preparation, and Herrn Norbert. Schammelt for PLD system maintenance.

I am thankful to DFG via SFB 762 for providing financial support for my doctoral work.

I wish to express my thanks to my colleagues and friends of the Max Planck Institute for their support during my research and also making my stay at Halle pleasant and enjoyable.

I thank Mr. Parveen Kumar (Lala) for being such a lovely friend and for his moral support.

I have no words to express my thanks to my parents and girlfriend Divya who have been constant source of inspiration to me throughout my research. In fact it is due to their encouragement and moral support when personal situations in life had made me crippled, that I am able to submit this thesis today.

## **Curriculum Vitae**

### **Personal information**

First Name:	Anuj
Last Name:	Chopra
Date of birth:	8 March 1981
Place of birth:	Hamirpur, Himachal Pradesh, India
Nationality:	Indian
Sex:	Male
Marital status:	Single

### **Education and Professional experience**

1998-2001	Bachelor of Science, NSCBM Degree College Hamirpur, Shimla University, Summer Hill, India.
2001-2003	Master of Science in Physics (Electronics), Dayalbagh University, Agra, India.
2005-2007	Project-Associate in IITM

### **Achievements and Awards**

Award	Qualified Graduate Aptitude Test in Engineering for Physics conducted by IITs.
	2006 DAAD (German Academic Exchange Service) award for strong academic grades and good scientific achievements.

Anuj Chopra

Halle (Saale), 17 March 2011.

## List Of publications and conference contributions

- ❖ S. Engel, R. Hühne, K. Knoth, A. Chopra, N.H. Kumar, V.S. Sarma, P.N. Santhosh, L. Schultz, B. Holzapfel “Optimisation of single  $\text{La}_2\text{Zr}_2\text{O}_7$  buffer layers for YBCO coated conductors prepared by chemical solution deposition” *J. Crystal Growth* **310**, 4295-4300 (2008).
- ❖ Anuj Chopra, Balaji I. Birajdar, Yunseok Kim, Ionela Vrejoiu, Marin Alexe, and Dietrich Hesse “Epitaxial, cation-ordered, ferroelectric  $\text{PbSc}_{0.5}\text{Ta}_{0.5}\text{O}_3$  thin films prepared by pulsed laser deposition” *Appl. Phys. Lett.* **95**, 022907 (2009).
- ❖ B. I. Birajdar, A. Chopra, M. Alexe, and D. Hesse “Crystal defects and cation ordering domains in epitaxial  $\text{PbSc}_{0.5}\text{Ta}_{0.5}\text{O}_3$  relaxor ferroelectric thin films investigated by high resolution transmission electron microscopy” *Acta Materialia (accepted)* (2011).
- ❖ Anuj Chopra, Marin Alexe, Balaji I. Birajdar, Yunseok Kim, and Dietrich Hesse “Characterization of  $\text{PbSc}_{0.5}\text{Ta}_{0.5}\text{O}_3$  epitaxial thin films prepared by pulsed laser deposition” 73rd Annual Meeting of the DPG 2007, Dresden (Talk).
- ❖ Anuj Chopra, Yunseok Kim, Marin Alexe and Dietrich Hesse “Epitaxial thin  $\text{PbSc}_{0.5}\text{Ta}_{0.5}\text{O}_3$  films on Si (100) by PLD” International Workshop on Functionality of Oxide Interfaces and Multiferroic Materials, Monastery Irsee, 2010 (Poster).



- ❖ B. I. Birajdar, A. Chopra, I. Vrejoiu, M. Alexe and D. Hesse “TEM study of ordering domains in  $\text{PbSc}_{0.5}\text{Ta}_{0.5}\text{O}_3$  and threading dislocations in  $\text{Ba}_{0.7}\text{Sr}_{0.3}\text{TiO}_3$  epitaxial films” Microscopy Conference ,Graz , 2009 (Poster).
- ❖ Participated in IMPRS workshop on “Advances in Science and Technology of Nanostructures” Halle (Salle), 2008.